2021

Rational Design of Advanced Functional Materials for Electrochemical Devices

Shun Lu
South Dakota State University

RATIONAL DESIGN OF ADVANCED FUNCTIONAL MATERIALS FOR ELECTROCHEMICAL DEVICES

BY

SHUN LU

A dissertation submitted in partial fulfillment of the requirements for the

Doctor of Philosophy

Major in Agricultural, Biosystems and Mechanical Engineering

South Dakota State University

2021

DISSERTATION ACCEPTANCE PAGE

Shun Lu

This dissertation is approved as a creditable and independent investigation by a candidate for the Doctor of Philosophy degree and is acceptable for meeting the dissertation requirements for this degree. Acceptance of this does not imply that the conclusions reached by the candidate are necessarily the conclusions of the major department.

Zhengrong Gu
Advisor Date

Van Kelley
Department Head Date

Nicole Lounsbery, PhD
Director, Graduate School Date

This dissertation is dedicated to my parents and Miss. Yuehui Wang for their loving support and encouragement.

ACKNOWLEDGEMENTS

It is the end of my PhD journey involving memorable times and many experiences in science and social life in Brookings, South Dakota. I would like to thank all the people who contribute this journey with their encouragements and supports. I apologize on beforehand that I probably miss some people in the follow acknowledgements.

First, I would like to convey my deepest appreciation to my advisor, Professor Zhengrong (Jimmy) Gu, for his paternally guidance, support, and encouragement, and his infectious enthusiasm and creativity during the past two and half years. I am indebted to Jimmy who consistently raised his level of expectations of my accomplishments and successfully showed me that I am capable of much more than I originally set out to be. My sincere appreciation and thanks to Prof. Anderson Gary, Prof. Natalie Thiex, and Prof. Yue Zhou for their guidance and support as great teachers and committee members.

I was also lucky to be able to associate myself with the talented and hardworking members of past, present, and future Gu group member. Dr. Keliang Wang, Dr. Matthew Hummel, Matthew Cole and Dr. Hongxing Jia, whose insightful ideas and technical skills always motivate me, provided many assistance during my early research stage in the group. I would like thank Dr. Yucheng Wang for being such a brotherly friend during I visited in Northumbria University. I also cherish the friendship with Prof. Xiaoteng Liu and appreciate the opportunity to interact with him in his group. I really enjoyed working with Dr. Xueqiang Qi, Dr. Xianhui Zhao and like to thank them for many interesting and good-spirited discussions relating to this research and for their friendship.

I am grateful to Prof. Yue Zhou and his lab members, including Dr. Ke Chen, Dr. Rajesh Pathak, and Wei He, for their technical assistance, patience, and kindness. Without their generous help and assistance, I could not have made it possible within three years.

I also like to express my gratitude to my friends outside of the lab who made my graduate school experience memorable. I thank Prof. Kelly, Cindy, Jasmine, Brenda, and Jeff for their sincere helps, and Yu Shen, Yong-chang Ye, Yiran Zhang, Xiao-man Lu, Lun Gao, Zhisheng (Jason) Cen, Mengling Ding, Ailin Guo for their friendship and encouragement.

I need also express my feeling of gratitude to Renewable Fuels Foundation and Bob Sather Memorial Scholarship committee for selecting me as the scholarship recipient, which really provided me the financial and spiritual supports. This will motivate me to achieve the excellence in my research area during my tenure at SDSU and beyond.

I reserve my deepest gratitude for Yuihui, my dad Deming Lu, and my mom Huimin Ren. To Yuehui, I want to thank your constant love, support, patience, and encouragement for the past years, for putting up with me even while dealing the stresses of your job despite the long distance. Finally, I am forever grateful to my parents, who throughout my life have provided me with the love, support, and family stability necessary to pursue my goals. I would not have been able to accomplish what I have today if it were not for your unconditional support.

1st July, 2021

CONTENTS

ABBREVIATIONS[1]

AC alternating current

AE auxiliary electrode

AFC alkaline fuel cell

AFM Atomic force microscopy

BET Brunauer-Emmett-Teller theory

CD current density

Cdl Capacitance of the electrochemical double layer

CE Counter electrode

CV Cyclic voltammetry

DC direct current

DFT Density functional theory

DME dropping mercury electrode

DMF dimethylformamide

DMFC direct methanol fuel cell

DPV Differential pulse voltammetry

ECC electrocapillary curves

---

[1] These abbreviations are used in most chapters. In some chapters other (specific) abbreviations are used. Abbreviations employed in theoretical experimental methods used in electrochemistry are listed in Chapter 3.

ECSA Electrochemical active surface area

EDL electric double layer

EDX Energy Dispersive X-Ray Analysis

EIS Electrochemical impedance spectroscopy

EMF electromotive force

EPS electrochemical power source

ESE excess surface energy

ESM Eggshell membrane

ETR electron transfer reaction

eV electron-volt

Glu Glucose

hap high anodic potentials

HER Hydrogen evolution reaction

ITIES interface between two immiscible electrolyte solutions

LPD linear potential scan

LSV Linear sweep voltammetry

MCFC molten carbonate fuel cell

MEA membrane-electrode assembly

MIEC	mixed ionic-electronic conductor
mM	Kilogram per mole
NiPc	Nickel(II) phthalocyanine
OCP	open-circuit potential
OCV	open-circuit voltage
ORR	Oxygen reduction reaction
Ox	oxidized form
PAFC	phosphoric acid fuel cell
PC	propylene carbonate
PD	potential difference
PTFE	polytetrafluoroethylene
PVC	poly(vinyl chloride)
PZC	point (or potential) of zero charge
RDE	rotating disk electrode
RDS	Rate-determining step
RE	Reference electrode
Red	Reduced form
SEM	Scanning electron microscopy

SHE	Standard hydrogen electrode
STEM	Scanning transmission electron microscope
SWV	Sweep wave voltammetry
TEM	Transmission electron microscope
TGA	Thermal gravimetric analysis
UOR	Urea oxidation reaction
WE	Working electrode
XPS	X-ray photoelectron spectroscopy
XRD	X-ray diffraction
ZIF	Zeolitic imidazolate framework

LIST OF FIGURES

LIST OF TABLES

ABSTRACT

RATIONAL DESIGN OF ADVANCED FUNCTIONAL MATERIALS FOR ELECTROCHEMICAL DEVICES

SHUN LU

2021

In recent years, there has been a fast-growing trend in developing urea ($CO(NH_2)_2$) as a substitute H_2 carrier in energy conversion due to its high energy density, nontoxicity, stability, and nonflammability. Urea, a byproduct in the metabolism of proteins and a frequent contaminant in wastewater, is an abundant compound that has demonstrated favorable characteristics as a hydrogen-rich fuel source with 6.7 wt % gravimetric hydrogen content. Also, there is 2-2.5 wt % urea from mammal urine; therefore, 0.5 million ton of additional fuels will be produced per year just from human urine (240 million ton each year). Electrochemical oxidation has been recognized as an efficient strategy for urea conversion and wastewater remediation. Thus, the chemical energy harvested from urea/urine can be converted to electricity via urea oxidation reaction (UOR). Moreover, the removal of urea from water is a priority for improving drinking water quality and presents an opportunity for UOR. However, the transition of UOR from theory and laboratory experiments to real-world applications is largely limited by the conversion efficiency, catalyst cost, and feasibility of wide-spread usage. Therefore, utilization of urea using electrochemical method is a 'two birds with one stone' strategy which convert wastewater to electricity via anodic urea oxidation reaction (***Seen in Chapter 2***).

Developing efficient and low-cost urea oxidation reaction (UOR) catalysts is a promising but still challenging task for environment and energy conversion technologies such as wastewater remediation and urea electrolysis. NiO nanoparticles that incorporated graphene as the NiO@Graphene composite were constructed to study the UOR process in terms of density functional theory. The single-atom model, which differed from the previous used heterojunction model (***Chapter 2***), was employed for the adsorption/desorption of urea and CO_2 in the alkaline media. As demonstrated from the calculated results, NiO@Graphene prefers to adsorb the hydroxyl group than urea in the initial stage due to the stronger adsorption energy of the hydroxyl group. After NiOOH@Graphene was formed in the alkaline electrolyte, it presents excellent desorption energy of CO_2 in the rate-determining step. Electronic density difference and the d band center diagram further confirmed that the Ni(III) species is the most favorable site for urea oxidation while facilitating charge transfer between urea and NiO@Graphene. Moreover, graphene provides a large surface for the incorporation of NiO nanoparticles, enhancing the electron transfer between NiOOH and graphene and promoting the mass transport in the alkaline electrolyte. Notably, this work provides theoretical guidance for the electrochemical urea oxidation work (***As presented in Chapter 3***).

In addition, urea oxidation reaction (UOR) has been known as a typical energy conversion reaction but is also a viable method for renal/liver disease diagnostic detection. Here, we reported the three-dimensional nickel oxide nanoparticles decorated on the carbonized eggshell membrane (3D NiO/c-ESM) as a modified electrode toward urea detection. The electrocatalysts are characterized by XRD, SEM, and EDX to confirm its structural and morphological information. NiO/c-ESM modified electrode exhibits an outstanding performance for urea determination with a

linear range from 0.05 to 2.5 mM, and limit detection of ~20 μM (3σ). This work offered a green approach for introducing 3D nanostructure through employing biowaste ESMs as templates, providing a typical example for producing new value-added nanomaterials with urea detection (***Presented in Chapter 4***).

Generally, urea oxidation reaction happens on the anode, less attention is paid on the cathode. In fact, hydrogen evolution reaction happens on cathode during water/urea electrolysis. Therefore, in this chapter (***Chapter 5***), we focus our attention on the cathodic reaction, as follows: Transition metal oxides (TMOs), especially nickel oxide (NiO), are environmentally benign and cost-effective materials, and have recently emerged as potential hydrogen evolution reaction (HER) electrocatalysts for future industrial scale water splitting in alkaline environment. However, their applications in HER electrocatalysts remain challenging because of poor electronic conductivity and unsatisfactory activity. Besides, the disposal of eggshell waste is also an environmentally and economically challenging problem because of food industry. Here, we report the synthesis of NiO nanoparticles (NPs) encapsulated in the carbonization of eggshell membrane via a green and facile approach for HER application. Noteworthy to mention here that the active carbon was made from the waste, eggshell membrane (ESM), meanwhile, the eggshell was used as a micro-reactor for preparation of electrocatalyst, NiO/C nanocomposite. Then, the as-prepared NiO/C nanocomposite was characterized by scanning electron microscopy (SEM), transmission electron microscopy (TEM), X-ray diffraction (XRD) and energy dispersive x-ray spectroscopy (EDS). The SEM, EDS and TEM images reveal that NiO nanoparticles distributed on the carbon support, and XRD patterns confirm the presence of the nanoparticles are NiO and C hybrids. The catalytic activity and durability of NiO/C nanocomposite was examined for HER in 1 M KOH solution. It has been

observed that NiO/C nanocomposite showed the better catalytic activity with the smallest Tafel slope of 77.8 mV dec^{-1} than single component's result, NiO particles (112.6 mV dec^{-1}) and carbonization of ESM (94.4 mV dec^{-1}). It indicates that the HER performance of electrocatalyst can be enhanced by synergistic effect between NiO particles and carbonization of ESM, with better durability after 500 CV cycles. Furthermore, such design principle for developing interfaces between TMOs and C by a green and facile method can offer a new approach for preparing more efficient electrocatalysts (***Seen in Chapter 5***).

Differed from other chapters, Chapter 4 focuses on the electroanalytical application of advanced nanomaterials. In this chapter, the sweep wave voltammetry (SWV) method was used for molecule detection. It is noted that we also developed several methods to detect small molecules, including differential pulse voltammetry (DPV) and chronopotentiometry (*i*-*t*). Therefore, several novel nanomaterials like gold nanoparticles and ZIF-8, two-dimensional nickel phthalocyanine-based metal-organic framework compounds were synthesized, respectively, and then used for the electroanalytical application, listed as ***Appendix A*** and ***B*** avoiding breaking the logistic of the whole manuscript.

CHAPTER 1 INTRODUCTION AND BACKGROUND

1.1 Electrocatalysis and electroanalysis

Electrochemistry is the branch of physical chemistry concerned with the relationship between electrical potential, as a measurable and quantitative phenomenon, and identifiable chemical change, with either electrical potential as an outcome of a particular chemical change, or vice versa. These reactions involve electrons transferring between electrodes via an electricity-conducting phase, separated by an ion-conducting and electronically insulating electrolyte. When a chemical reaction is affected by a potential difference, for example in electrolysis, or if electrical potential results from a chemical reaction as in a battery or fuel cell, it is called an electrochemical reaction. Unlike chemical reactions, in electrochemical reactions electrons, are not transferred directly between molecules, but via the aforementioned electronically- and ionically-conducting circuits, respectively. This phenomenon is what distinguishes an electrochemical reaction from a chemical reaction. Electrochemistry also provides several promising approaches for the energy conversion and storage (Fig. 1.1).

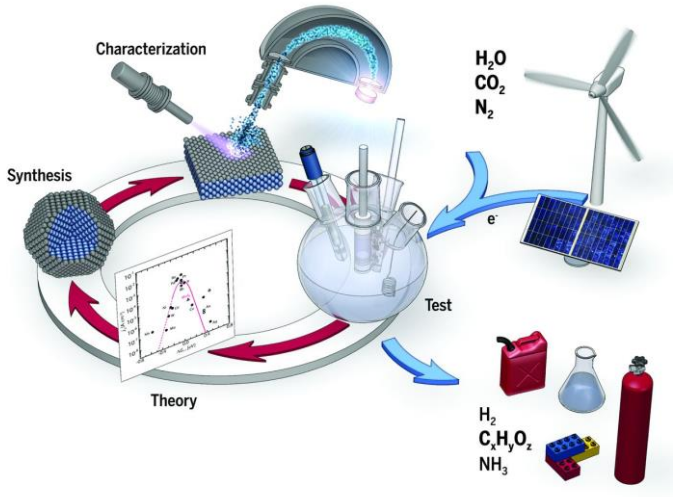

Figure 1.1 the relationship between electrochemistry and huamn activity

1.1.1 Hydrogen production via electrochemical approach

Electrolysis is a promising option for carbon-free hydrogen production from renewable and nuclear resources. Electrolysis is the process of using electricity to split water into hydrogen and oxygen. This reaction takes place in a unit called an electrolyzer (Fig. 1.2). Electrolyzers can range in size from small, appliance-size equipment that is well-suited for small-scale distributed hydrogen production to large-scale, central production facilities that could be tied directly to renewable or other non-greenhouse-gas-emitting forms of electricity production. Like fuel cells, electrolyzers consist of an anode and a cathode separated by an electrolyte. Different electrolyzers function in different ways, mainly due to the different types of electrolyte material involved and the ionic species it conducts. Alkaline electrolyzers operate via transport of hydroxide ions (OH-) through the electrolyte from the cathode to the anode with hydrogen being generated on the cathode side. Electrolyzers using a liquid alkaline solution of sodium or potassium hydroxide as the electrolyte have been commercially available for many years. Newer approaches using solid alkaline exchange membranes (AEM) as the electrolyte are showing promise at the lab scale.

In a proton exchange membrane (PEM) electrolyzer, the electrolyte is a solid specialty plastic material (Fig. 1.3)

- Water reacts at the anode to form oxygen and positively charged hydrogen ions (protons).
- The electrons flow through an external circuit and the hydrogen ions selectively move across the PEM to the cathode.

- At the cathode, hydrogen ions combine with electrons from the external circuit to form hydrogen gas. Anode Reaction: $2H_2O \rightarrow O_2 + 4H^+ + 4e^-$ Cathode Reaction: $4H^+ + 4e^- \rightarrow 2H_2$

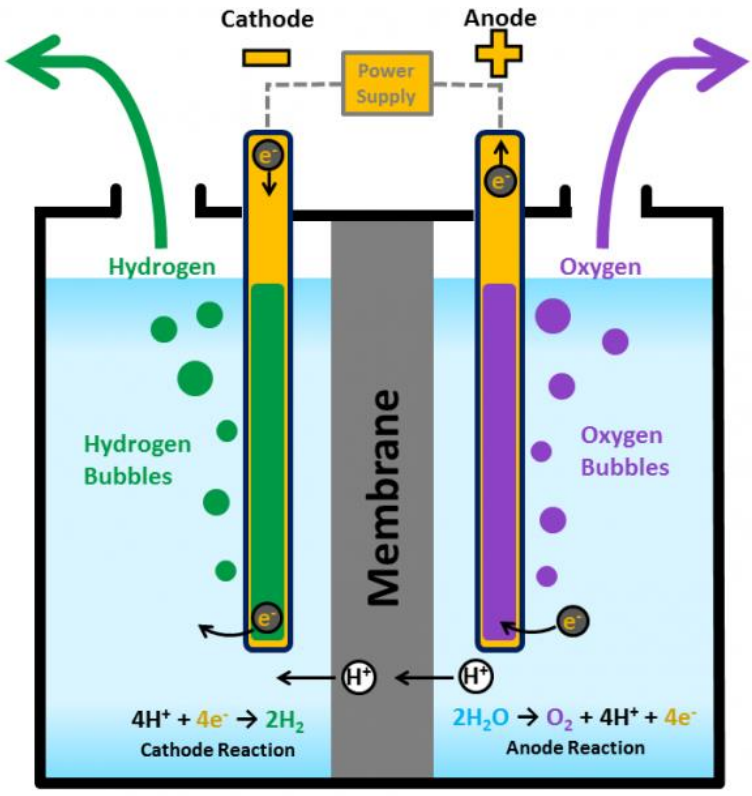

Figure 1.2 Scheme of water electrolysis via proton exchange membrane electrochemical cell [1]

Hydrogen production via electrolysis may offer opportunities for synergy with dynamic and intermittent power generation, which is characteristic of some renewable energy technologies. For example, though the cost of wind power has continued to drop, the inherent variability of wind is an impediment to the effective use of wind power. Hydrogen fuel and electric power generation could be integrated at a wind farm, allowing flexibility to shift production to best match resource availability with system operational needs and market factors. Also, in times of excess electricity production

from wind farms, instead of curtailing the electricity production as is commonly done, it is possible to use this excess electricity to produce hydrogen through electrolysis.

It is important to note that,

- Today's grid electricity is not the ideal source of electricity for electrolysis because most of the electricity is generated using technologies that result in greenhouse gas emissions and are energy intensive. Electricity generation using renewable or nuclear energy technologies, either separate from the grid, or as a growing portion of the grid mix, is a possible option to overcome these limitations for hydrogen production via electrolysis.

- The U.S. Department of Energy and others continue efforts to bring down the cost of renewable-based electricity production and develop more efficient fossil-fuel-based electricity production with carbon capture, utilization, and storage. Wind-based electricity production, for example, is growing rapidly in the United States and globally.

Research Focuses on Overcoming Challenges

- Meeting the Hydrogen Shot clean hydrogen cost target of \$1/kg H_2 by 2030 (and interim target of \$2/kg H_2 by 2025) through improved understanding of performance, cost, and durability trade-offs of electrolyzer systems under predicted future dynamic operating modes using CO_2 -free electricity.
- Reducing the capital cost of the electrolyzer unit and the balance of the system.
- Improving energy efficiency for converting electricity to hydrogen over a wide range of operating conditions.

1.1.2 Energy conversion via urea oxidation reaction

The increasing demand of energy has induced high consumption of fossil fuels and a drastic increase in environmental problems, which draws a great attention.[2, 3] Instead of fossil fuels, hydrogen fuel is believed to be a clean energy with the only combust product being water.[4] For conventional hydrogen production, water electrolysis requires relatively high applied potential of 1.23 V[5], due to the sluggish kinetics of the oxygen evolution reaction (OER) at the anode half-cell, resulting in a comparatively high overpotential.[6-8] Recently, the electrochemical urea oxidation reaction (UOR) to produce hydrogen has been attracting a lot of interest (Fig. 1.3). Urea is earth abundant from urea-rich wastewater in nature which comes from human or animal urine, where it is harmful to environment and public health[9]. Numerous technologies have been used for urea-containing wastewater treatment, such as chemical oxidation, hydrolysis, and biological decomposition. These methods are not economic and environmental friendly.[10] Therefore, utilization of urea using the electrochemical method is a 'two birds with one stone' strategy which converts wastewater to renewable hydrogen.

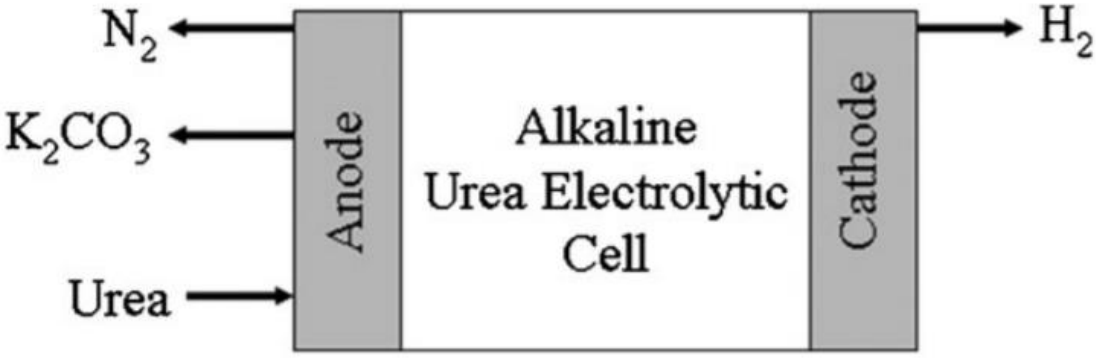

Figure 1.3 Schematic representation of the direct urea-to-hydrogen process

The urea oxidation reaction is a complicated reaction process with six electrons transfered, the primary step of UOR is the urea-oxidation reaction at the anodic side[11, 12]:

Anode:

$$CO(NH_2)_2(aq) + 6OH^- - 6e^- \rightarrow N_2(g) + 5H_2O(l) + CO_2(g)$$

Where the cathode site is the production of hydrogen:

$$6H_2O(l) + 6e^- \rightarrow 3H_2(g) + 6OH^-(aq)$$

And the overall reaction is:

$$CO(NH_2)_2(aq) + 6H_2O(l) \rightarrow N_2(g) + 3H_2(g) + CO_2(g)$$

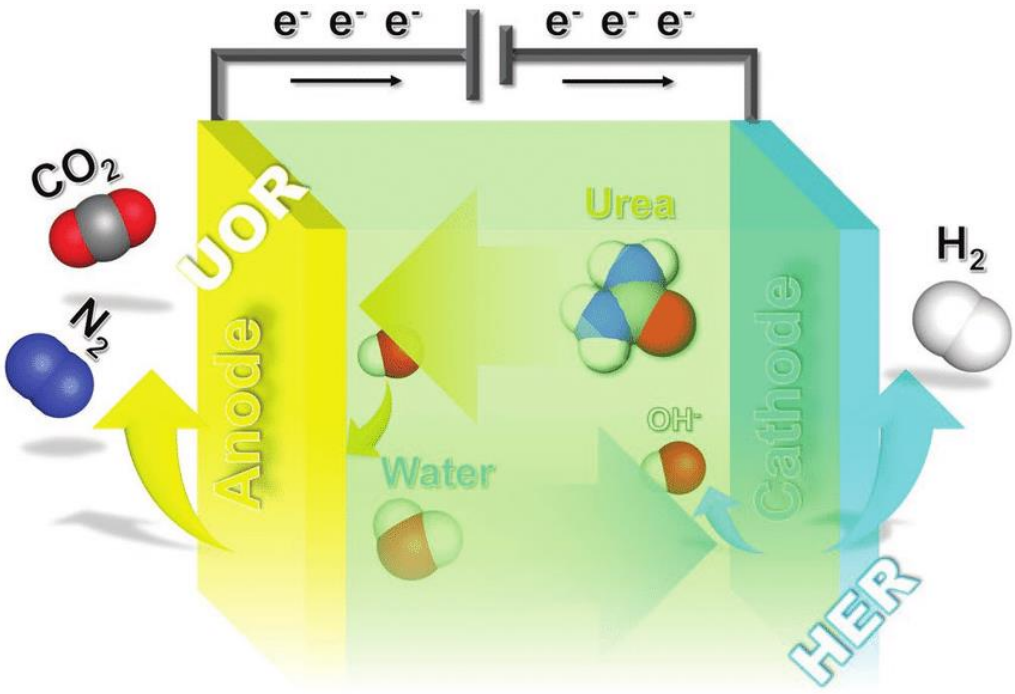

Figure 1.4 An illustration of a typical urea electrolytic cell and it counterpart reaction

Comparing with water electrolysis, UOR requires a lower applied potential of only 0.37 V, therefore less energy input is required at standard conditions[11, 13], which is remarkably lower than water electrolysis with a potential of 1.23 V (Fig. 1.4). Therefore, urea electrolysis is considered as a promising method of hydrogen evolution. However, a key issue of UOR is the low kinetics and low durability of the required catalyst for the reactions. Some noble metal catalyst have been reported such as Pt, Rh, Ir, where the high cost of noble metals becomes one of the hurdles preventing its commercialization. Compared with noble metals illustrated above, nickel-based catalysts and their derivatives have been discovered to have good UOR performance, with their good catalytic activity, earth abundance at low-cost, and robust urea electro oxidation[14-16].

1.1.3 Theoretical insights on urea oxidation reaction

The mechanism of urea decomposition in the aqueous phase has been further studied by different authors. In an aqueous solution, the elimination mechanism yields isocyanic acid and ammonia, whereas intramolecular proton transfer with urease gives cyanic acid and ammonia. In addition, their analyses of the activation energies of aqueous elimination and hydrolytic mechanism pathways of urea concluded that urea prefers to eliminate ammonia rather than undergo hydrolysis.

Although significant contributions have been made in the study of the hydrolysis mechanism of urea in the presence of urease both experimentally and theoretically, studies on electrooxidation of urea in an alkaline medium using a nickel catalyst (similar to the urease active sites) have not been previously reported in the literature.

Bezerra et al. examined the electrochemical oxidation of urea with platinum as a catalyst in acidic, alkaline, and neutral media. It was found that acidic media produced N_2 and CO_2 with minute amounts of CO generated due to hydrolysis. However, the results in the alkaline media were not clearly elucidated as the focus was placed on the orientation of the urea molecule and the CO formed in the initial hydrolysis. It was found that the urea molecule was adsorbed through the O atom at potentials above −0.4 V and was adsorbed through the amine group below −0.4 V vs an Ag/AgCl reference. Recently, Botte et al. reported the production of ammonia and nitrogen in the anodic compartment of an electrochemical cell during electrolysis of urea and urine for the production of hydrogen. The author suggested that the production of ammonia is due to the chemical oxidation of urea in alkaline media in the presence of the catalyst, while the production of nitrogen is due to the electrooxidation of urea.

1.1.4 Electroanalysis via urea oxidation reaction

Urea, a metabolic end product in the human body, is critical in assessing various metabolic disorders, including renal function. Moreover, monitoring of urea levels is important in the food and environment industries. Chromatographic and spectroscopic methods have been widely employed to measure urea concentrations in biological and chemical samples. However, these methods require tedious sample preparation and cannot be used on-site. Alternative methods using various biosensors based on the urease enzyme have been developed, with simple designs capable of rapid on-site urea analysis. The enzymatic hydrolysis of urea generates ammonia ions and bicarbonate ions, which can be amperometrically, potentiometrically, optically, thermally, and piezoelectrically detected using various transducers.

Amperometric biosensing is considered the most promising approach, because it offers a fast, reliable, simple, and low-cost detection. In urease-based amperometric biosensors, the NH4+ ion can be catalytically oxidized by either a second enzyme or metal catalysts. However, denaturing of the enzyme can cause poor long-term stability. Recently, non-enzymatic biosensors with metal-based catalysts have received widespread interest because of the high sensitivity and stability of the devices. Metal oxides such as NiO, CuO, and ZnO, with low costs and well-defined redox properties, have been employed for direct electro-catalytic oxidation and determination of many biochemical compounds such as urea, glucose, and ethanol. In particular, Ni-based catalysts have exhibited excellent catalytic abilities for urea oxidation.

1.2 Motivation and objectives

1.2.1 Motivation

Inspired from the porous carbon, especially biomass-derived carbon, which can provide a stable, porous, and robust support for advanced materials, the novel porous structure can be suitable for electrocatalysis and electroanalysis. The disposed eggshell can be seen anywhere from the food industry and daily life. Therefore, based on what we demonstrated before, we tried to construct several novel nanostructured materials for efficient electrochemical reactions. Similarly, consider the concept of ‘trash to treasure’, urea, mainly produced from human or mammal animal urine and widely exists in sewage, can be utilized as a new fuel due to its high content of hydrogen. It means urea can be processed via an electrochemical approach, reducing potential environmental problem, whilst converting the waste into energy.

1.2.2 **Objectives**

The objective of this dissertation is to develop a multi-functional material based on biomass-derived carbon, working as the electrocatalyst for multi-functional applications, including energy conversion and storage and electrochemical detection. As a supplement, other materials, i.e., metal-organic framework compounds, were also explored as electrocatalyst for small molecule detection using different detection methods.

- Evaluate the porous properties of the carbon materials which were produced from the eggshell membrane by SEM, TEM and BET characterizations.
- Analyze the performance of the eggshell membrane-derived carbon towards urea oxidation through a series of electrochemical approaches and physical measurements.
- Analyze the potential mechanism of urea oxidation reaction on the synthesized sample with theoretical method (density functional theory).
- Evaluate the performance of the eggshell membrane-derived carbon towards urea detection via sweep wave voltammetry.
- Evaluate the performance of hydrogen production on the eggshell membrane-derived carbon properties by cyclic voltammetry, linear sweep voltammetry and electrochemical impedance spectroscopy.

CHAPTER 2 HIGHLY EFFICIENT UREA OXIDATION VIA NESTING NANO-NICKEL OXIDE IN EGGSHELL MEMBRANE-DERIVED CARBON[2]

2.1 Introduction

In recent years, there has been a fast-growing trend in developing urea ($CO(NH_2)_2$) as a substitute H_2 carrier in energy conversion due to its high energy density, nontoxicity, stability and non-flammability.[17] Urea, a byproduct in the metabolism of proteins and a frequent contaminant in wastewater, is an abundant compound that has demonstrated favorable characteristics as a hydrogen-rich fuel source with 6.7 *wt.*% in gravimetric hydrogen content.[17-20] Also, human urine is 2-2.5 *wt.*% urea, therefore, 0.5 million tons of additional fuel will be produced per year just from human urine (240 million tons of urea each year).[21-24] Electrochemical oxidation has been recognized as an efficient strategy for urea conversion and wastewater remediation.[25-27] Thus, the chemical energy harvested from urea/urine can be converted to electricity *via* the urea oxidation reaction (UOR).[13, 28, 29] Moreover, the removal of urea from water is a priority for improving drinking water quality and presents an opportunity for UOR.[30] However, the transition of UOR from theory and laboratory experiments to real-world applications is largely limited by the conversion efficiency, catalyst cost and the feasibility of wide-spread usage.[31]

---

[2] Chapter 2, in full, is a reprint of the research paper titled 'Highly efficient urea oxidation via nesting nano-nickel oxide in eggshell membrane-derived carbon' as it published on the journal of ***ACS Sustainable Chemistry & Engineering***. Shun Lu, Matthew Hummel, Zhengrong Gu, Yucheng Wang, Keliang Wang, Rajesh Pathak, Yue Zhou, Hongxing Jia, Xueqiang Qi, Xianhui Zhao, Ben Bin Xu, Xiaoteng Liu. 2021, 9(4): 1703-1713. Shun Lu was the primary investigator and first author of this article.

Primarily, the electrooxidation of urea has relied on cost-prohibitive rare metals such as ruthenium, platinum, tantalum, or iridium as the urea catalysis.[29, 32] Recent studies implementing common transition metals and their oxides, particularly nickel, have found similar success while having much lower material costs.[33-35] For instance, Luo et al. prepared ultrathin and porous nickel hydroxide nanosheets for efficient UOR and found that 1.82 V (*vs.* RHE, Reversible Hydrogen Electrode) was needed to achieve a large current density of 298 mA cm^{-2}.[36] Qiao et al. reported a two-dimensional nickel-based metal-organic framework (2D Ni-MOF) nanosheet by coordinating nickel ions and benzenedicarboxylic acid. The electrochemical results showed better UOR performance and smaller overpotential compared to $Ni(OH)_2$ and the commercial Pt/C.[13] Similarly, Ma et al. investigated Ni-MOF with different morphologies such as, nanowires, neurons, and urchins, and found that the Ni-MOF nanowires required ~0.8 V (*vs.* Ag/AgCl) to obtain a current density of 160 mA cm^{-2}.[37] Thus, based on the previous studies, the nickel-based materials' electrocatalytic behavior is well understood, making them ideal candidates for UOR.[38, 39] However, the kinetics of UOR at the anodic area is still sluggish owing to the multi-electron transfer and multiple gas-adsorption/desorption procedures.[11, 38-41] To address this key issue, the coordination of high surface area and conductive materials are considered beneficial.[42-44] Expanding the electrochemically active surface area, the bio-derived carbon doped nickel can provide the electrochemically active high surface area and conductivity in the material selection, resulting in efficient substrates.[45] Innovations with UOR from organic and bio-derived compounds have yielded substantial improvements in energy production efficiency.[46, 47]

Biomass-derived carbon materials have been increasingly implemented in electrochemical energy conversion and detection owing to their low-price, porous structure and high conductivity.[48] Hierarchical porous activated carbons are favored in particular due to their variety in pore size and volume, the potential for modification, and synthesis from waste biomaterials.[49, 50] One promising material that has demonstrated notable electrochemical properties is the eggshell membrane (ESM). ESM is a thin, protein-based membrane functioning as a gas-exchange interface for the embryo within the egg to the outside world via its abundant micro- and nano-sized pores. [51] Aside from the traditional methods of waste management, ESM has been used in the production of clean energy where it replaces coal, oil or natural gases to generate electricity through fuel cell devices. ESM collected from waste eggshells has demonstrated excellent electrochemical behavior on its own in energy storage and conversion [52, 53] as well an ability to be infused with different transition metal oxides for sensing purposes.[54, 55]

In this work, we reported a low-cost UOR electrocatalyst (C@NiO), composed of nickel oxide nanoparticles anchored on porous carbon derived from the biowaste eggshell membrane *via* hydrothermal synthesis and pyrolysis strategy. Benefiting from the strong synergistic effect between nickel oxide and the porous carbon, the as-prepared electrode only needs 1.36 V *versus* RHE to realize 10 mA cm^{-2} in 1.0 M alkali solution containing 0.33 M urea, and delivers 25 mA cm^{-2} at 1.46 V. In addition, from the viewpoint of the theoretical calculations, its intermediate (C@NiOOH), which formed from C@NiO in alkaline solution, gave this electrocatalyst possessing the ability to effectively hinder "CO_2 poisoning", as well as ensuring its superior performance for UOR. This work also presented the low-cost urea oxidation

electrocatalyst design with the porous structure to solve the previous problems we described (source and cost) and promote the catalyst's potential application in energy conversion based on the concept of "trash to treasure".

2.2 Experimental

2.2.1 Preparation of the porous C@NiO nanocomposites

Before obtaining C@NiO nanocomposites from the biowaste eggshell membrane, the ESM received pre-treatments to remove the egg white and other organic chemicals. C@NiO nanocomposites were prepared through a smart approach that the eggshell was not only employed as a reactor, but also the eggshell membrane as a filter membrane, as presented in Fig. 2.1. First, the eggshell filled with $Ni(NO_3)_2$ aqueous solution was transferred into a beaker with urea, then kept at 70 ℃ for 6 h. In this process, $Ni(OH)_2$ was synthesized on the interface of the eggshell membrane as OH^- ions (outside of ESM) were reacted with Ni^{2+} ions (inside of ESM). Then, the eggshell membrane was stripped from the eggshell reactor by tweezers after the reaction system was naturally cooled down. The stripped ESM was washed thoroughly with deionized water. Completely, black powder was received after calcination at 500 ℃ for two hours in N_2 environment. The calcined black powder with a metallic color was washed and collected for further characterizations.

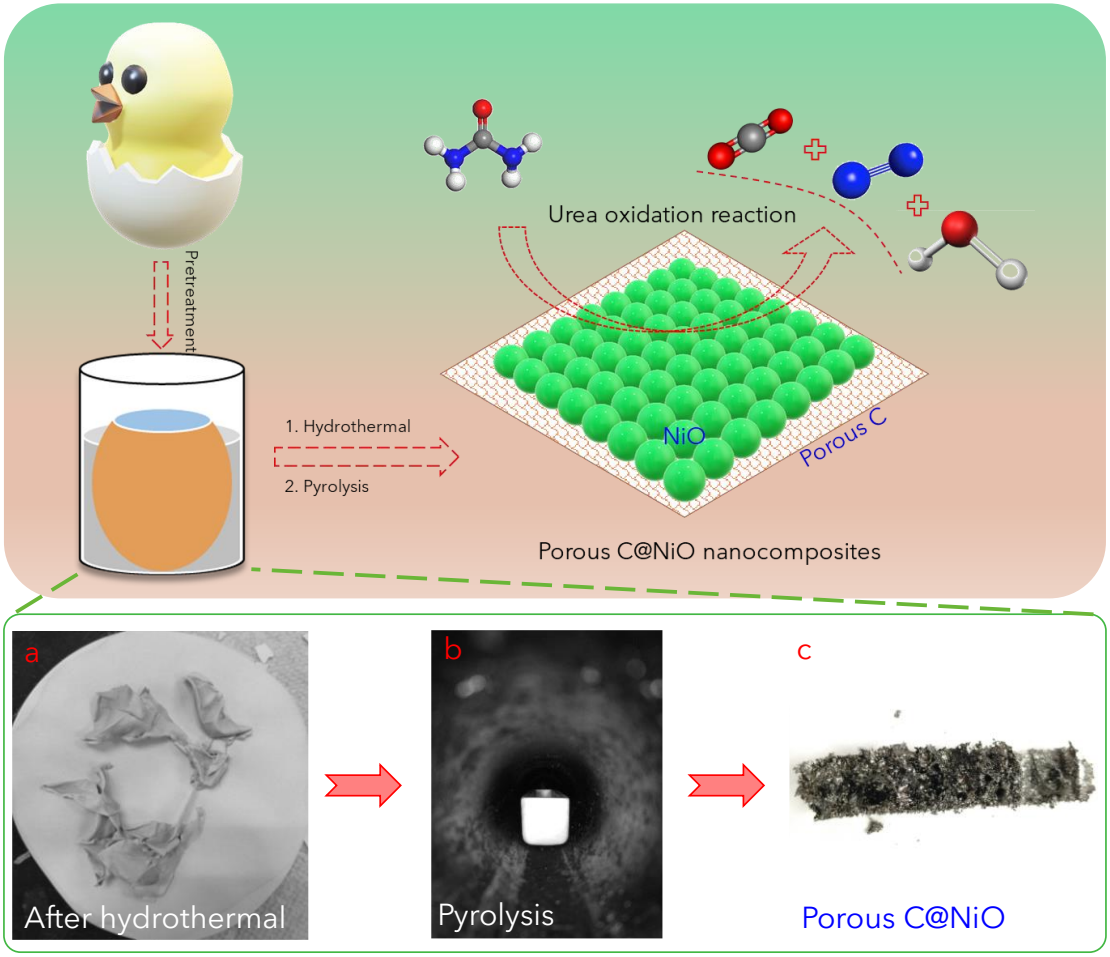

Figure 2.1 Scheme of the formulation process of the porous C@NiO nanocomposites: (a) dried NiO/ESM after the hydrothermal process, (b) pyrolysis treatment, and (c) final product after the pyrolysis.

2.2.2 Physical characterizations

The scanning electron microscopy (SEM) and transmission electron microscopy (TEM) were both employed to observe the as-prepared samples' morphological information and equipped with high-resolution TEM (HRTEM) and select area electron diffraction (SAED). Scanning transmission electron microscopy energy dispersive X-ray (STEM-EDX) spectroscopy was employed for analyzing the element distribution. The pyrolysis process was investigated to indicate the synthesis of C@NiO nanocomposites through the thermogravimetric analysis (TGA) measurement in the nitrogen gas environment.

TGA was performed by an integrated thermal analyzer with a ramp rate of 20 °C min^{-1} under N_2 protection. Furthermore, X-ray diffraction (XRD) was used for analyzing the crystalline structure of the as-obtained sample. X-ray photoelectron spectroscopy (XPS) spectra were carried out to analyze the surface compositions and chemical valence information for the as-prepared sample. All binding energies were referred to as the C 1s peak of the surface adventitious carbon at 284.8 eV.

2.2.3 Electrochemical measurements

All electrochemical measurements of urea oxidation were performed on a CHI (760E, Texas, USA) electrochemical analyzer. The conventional three-electrode testing configuration was used in all electrochemical measurements. A glassy carbon electrode (Ø 3 mm) was used as the working electrode (WE) and would receive catalyst modification, Pt electrode and Ag/AgCl (within saturated KCl solution) were selected as counter and reference electrodes (CE and RE), respectively. Considering different concentrations of urea used for oxidation, such as 0.1 M, 0.33 M and 0.5 M, 0.33 M urea was selected for oxidation measurements in this study to match the concentration in mammal urine.[56, 57] Cyclic voltammetry (CV) and linear sweep voltammetry (LSV) or polarization measurements were both carried out in a 1.0 M alkali solution with/without 0.33 M urea. Electrochemical impedance spectroscopy (EIS) spectrum was also investigated in 0.1 M potassium ferricyanide solution (frequency range: 100 kHz-0.1 Hz, AC perturbation: 5 mV, applied potential: open-circuit potential). Electrochemical double-layer capacitance (C_{dl}) tests were performed through a series of CV tests using a series of scan rates (2-10 mV s^{-1}) in 1.0 KOH with a similar potential range (0.06-0.16 V *vs.* Ag/AgCl). Chronoamperometry (CA) measurements were

carried out at a constant potential of oxidation peak potential *vs.* Ag/AgCl for 1800 s in 1.0 alkali media with 0.33 M urea. Here, the loading mass of the catalyst on the working electrode was calculated as 0.075 mg cm^{-2}, and all potentials mentioned in this study were converted versus a reversible hydrogen electrode (RHE): ($E_{RHE} = E_{Ag/AgCl} + 0.21$ V + 0.059×pH, 25℃) unless otherwise specified, and *iR* compensation was performed for all linear LSV results.

2.2.4 DFT calculation methods

To study the source of the highly electrocatalytic performance of C@NiO nanocomposites, calculations were carried out using spin-polarized density functional theory (DFT), equipped with the CASTEP package with the Perdew-Burke-Ernzerh (PBE) generalized gradient approximation (GGA) exchange-correlation functional.[58] The adsorption of urea and CO_2 on the C@NiO was studied and compared with that on C@NiOOH, and the heterojunctions were chosen as our theoretical models. The core electrons were treated with Ultrasoft Pseudopotentials.[59] The cutoff energy for the plane wave expansion was 340 eV, and the Monkhorst-Pack k-point sampling was generated with a 2×2×1 grid. The convergence criterion for the structural optimizations was a maximum force of 0.05 eV/Å and a maximum displacement of 0.002 Å. A vacuum layer of 15 Å thickness was used along the z-direction to totally eliminate the interactions between different surfaces. The adsorption energy of urea or CO_2 over C@NiO and C@NiOOH was calculated according to the below Equation.1:

$$E_{ads} = E_{total} - (E_{slab} + E_{adsorbate}) \quad \text{Equation. 1}$$

Where E_{ads} is the adsorption energy, E_{total} is the total energy for the adsorption state, E_{slab} is the energy of the optimized surface of C@NiO or C@NiOOH and $E_{adsorbate}$ is the energy of mono urea or CO_2 molecule.

2.3 Results and discussion

2.3.1 Physical characterizations of the porous C@NiO nanocomposites

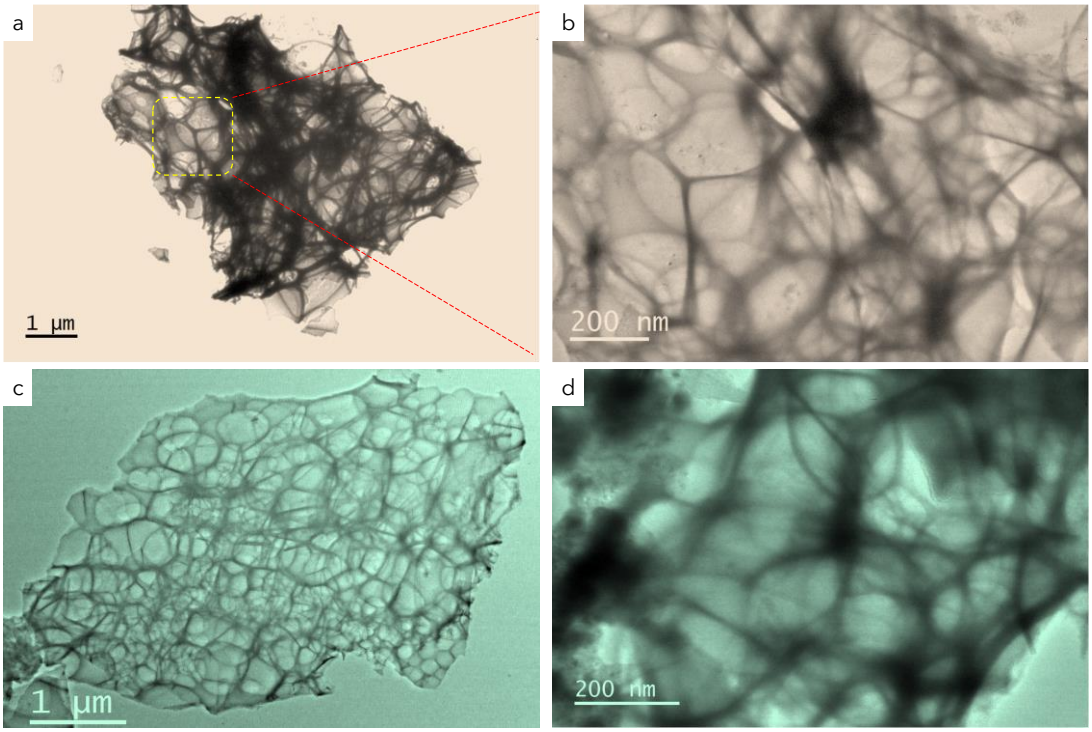

Figure 2.2 (a-b) TEM images of the porous carbon, (c-d) TEM images of the C@NiO nanocomposites.

There is a hierarchical structure of the porous carbon with transparent layers between carbon frameworks (Figs. 2.2a-b), indicating that it can provide a large surface area of active sites.[60] As depicted in Fig. 2.2c, NiO nanoparticles are anchored on the porous carbon frameworks. The color of carbon layers tends to be dark (Fig. 2.2d) and differs from Fig. 2.2b. This phenomenon may be due to the introduction of NiO nanoparticles.

STEM-EDX mapping was further applied to verify the composition of the as-prepared sample. The element distribution of Ni, O and C without other impurities on the transparent layers is observed well with higher magnification (~100 nm) in Figs. 2.3a-d. The porous structure is derived from the biomacromolecule fibers of ESM[52], with NiO nanoparticles dispersed well on the porous carbon, as presented in Fig. 2.3d.

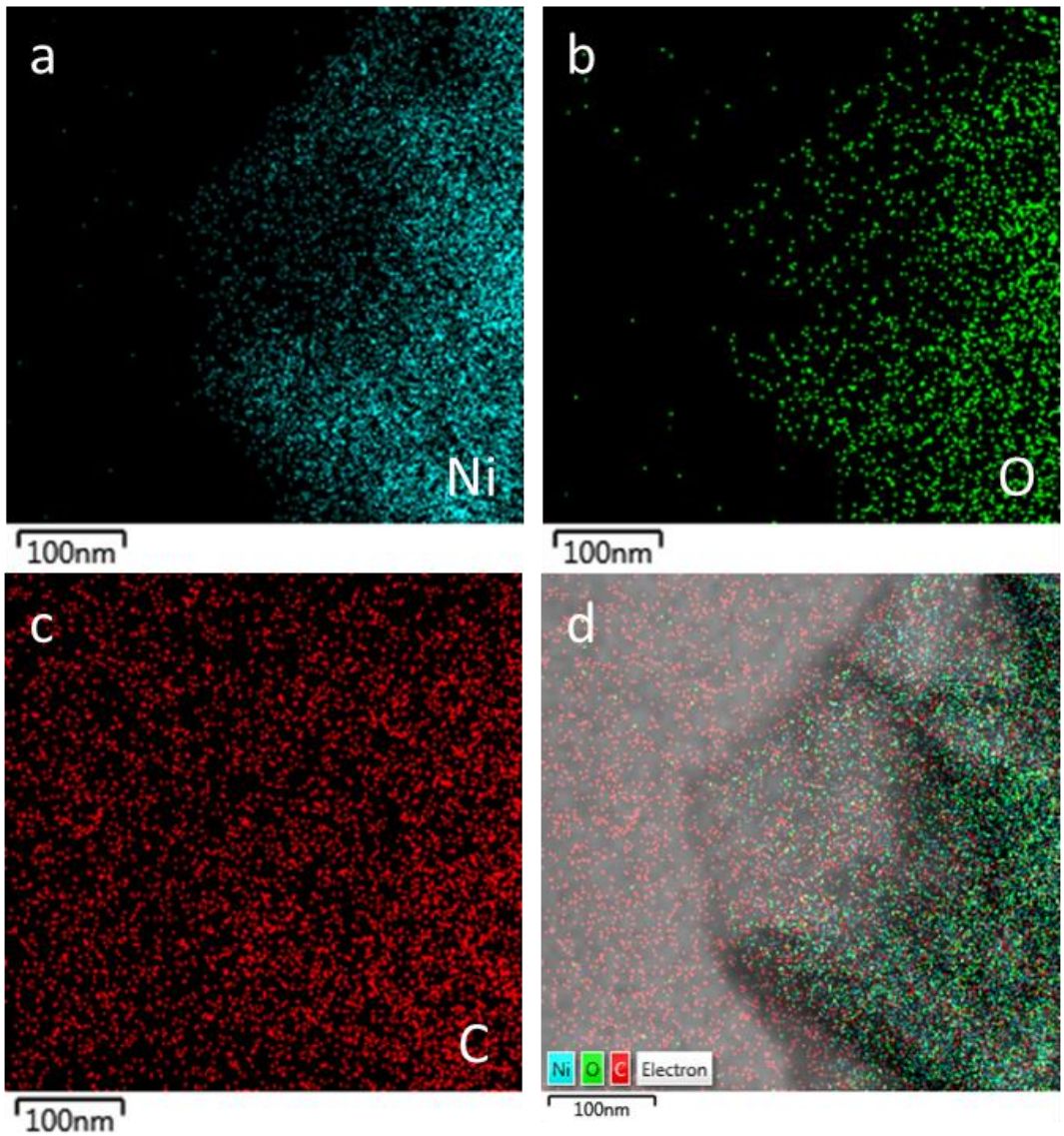

Figure 2.3 STEM-EDX images of the C@NiO nanocomposites (a) Nickel, (b) Oxygen, (c) Carbon and (d) the mixed results.

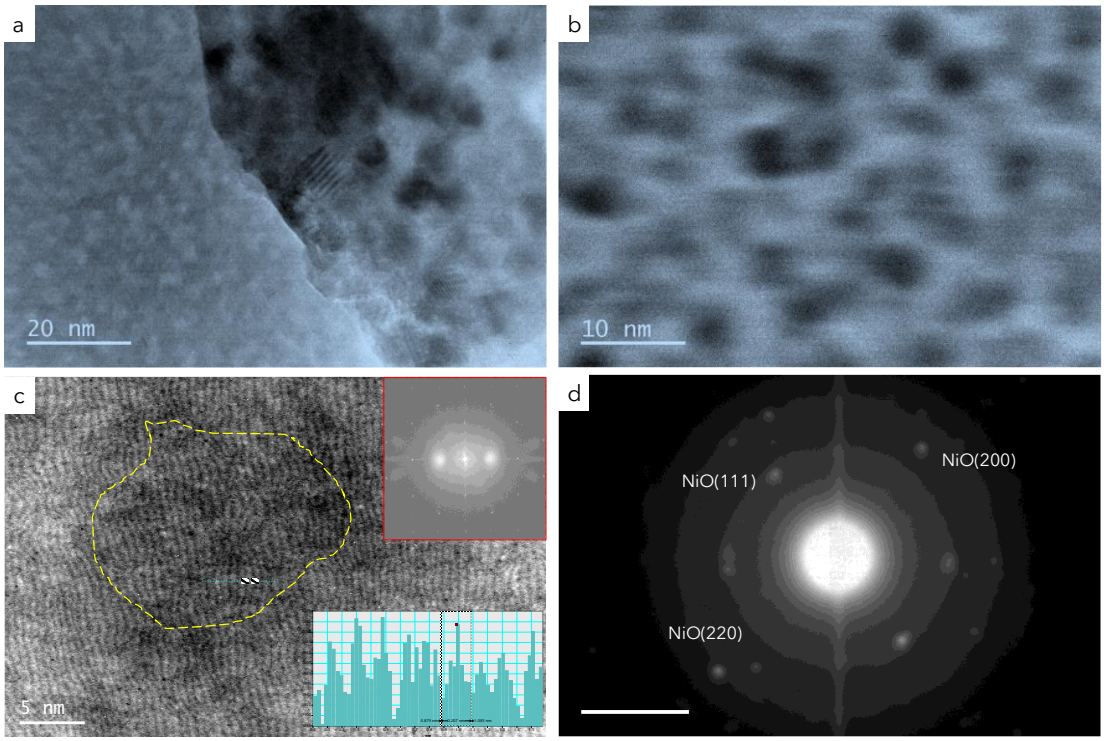

Figure 2.4 (a-b) TEM images with magnifications (20 nm and 10 nm), (c) HRTEM image and (d) SAED pattern of C@NiO nanocomposites.

Several black dots with an average size of 6.5 nm are displayed in Fig. 2.4a and Fig. 2.4b, confirming the existence of NiO nanoparticles. Fig. 2.4c exhibits the average lattice spacing of 0.207 nm in the dark area, which corresponds to the (111) fact of NiO (JCPDS No.47-1049). Fig. 2.5 also presents several similar areas with the same lattice spacing from Fig. 2.4c. Meanwhile, NiO grains encapsulated on the porous carbon also can be confirmed by its lattice fringes using fast Fourier transform (FFT) of HRTEM image due to NiO having specified unit cell parameters of 0.418 nm with face-centered cubic (fcc) structures (inset of Fig. 2.4c). As a comparison, pure NiO particles were synthesized using the same method and their morphology appeared as an aggregation of different sizes (Fig. 2.6) due to no supports in hydrothermal treatment process for good dispersion.[61] The SAED result of C@NiO nanocomposites in Fig. 2.4d reveals

the polycrystalline property with the feature of uniform central and diffraction spots. The diffraction rings have corresponded to the diffraction of the graphite-like carbon and the appeared spots are indexed to (111), (200), and (220) diffraction of pure NiO. All the above results demonstrated the porous C@NiO nanocomposite was successfully prepared with hierarchical structure and uniform dispersion.

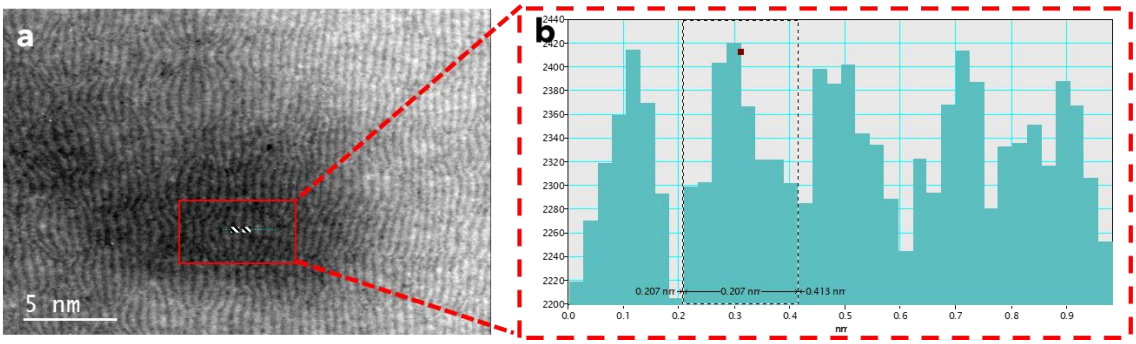

Figure 2.5 (a) HRTEM of different selected area in Fig. 2.4c with (b) the corresponding height profile.

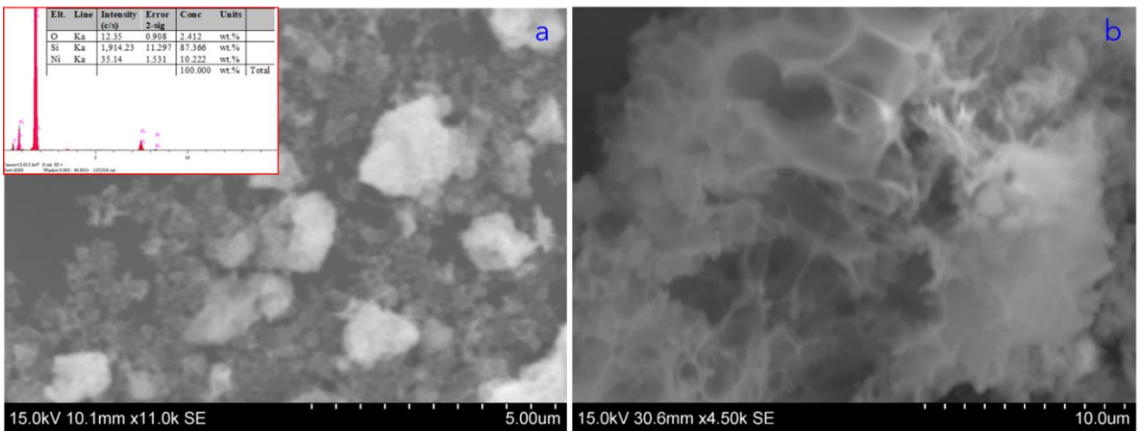

Figure 2.6 (a) SEM image of NiO particles, inset: EDX spectrum of NiO particles. (b) SEM image of the porous carbon.

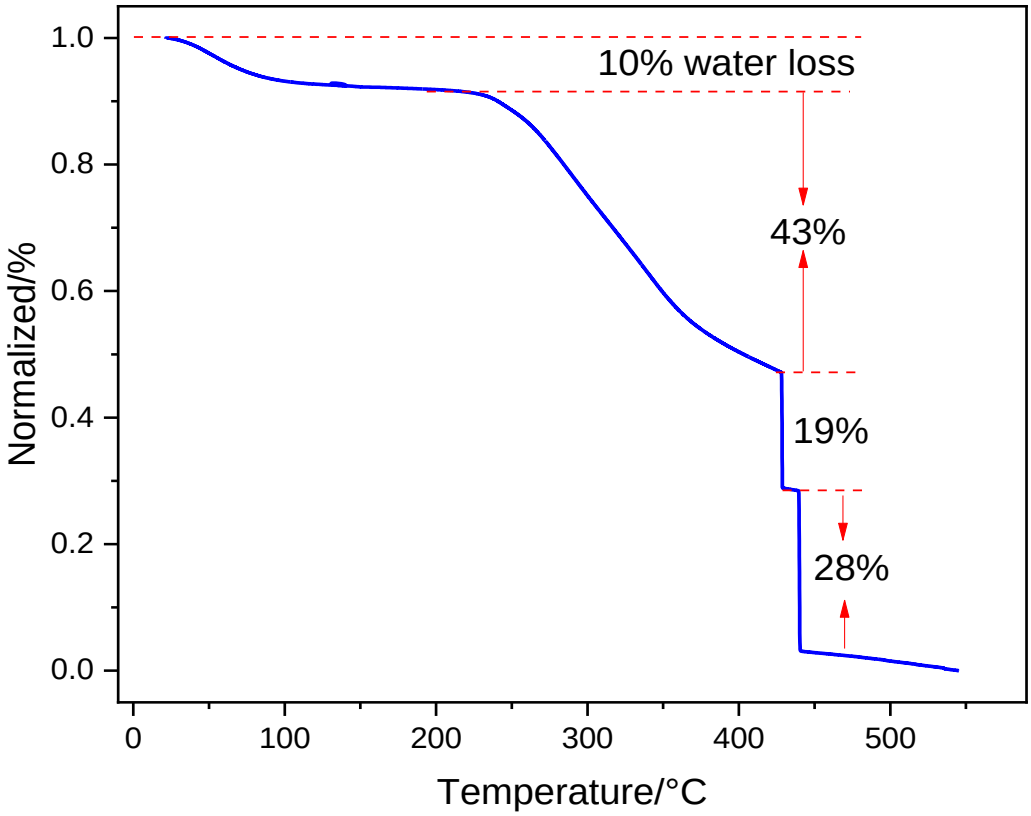

Figure 2.7 Figure S3. TGA curve of C@NiO nanocomposites.

TGA result of the precursor $Ni(OH)_2$/ESM is presented in Fig. 2.7. The precursor $Ni(OH)_2$/ESM endured a four-step weight loss owing to continuous dehydration and decomposition. The first stage (20-100 °C) is related to the evaporation of the adsorbed and intercalated water molecules associated with the surface of $Ni(OH)_2$/ESM. It is possible to estimate the water content (10 *wt.*%) of the precursor. ESM started pyrolyzing at ~200 °C and was completely pyrolyzed at 550 °C with a weight loss of 48 *wt.*%. Similarly, Zhai et al. found that decomposition of $Ni(OH)_2$ into NiO occurs between 300 and 400 °C.[62] For this step, the TG curve exhibits a sharp weight loss 19 *wt.*%, which is in line with the theoretical weight loss value (19.4%) due to the decomposition of $Ni(OH)_2$.[63] Organic components are completely removed by this

stage, including gas like CO_2, resulting in the uniformed NiO nanoparticles anchoring on the porous carbon. This result is consistent with previous TEM and SEM observations well.

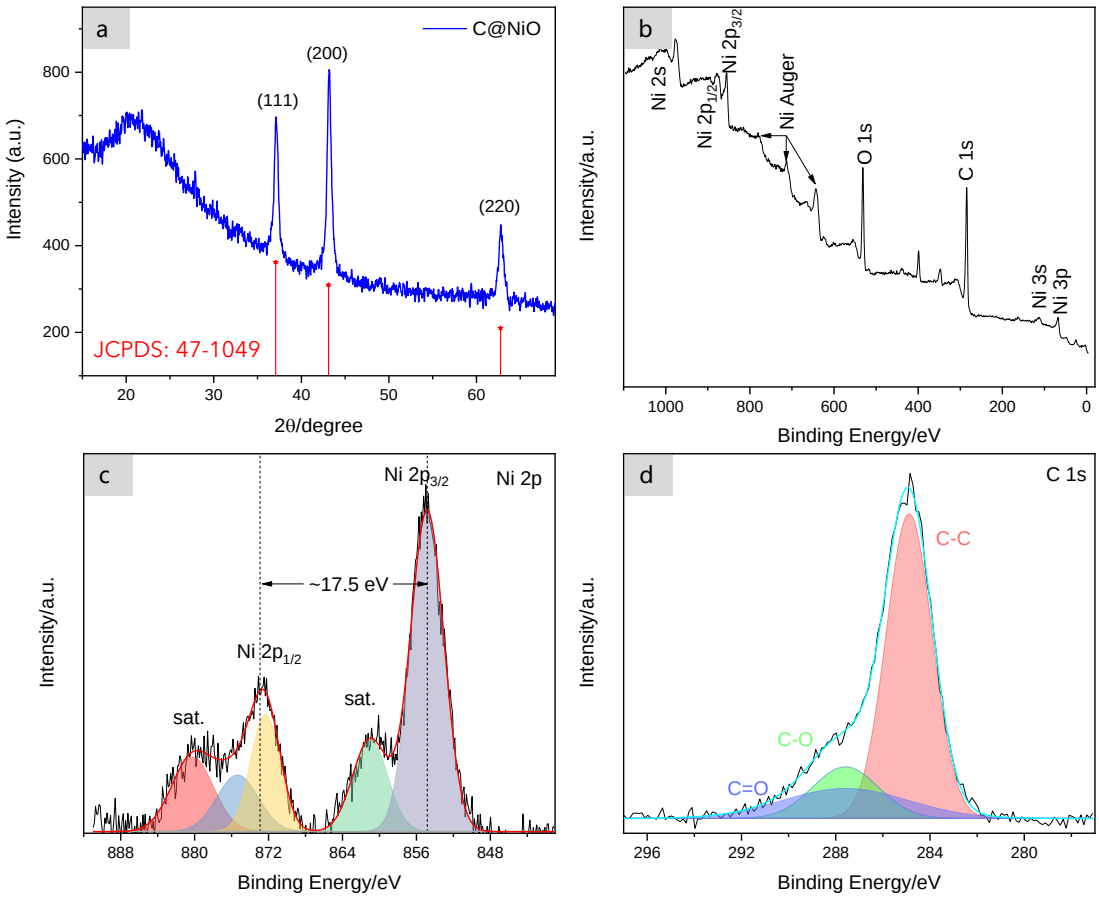

Figure 2.8 (a) XRD pattern, (b) XPS survey spectrum, and the high-resolution XPS spectra of (c) Ni 2p and (d) C 1s regions, of C@NiO nanocomposites.

In Fig. 2.8a, the peaks appeared at 37.2°, 43.2°, 62.8° (2θ), and are indexed to the crystal planes of NiO (JCPDS Card #47-1049) well. The peaks at 24.8° also confirmed the existence of carbon (JCPDS Card #41-1487). This XRD analysis identified the presence of NiO and C in the as-prepared sample, which also consistent with the HRTEM

pattern. The XPS survey spectrum of C@NiO nanocomposites further confirms the existence of nickel, oxygen, and carbon species in Fig. 2.8b. There are two apparent peaks located at 873.3 eV and 855.8 eV due to Ni $2p_{1/2}$ and Ni $2p_{3/2}$, as depicted in Fig. 2.8c. As a result, the binding energy peaks at 880 eV and 861 eV are assigned to the satellite peaks of Ni $2p_{1/2}$ and Ni $2p_{3/2}$, respectively. The spin-energy separation of two main peaks (from 873.3 eV to 855.8 eV) is ~17.5 eV, which is the typical characteristic of the $Ni(OH)_2$ phase[62], Nevertheless, all the Ni 2p peaks of the as-prepared sample shift to higher binding energies compared to $Ni(OH)_2$, implying a higher oxidation state of Ni(II) ions in C@NiO nanocomposites.[13] The C 1s can be further fitted to three peaks located at 286.4, 285.8, and 284.2 eV, corresponding to carbonyl bond, carbon-oxygen bond, and carbon-carbon bond in Fig. 2.8d. The above results further confirmed that the successful growth of NiO nanoparticles anchored on the porous carbon used to prepare C@NiO nanocomposites.

2.3.2 UOR performance of the porous C@NiO nanocomposites

To assess the electrocatalytic performance of C@NiO nanocomposites for urea oxidation, electrochemical measurements were applied through a typical three-electrode setting. Urea electrolysis reaction in alkaline environmental can be expressed as following (Equations.2-4):

Anode: $CO(NH_2)_2 + 6OH^- \rightarrow N_2 + 5H_2O + CO_2 + 6e^-$ Equations.2

Cathode: $2H_2O + 2e^- \rightarrow H_2 + 2OH^-$ Equations.3

Overall: $CO(NH_2)_2 + H_2O \rightarrow N_2 + 3H_2 + CO_2$ Equations.4

The electrochemical behaviours of the C@NiO electrode were evaluated by CV measurements in the alkaline medium in the absence/presence of 0.33 M urea and the pure NiO sample, and the porous carbon electrode were also tested for comparison, as shown in Fig. 2.9.

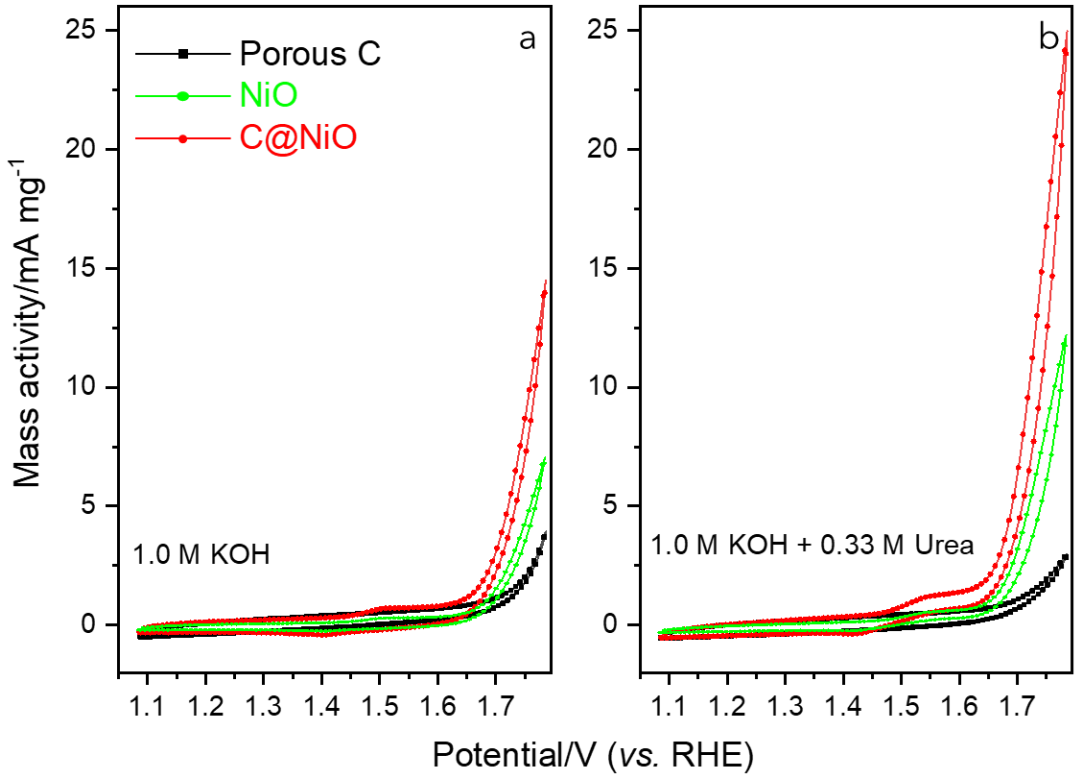

Figure 2.9 CVs of NiO, the porous carbon and C@NiO electrodes in the absence (a) and presence (b) of 0.33 M urea in 1.0 M KOH at a scan rate of 20 mV s^{-1}.

As for C@NiO electrode, there is an obvious oxidation peak at ~1.32 V, which can be attributed to the formation of NiOOH species.[11] However, C@NiO electrode presents an improved current density for urea oxidation after the addition of urea. Coincidentally, the onset potential of UOR is very close to the potential position where NiOOH species are generated, implying that the fresh NiOOH species acted as active

sites for urea oxidation, which is in line with the reported Ni-based electrocatalysts.[13, 55, 61, 64]

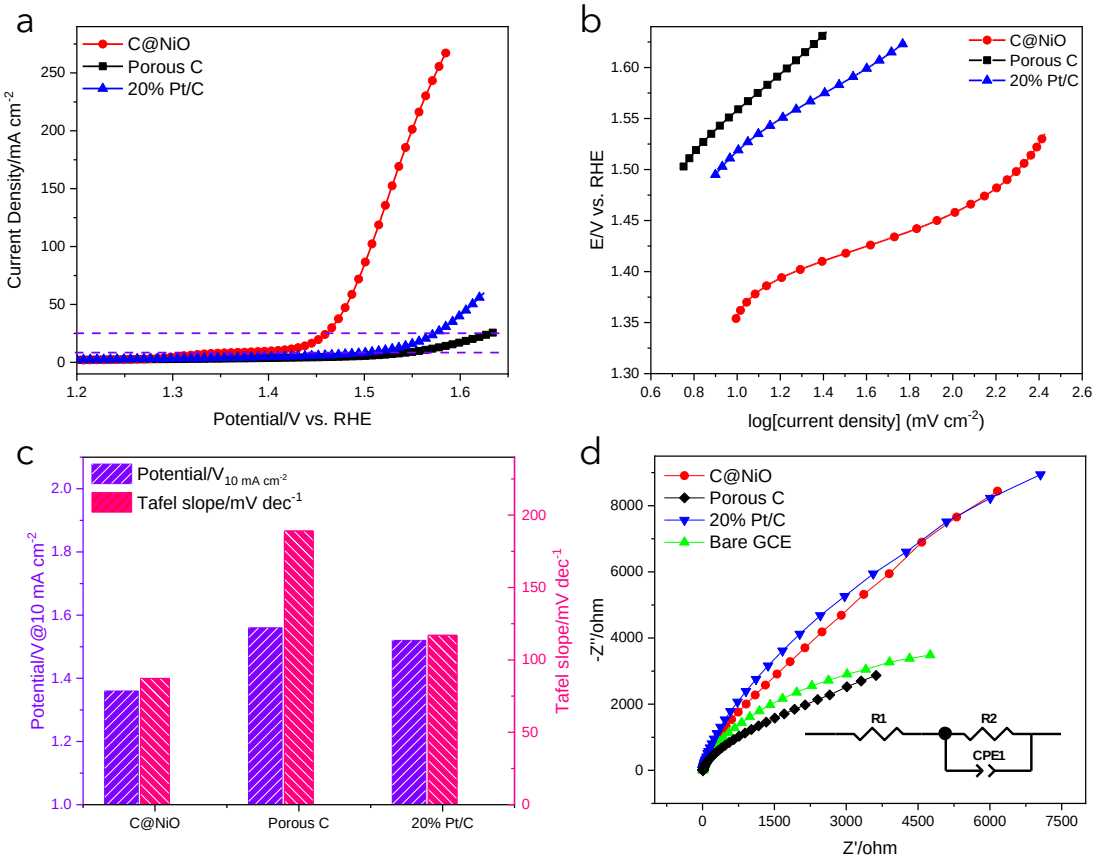

Figure 2.10 Electrochemical performance for UOR. (a) LSV curves of the porous carbon, 20% Pt/C and C@NiO electrodes in 1.0 M KOH containing 0.33 M urea, (b) Tafel plots of the above samples, (c) The histogram of a comparison of the potentials and Tafel slopes between the porous carbon, 20% Pt/C and C@NiO electrodes, (d) Nyquist plots of the porous carbon, 20% Pt/C and C@NiO electrodes in 1.0 M KOH with an open circuit voltage.

Furthermore, the integrated area of the CV of C@NiO electrode is larger than the porous carbon electrode, indicating that NiO nanoparticles anchoring the porous carbon exposed more active species for urea oxidation and enhanced the electrocatalytic performance of UOR. Fig. 2.10a reveals the linear sweep voltammetry curves of C@NiO electrode compared with the porous carbon and commercial 20% Pt/C in the alkali media containing 0.33 M urea. The current density of C@NiO electrode increases

with the potential moved towards the positive side, while the other two samples only show minor changes. The UOR catalytic performance of C@NiO is estimated by Tafel curves in Fig. 2.10b. A more intuitional comparison of potential (the current density of 10 mA cm^{-2}) and Tafel information among C@NiO electrode, the porous carbon and commercial 20% Pt/C can be found in the histogram (Fig. 2.10c), in which C@NiO electrode presents the lowest potential to attain 10 mA cm^{-2}. The Tafel slope of C@NiO (87.2 mV dec^{-1}) is also lower than those of the porous carbon and commercial Pt/C, implying faster UOR kinetics for C@NiO electrode.

As presented in Table 2.1, UOR performance of several electrocatalysts are listed. The C@NiO electrode presents a smaller potential and lower mass loading than that of the porous carbon and commercial Pt/C, suggesting the favorable reaction kinetics for UOR.

Table 2.1 Comparison of the UOR performance and mass loadings between recently reported electrocatalysts

Samples	Mass loading /mg cm^{-2}	Electrolyte	Potential /V vs. RHE 10 mA cm^{-2}	Ref./Year
Ni-MOF[a]	0.26	1.0 M KOH + 0.33 M Urea	1.36	[13]/2017
$Ni(OH)_2$	0.26	1.0 M KOH + 0.33 M Urea	1.46	[13]/2017
Pt/C	0.26	1.0 M KOH + 0.33 M Urea	1.64	[13]/2017

α-$Ni(OH)_2$	0.142	1.0 M KOH + 0.33 M Urea	1.39	[65]/2018
$Ni(OH)_2$-NMs[b]	--	1.0 M KOH + 0.33 M Urea	1.35	[66]/2019
NiO/Gr[c]	--	0.5 M NaOH + 0.3 M urea	1.33	[67]/2017
NiO/Gt[d]	--	0.5 M NaOH + 0.3 M urea	1.39	[68]/2017
$Ni(OH)_2$	0.285	1.0 M KOH + 0.33 M Urea	1.42	[35]/2019
NiCu/CNF[e]	28.05	1.0 M KOH + 1.0 M Urea	1.43	[69]/2019
NiCo LDH/$NiCo(OH)_2$[f]	--	5.0 M KOH + 0.33 M Urea	0.32 vs. Hg/HgO	[70]/2020
FeNi Oxide	--	1.0 M KOH + 0.33 M Urea	1.39	[71]/2020
C@NiO	0.075	1.0 M KOH + 0.33 M Urea	1.36	This work

a: MOF, metal-organic framework

b: NM, nanomeshes

c: Gr, graphene

d: Gt, graphite

e: CNF, carbon nanofiber

f: LDH, layered double hydroxide

2.3.3 Mechanism investigation via electrochemical measurements

EIS measurement was also tested to obtain more information about the catalytic performance of C@NiO nanocomposites. The porous carbon, 20% Pt/C and the bare GCE all received the same test for comparison. The results presented in Fig. 2.10d indicate that C@NiO electrode presents a much smaller Nyquist semicircle than that of the porous carbon, 20% Pt/C and the bare GCE under an open-circuit potential, revealing that it has a much faster charge transfer than other samples, which matched with the previous polarization curves as well.

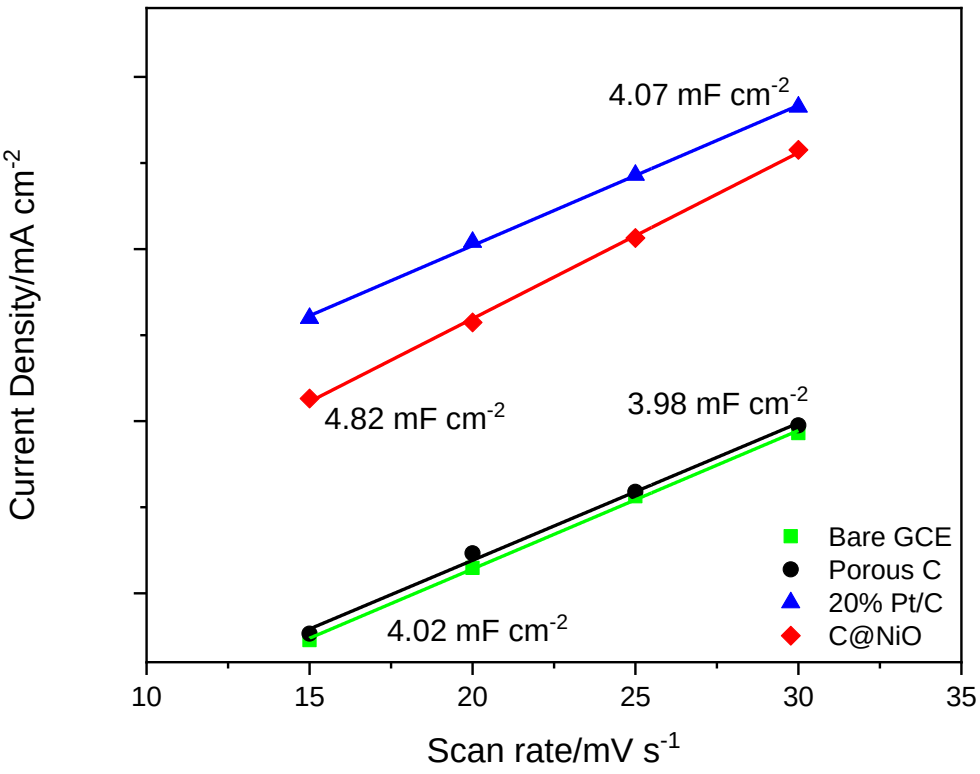

Figure 2.11 Linear plots of double-layer capacitance to assess the electrochemically active surface area.

Electrochemical active surface area (ECSA) measurements were further performed to study the electrochemical double-layer capacitance (C_{dl}) among C@NiO, the porous carbon, 20% Pt/C and the bare GCE. As demonstrated in Fig. 2.11, C@NiO electrode was calculated to be 4.82 mF cm^{-2}, well above the values of the porous carbon (3.98 mF cm^{-2}), 20% Pt/C (4.07 mF cm^{-2}) and the bare GCE (4.02 mF cm^{-2}). Calculation details can be found in Fig. 2.12. This means C@NiO electrode has larger active surface area with more active sites that promote UOR efficiently. In addition, the presence of urea increases the current density of the anode as the potential increase is applied.

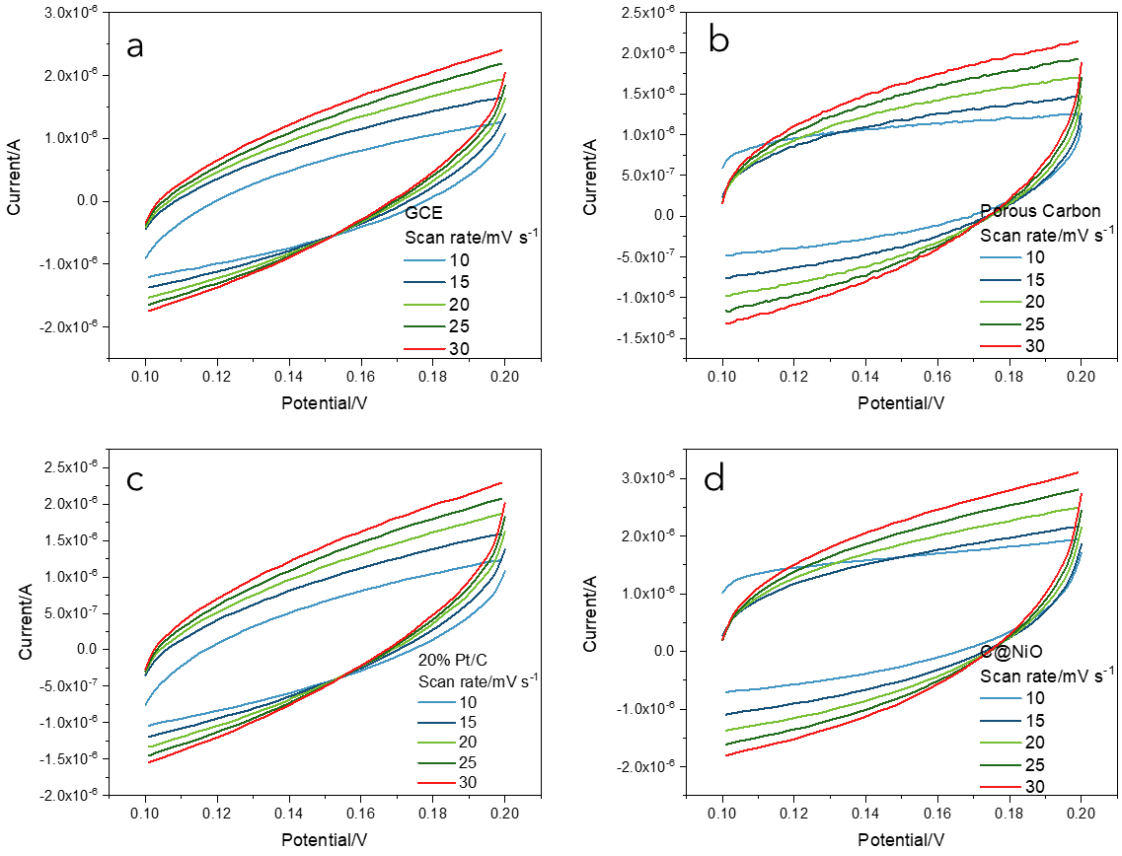

Figure 2.12 Cyclic voltammetry curves of (a) GCE, (b) The porous carbon, (c) 20% Pt/C and (d) C@NiO electrode measured in 1.0 M KOH solution at scan rates from 10 to 30 mV s^{-1}. Note: CV curves recorded in the non-faradaic region at different scan rates were presented in Fig. S5. The electrochemical double-layer capacitance (C_{dl}) is calculated according to the following formula: $j_c = VC_{dl}$ (a plot of j_c versus V gives out a straight line with a slope equal to C_{dl}).

As presented in Fig. 2.13, the current density of C@NiO electrode presents an increasing stepwise potential in 1.0 M alkali solution with/without 0.33 M urea. When the positive potential (0.1-0.4 V *vs.* Ag/AgCl) was applied, there are no redox cycles corresponding to the conversion of Ni^{2+} species to Ni^{3+} species before urea addition. When the potential (0.5-0.8 V *vs.* Ag/AgCl) larger than the onset potential was applied, a higher current density was obtained owing to the OER effect. It can be inferred that the porous C@NiO nanocomposites induce a high electron transfer and mass transport rate due to their excellent electrical conductivity.

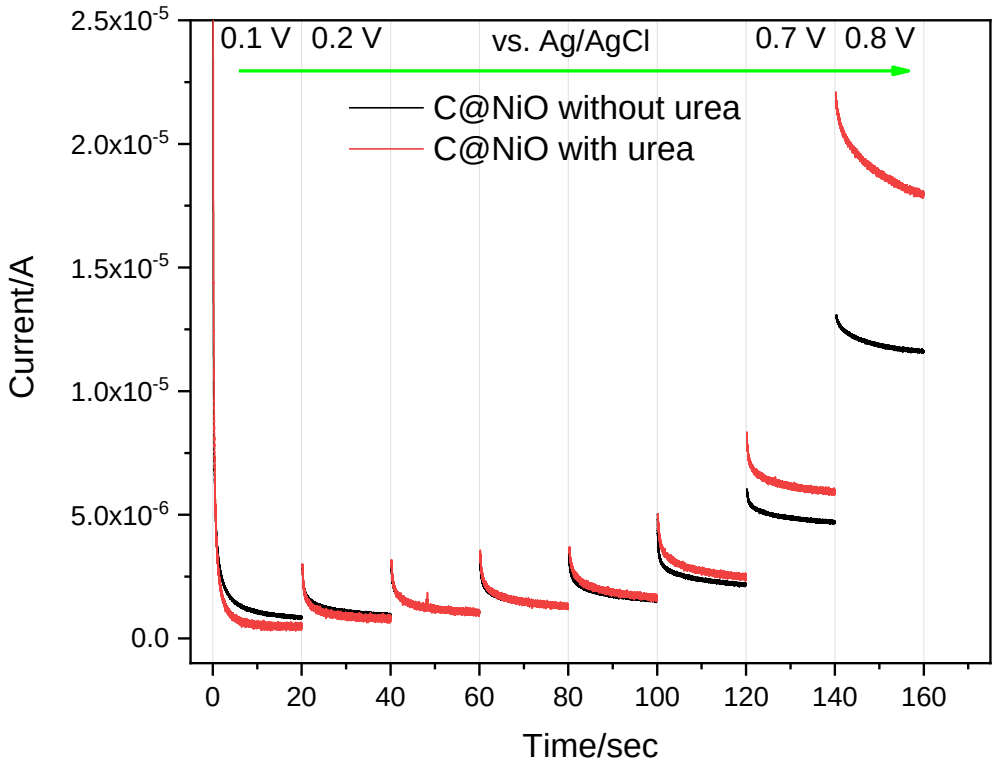

Figure 2.13 The current response at the different potential from 0.1 to 0.8 V vs. Ag/AgCl on the C@NiO electrode in the absence and presence of 0.33 M urea in 1.0 M KOH.

Moreover, the stable multistep chronopotentiometry (CP) curves also suggest better conductivity and mass transport of C@NiO electrode for UOR performance. The stability of C@NiO electrode during urea oxidation was further examined, as shown in Fig. 2.14. It can be observed that the current density of C@NiO electrode only shows negligible degradation compared with the commercial 20% Pt/C after 1800 s testing under an applied potential of 1.3 V *vs.* RHE. This indicates that C@NiO electrode has good catalytic stability in alkali with urea. To further confirm the structural stability after long-term durability, the stripped sample from the working electrode was observed again by the TEM technique. The original layer structure with uniform NiO nanoparticles was kept, as demonstrated in Fig. 2.15.

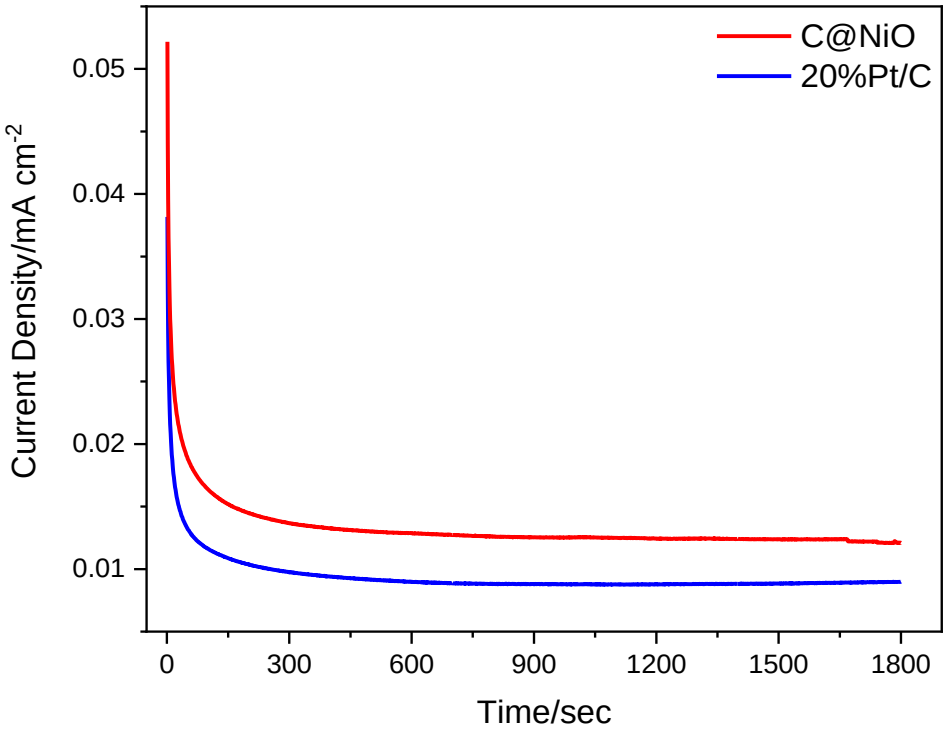

Figure 2.14 Chronoamperometry curves of C@NiO and 20% Pt/C in the 1.0 M KOH containing 0.33 M urea at an applied potential of 1.3 V (*vs.* RHE).

Consequently, it can be concluded that C@NiO electrode shows excellent UOR performance owing to i) NiO nanoparticles directly anchored on the porous carbon enlarge the electrochemically active surface area; ii) the transparent carbon layer could enhance its electrical conductivity, providing faster electron transfer and mass transport between nanoparticles and the carbon matrix, improving UOR electrocatalytic performance, reducing NiO nanoparticles direct contact with electrolyte, and thereby enhancing the stability.

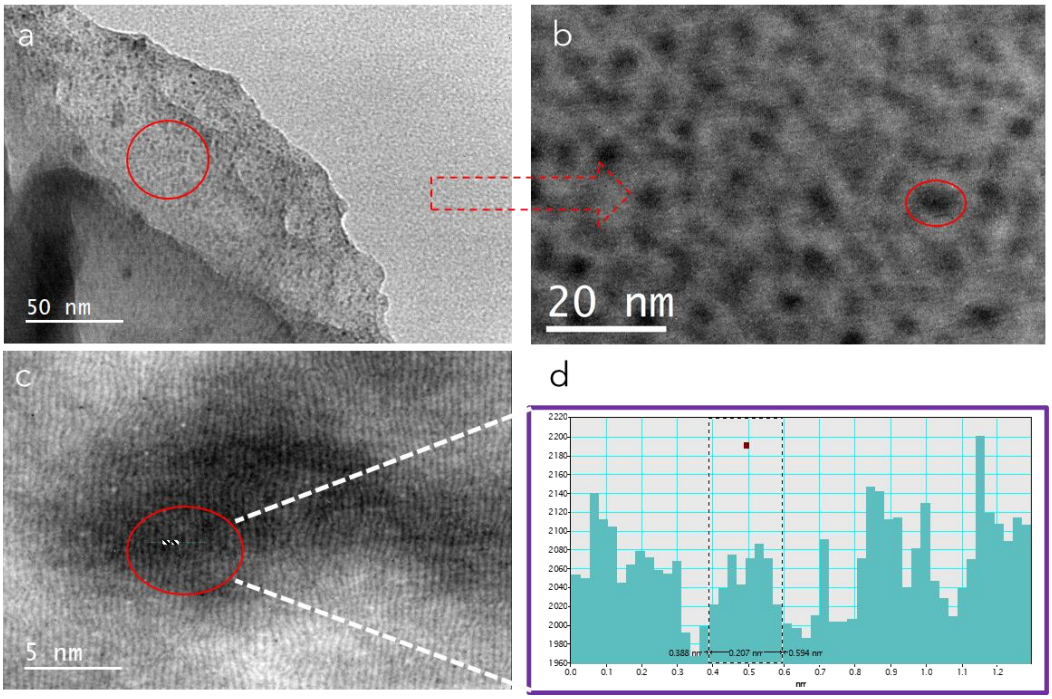

Figure 2.15 TEM images (a-b) of C@NiO nanocomposites after durability test, (c) HRTEM image of C@NiO nanocomposites and (d) with the corresponding height profile.

2.3.4 Mechanism investigation via theoretical calculations

To gain insight into the synergistic effect in C@NiO nanocomposites towards urea oxidation, spin-polarized DFT calculations were utilized to provide more details in this

work. Generally, $CO(NH_2)_2$ is primarily adsorbed on the surface of electrocatalysts during urea electrooxidation. It indicates that the adsorption energy of urea plays an important function in determining electrocatalytic urea oxidation[72]. It is noteworthy that our DFT calculations do not take all the experimental details into account, and the graphene was present as an alternative structure to simulate the porous carbon, qualitatively revealing the influence of the porous structure on the electronic structure of NiO nanoparticles. The graphene/NiOOH and graphene/NiO heterojunctions were chosen as the theoretical models in this work (Figs. 2.16a-b).

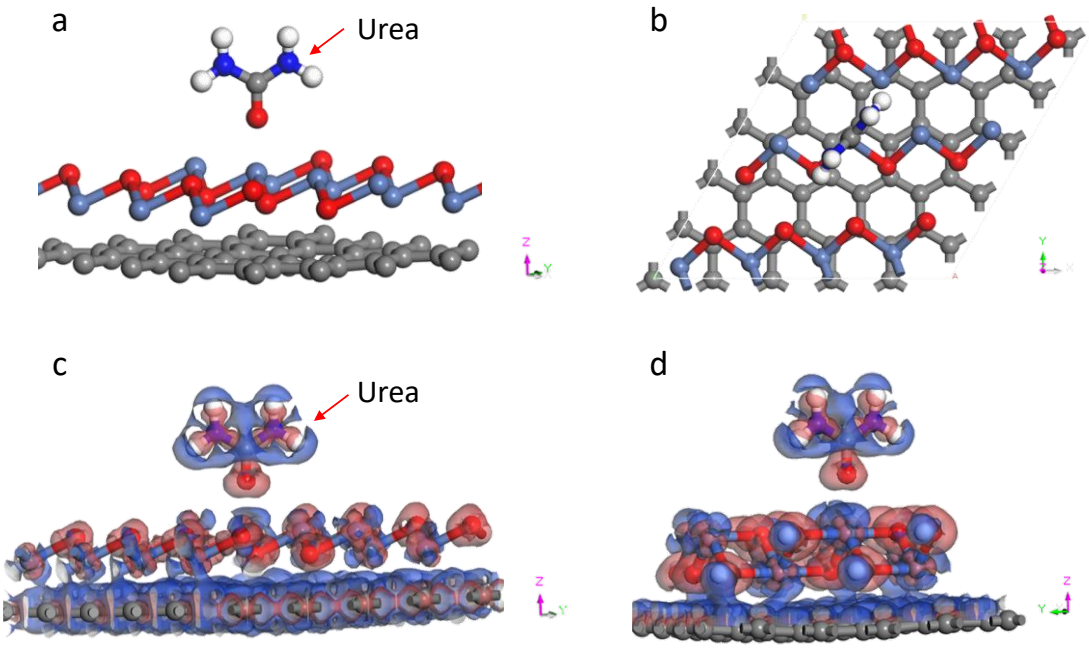

Figure 2.16 The structural model of the porous C@NiO and urea under different views (a-b). The electron density difference of urea adsorbed on (c) C@NiO and (d) C@NiOOH, the red hooded face means enrichment of electrons while the blue one means the deficiency of electrons.

According to the DFT calculations, the urea preferred to adsorb on the surface of C@NiOOH heterojunction and the adsorption energy is -1.53 eV, while the adsorption energy is only -0.97 eV on the C@NiO heterojunction (Fig. 2.17a). Moreover, the

electron density difference as shown in Figs. 2.16c-d, and the slice of electron density difference in Figs. 2.18a-b showed that a few more electrons from Ni transferred to the O atom of the urea on the C@NiOOH heterojunction than that on C@NiO heterojunction, which means that the alkaline environment plays an important role in the UOR, and it can be deemed that the Ni(III) species presented its favorable active sites.

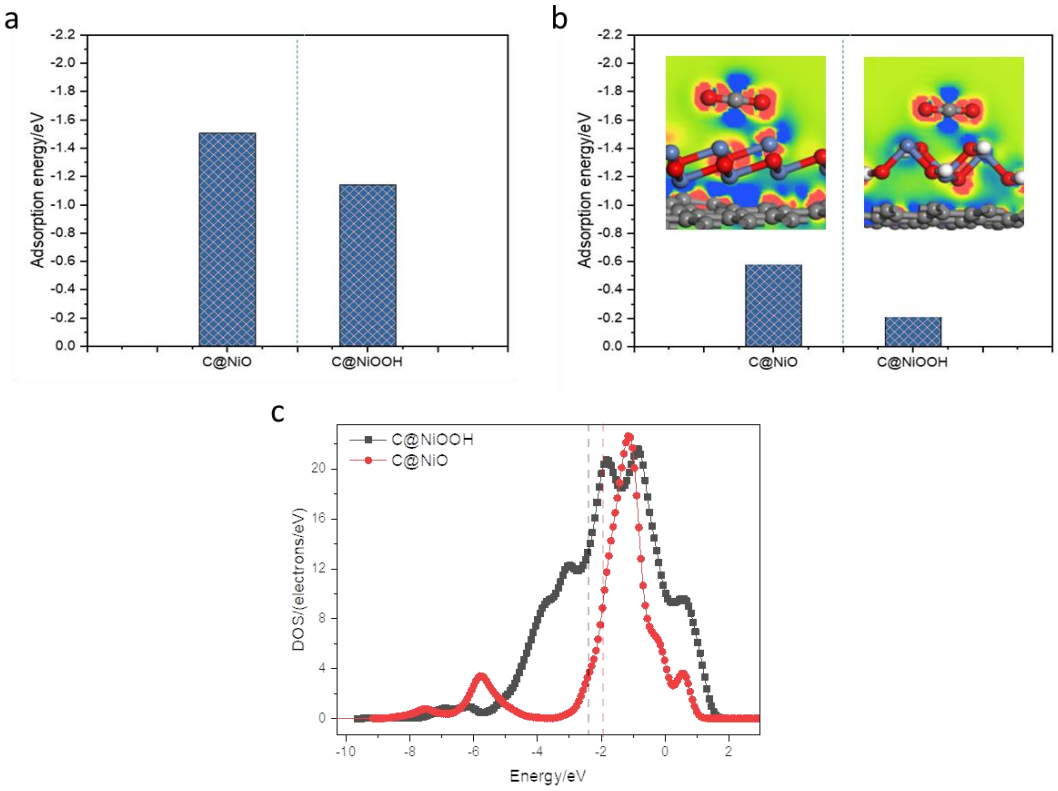

Figure 2.17 (a) The adsorption energy of urea on the porous C@NiO and C@NiOOH. (b) The adsorption energy of CO2 on the porous C@NiO and C@NiOOH, the inserted two pictures are the electron density difference of CO_2 adsorbed on C@NiO and C@NiOOH, respectively. The red area means enrichment of electrons while the blue means the deficiency of elections. (c) The d density of states of Ni in NiO (doted red line) and NiOOH (black line), respectively. The fermi level is set to zero, and the vertical lines represent the d band center.

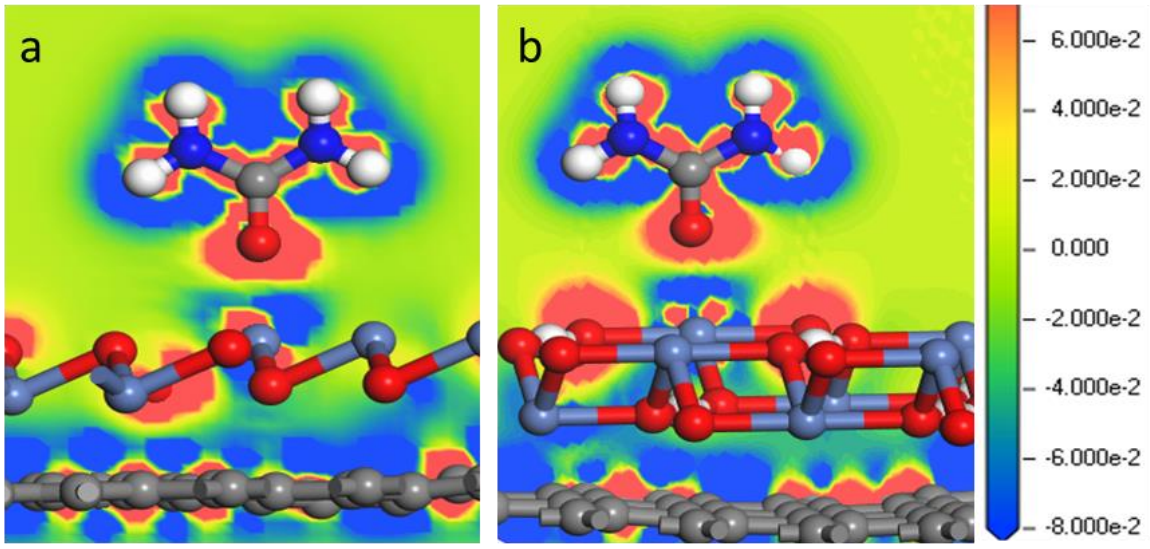

Figure 2.18 Slice images of the adsorption of urea molecule on the surface of (a) C@NiO and (b) C@NiOOH heterojunctions and the corresponding slice of electron density difference. The contour around the atoms represents the electron accumulation (red) or electron deletion (blue).

Besides, CO_2 adsorption on the surface or interface of the catalysts is significant to the remarkable UOR performance[73]. Moreover, the rate-determining step in UOR is the adsorbed CO_2 desorption from active sites[74]. Thus, the adsorption energy of CO_2 on C@NiO electrode and C@NiOOH was comparatively studied with DFT calculations. As illustrated in Fig. 2.17b, it can be determined that the adsorption energy of CO_2 on the C@NiO is -0.57 eV, while it becomes almost zero on the C@NiOOH surface, which means a much weaker CO_2 adsorption over C@NiOOH. Furthermore, the calculated d band center of Ni in C@NiO is -1.97 eV, while it is far from the Fermi level and decreases to -2.20 eV for the Ni in C@NiOOH (Fig. 2.17c). The lower d band center leads to the weaker adsorption for CO_2. From this viewpoint, it effectively retards the "CO_2 poisoning" of electrocatalyst, ensuring superior UOR performance.

2.3.5 UOR performance enhancement mechanism discussion

The improvement of UOR performance is mainly from the synergistic effect between NiO and the porous carbon, as illustrated in Fig. 2.19. It can be ascribed to several reasons, *i)* NiO nanoparticles directly encapsulated onto the porous carbon enlarged the electrochemically active surface area with more active sites. For example, 3D interwoven-like structure could afford more active sites and enable gas release from the reactions in the material preparation viewpoint. *ii)* The transparent carbon layer could enhance its electrical conductivity, providing faster electron transfer and mass transport between nanoparticles and the carbon matrix, improving UOR electrocatalytic performance, reducing NiO nanoparticles direct contact with electrolyte, therefore enhancing the stability. *iii)* The synergistic effect in C@NiO nanocomposites could regulate the electron density to optimize active sites and promote electrocatalytic UOR performance efficiently in terms of theoretical calculations.

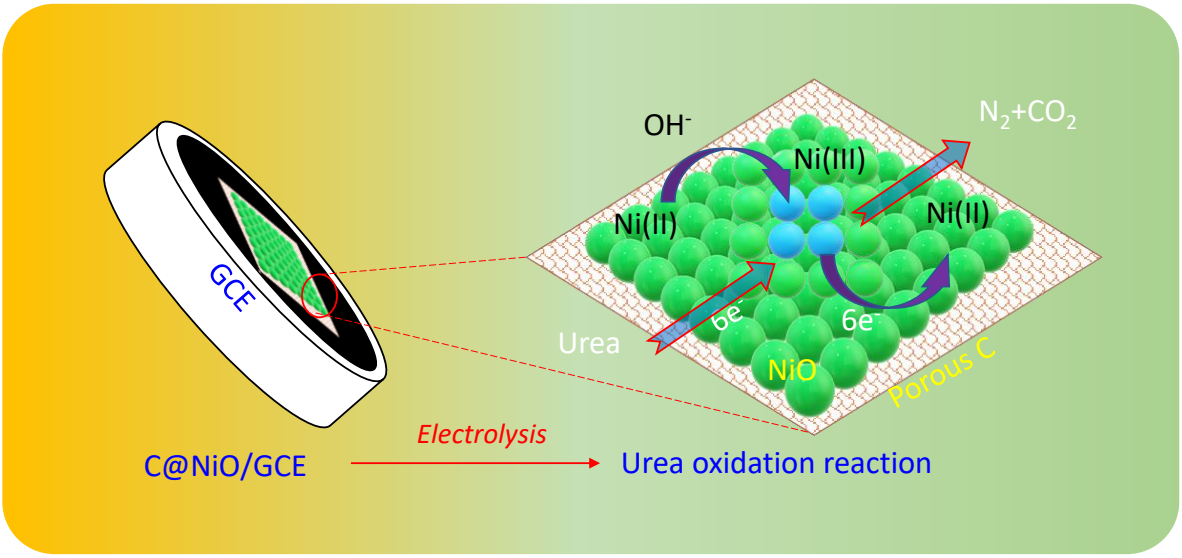

Figure 2.19 The mechanism of UOR on C@NiO electrode.

2.4 Conclusions

In summary, we have reported the nickel oxide nanoparticles supported on the carbonized eggshell membrane with interwoven networks as low-cost electrocatalysts (C@NiO) for urea oxidation. The resultant C@NiO electrode exhibited much better electrocatalytic urea oxidation performance than that of the commercial 20% Pt/C under the same test conditions. It can achieve a current density of 10 mA cm^{-2} at 1.36 V (*vs.* RHE) and 25 mA cm^{-2} at 1.46 V (*vs.* RHE) and a low Tafel slope of 87.2 mV dec^{-1}. Such an excellent urea oxidation performance could be attributed to the synergetic effect in the porous carbon and NiO nanoparticles which provides excellent electrocatalytic activity and stability in the C@NiO nanocomposites. Moreover, from theoretical calculations, Ni(III) species and the porous carbon further enabled the electrocatalyst to effectively inhibit "CO_2 poisoning" of electrocatalysts, guaranteeing its superior UOR performance. This study promotes the low-cost UOR electrocatalyst design with porous structure and uniform composition and develops biomass-derived applications in urea conversion based on the concept of "trash to treasure".

CHAPTER 3 DFT INVESTIGATION OF NIO@GRAPHENE COMPOSITE AS UREA OXIDATION CATALYST IN ALKALINE ELECTROLYTE[3]

3.1 Introduction

The continuous increase in the energy demand leads to the pursuit of a clean and renewable energy source because non-renewable energy sources such as traditional fossil fuels are limited and lead to global warming. It is necessary to bridge the gap between academia and industry with extensive research and their practical applications. Although hydrogen and oxygen evolution reactions (HER and OER respectively) have been considered as revolutionary fuel cell designs that utilize water-splitting technology, they suffer from efficiency drawbacks and can be used in a only pristine fresh water and with the use of noble metal catalysts.[75, 76] Urea oxidation reaction (UOR) is a fundamental step in fulfilling the need for practical green energy because they do not need high-voltage supply and also do not release O_2 and H_2 gases simultaneously, encountered during water splitting.[31] Furthermore, urea is an abundant component of human and animal waste, which can result in the production of problematic ammonia under normal degradation or standard hydrolysis practices.[77] More importantly, the UOR process could provide an opportunity for waste disposal and green hydrogen production.[78]

---

[3] Chapter 3, in full, is a reprint of the research paper titled 'Density Functional Theory Investigation of the NiO@Graphene Composite as a Urea Oxidation Catalyst in the Alkaline Electrolyte' as it published on the journal of ***ACS Omega***. Shun Lu, Matthew Hummel, Shuai Kang, Rajesh Pathak, Wei He, Xueqiang Qi, Zhengrong Gu. 2021, 6, 22, 14648-14654. Shun Lu was the primary investigator and first author of this article.

In a typical UOR, urea in an alkali electrolyte is subjected to a negative potential which drives the production of N_2 and CO_2 at the anode and H_2 on the cathode [79]. This process is depicted in Equations 1-3, respectively.

Anode: $CO(NH_2)_2 + 6OH^- \rightarrow N_2 + 5H_2O + CO_2 + 6e^-$ Equation. 1

Cathode: $6H_2O + 6e^- \rightarrow 3H_2 + 6OH^-$ Equation. 2

Overall: $CO(NH_2)_2 + H_2O \rightarrow N_2 + H_2 + CO_2$ Equation. 3

The UOR process is slow and inefficient under normal conditions due to the 6-electron transfer process from anode to cathode.[80, 81] Thus, it is necessary to modify the working electrode using a catalyst. Nickel-based materials are considered as one of the most promising groups of materials for catalysis in UOR owing to their low-cost, easy synthesis route, and abundanance in nature.[82, 83] For example, Tamman et al. developed a NiO modified electrode for electrocatalytic urea oxidation in the alkaline media and confirmed the UOR process is a completely irreversible diffusion-controlled route.[84] To improve the conductivity of Ni-based materials while maintaining the compound's catalytic performance, several effective strategies were applied, including the introduction of a conductive support[85], element doping[86], high valence Ni-based materials[87], and defect engineering[72]. Many of these effective strategies were developed to realize the commercial implementation of Ni-catalyst driven UOR. Nevertheless, the in-depth theoretical-fundamental understanding of the UOR were not studied due to its complicated multi-step gas adsorption and desorption process.

Moreover, one major theoretical drawback found by density functional theory calculation is the rate-limiting intermediate step of CO_2 desorption during the reaction on the anode.[73] In our previous work, we investigated the use of nano-NiO supported

on eggshell membrane-derived carbon for a Ni-catalyzed UOR, and the periodic heterojunction model was selected to illustrate the impact between the porous carbon and NiO nanoparticles.[85] Meanwhile, graphene was employed as the alternative porous carbon for simulations. It is important to add theoretical simulation to understand the UOR process using different models, especially for the existence of the single-atom model due to attractive findings.[88, 89] The in-depth mechanism of UOR with NiO@Graphene is still not clear. Consequently, it is useful to employ the single-atom model to investigate the role of NiO@Graphene in the UOR process.

In this work, a single-atom model was built to understand the relationship of NiO@Graphene composite and its urea oxidation behavior. The single-atom model, which differs from the previous theoretical model, was applied to illustrate the influence of between graphene and NiO nanoparticles. Meanwhile, this work also served as an important theoretical supplement for the previous research. Prior to the investigation of UOR, the adsorption of the hydroxyl group and urea on the NiO@Graphene was compared. Then, the adsorption of urea and CO_2 on NiO and NiOOH with graphene was calculated and compared. The electron density difference map was also used to study the electron transfer of NiO@Graphene composite.

3.2 Experimental

To understand the origin of the electrocatalytic urea oxidation mechanism of NiO@Graphene composite, density functional theory (DFT) calculations were conducted using the $Dmol^3$ package with the Perdew-Burke-Ernzerh (PBE) formulation of the generalized gradient approximation (GGA) program. The adsorption of urea and

CO_2 on NiO@Graphene was investigated and compared to that on NiOOH@Graphene, respectively. The single-atom structure was selected in this investigation. The core electrons were treated by DFT Semi-core Pseudopotentials. The DNP basis set was chosen as it can provide more precision for hydrogen-involved calculations. The convergence thresholds for energy change, maximum force and maximum displacement are set to be 2×10^{-5} Hartree, 0.004 Hartree $Å^{-1}$ and 0.005 Å, respectively. A vacuum layer of 15 Å thickness was employed along the z-direction to eliminate the interactions between different surfaces. In this work, the adsorption energy of urea or CO_2 is an important reference point for determining the activity and stability of a urea electrocatalyst. Therefore, the adsorption energy of urea or CO_2 over NiO@Graphene and NiOOH@Graphene were calculated according to Equation 4.

$$E_{ads} = E_{total} - (E_{slab} + E_{adsorbate}) \quad \text{Equation. 4}$$

where E_{ads} is the adsorption energy, E_{total} is the total energy for the adsorption state, E_{slab} is the energy of the optimized surface of C@NiO or C@NiOOH, and $E_{adsorbate}$ is the energy of single urea or CO_2 molecule. So, a more negative E_{ads} in equation 4 implies that the adsorption is thermodynamically more favorable.

3.3 Results and discussion

3.3.1 Competitive adsorption of urea/hydroxyl group on the NiO@Graphene

In earlier literatures of UOR towards NiO and its derivates, most of the theoretical studies have been performed by considering the adsorption/desorption of CO_2 in gas-liquid interface which matched well with the formed *COO species.[85] However, the

competitive adsorption of urea and hydroxyl group on the surface of NiO-based electrocatalyst cannot be ignored before urea oxidation. Thus, to understand the competitive adsorption, both the adsorption energy of urea and hydroxyl group were calculated, respectively. As shown in **Fig. 3.1**, the adsorption energy of hydroxyl group (route I) on the NiO@Graphene is calculated as -3.49 eV, which is higher than that of the adsorption energy of urea (route II). It means NiOOH@Graphene was formed easily in the alkaline media without the disturbing of urea adsorption.

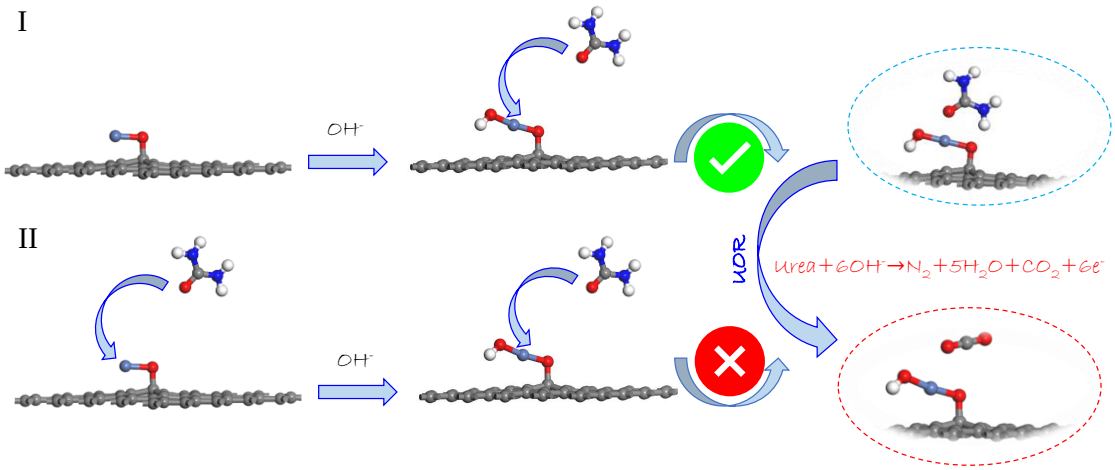

Figure 3.1 Schematic illustration of the adsorption route of urea/hydroxyl on the NiO@Graphene (grey for C atom, red for O atom, and blue for N atom)

3.3.2 Theoretical analysis on NiO@Graphene and NiOOH@Graphene

To get an understanding of the electrocatalytically urea oxidation mechanism of NiO@Graphene, DFT calculations were utilized based on the single-atom model. Generally, NiO(II) nanoparticles will be oxidized into NiOOH(III) in the alkaline environment, which is due to the redox reaction (Equation 5) occurring at the NiO(II) nanoparticles, as shown in Fig.3.1.

$$NiO + OH^- \leftrightarrow NiOOH + e^-$$ Equation. 5

$$Ni(OH)_2 + OH^- \leftrightarrow NiOOH + H_2O + e^-$$ Equation. 6

In a typical cyclic voltammetry diagram of pure NiO in the presence of alkaline electrolyte, the oxidation peak around 0.35 V corresponds to the transformation of Ni(II) to Ni(III), and the reduction peak around 0.15 V corresponds to the transformation of Ni(III) to Ni(II).[90] The formed Ni(III) species was regarded as the active sites for the UOR process. Before the research on nickel oxide, nickel hydroxide was first electrooxidized to NiOOH species in alkaline media (Equation 6), and then urea molecules adsorbed on the NiOOH species via bridging coordination, whereby a Ni atom interacts with a C atom (Urea). It means that the onset potential for the UOR is the potential for the formation of NiOOH via Ni electrooxidation. The next dissociation of urea on NiOOH is a multiple processes, producing a variety of intermediate species, such as the typical reaction pathway was proposed as: *$CO(NH_2)_2$ → *$CO(\cdot HNNH_2)$ → * $CO(\cdot HNNH)$ → *$CO(\cdot HNN)$ → *$CO(N\cdot N)$ → *$CO(OH)$ → *$CO(NH_2)_2$ → *$CO(OH\cdot OH)$ → *COO.

By analyzing the Gibbs energy and the resistance of each step (Table 3.1), they uncovered that the rate-determining step (RDS) is the desorption of CO_2 from NiOOH species. Thus, to simplify the DFT calculation, and the adsorption of CO_2 on the given composite was used to simulate the RDS process of urea oxidation.

Table 3.1 Gibbs energies (Δ G) for the possible steps on M (M = NiOOH).[73]

Reactions	Δ G/kJ mol^{-1}
$CO(NH_2)_2 + M \rightarrow [M{\cdot}CO(NH_2)_2]_{ads}$	66.2
$[M{\cdot}CO(NH_2)_2]_{ads} + OH^- \rightarrow [M{\cdot}CO(NH_2{\cdot}NH)]_{ads} + H_2O + e^-$	-28.9
$[M{\cdot}CO(NH_2{\cdot}NH)]_{ads} + OH^- \rightarrow [M{\cdot}CO(NH_2{\cdot}N)]_{ads} + H_2O + e^-$	-185.1
$[M{\cdot}CO(NH_2{\cdot}N)]_{ads} + OH^- \rightarrow [M{\cdot}CO(NH{\cdot}N)]_{ads} + H_2O + e^-$	75.4
$[M{\cdot}CO(NH{\cdot}N)]_{ads} + OH^- \rightarrow [M{\cdot}CO(N{\cdot}N)]_{ads} + H_2O + e^-$	-178.2
$[M{\cdot}CO(N{\cdot}N)]_{ads} + OH^- \rightarrow [M{\cdot}CO{\cdot}OH)]_{ads} + N_2 + e^-$	392.7
$[M{\cdot}CO{\cdot}OH)]_{ads} + OH^- \rightarrow [M{\cdot}CO_2)]_{ads} + H_2O + e^-$	-156.6
$[M{\cdot}CO_2)]_{ads} \rightarrow M + CO_2$	1242.2
Total	1227.7

Table 3.2 The DFT data for the adsorption of CO_2 and urea on the surface of NiO@Graphene and NiOOH@Graphene, respectively.

Species	Optimized energy/eV	Adsorption energy/eV	The shortest distance between CO_2 and catalyst/Å	The shortest distance between urea and catalyst/Å
NiO@Graphene-Urea	-11619.6959	-1.377778046	--	Ni-O: 1.920 O-H: 1.744
NiOOH@Graphene-Urea	-12072.8731	-0.77729845	--	Ni-O: 1.920 O-H: 1.744
NiO@Graphene-CO_2	-10569.1883	-0.628792601	Ni-O: 2.040	--
NiOOH@Graphene-CO_2	-11022.4195	-0.082424595	Ni-O: 2.569	--

Graphene was an alternative instead of the porous carbon in our previous work with many advantages of high-conductivity and stable support.[85] It is noted that, graphene preferentially anchors NiO nanoparticles via electrostatic attraction due to it is electronegative.[90] Hence, we concluded the connection of NiO on the given graphene substrate was achieved by the Ni-O-C bond. The optimized configurations are listed in Fig. 3.2, and the corresponding adsorption energies of urea and CO_2 molecule are listed in Table 3.2 and Table 3.3.

Table 3.3 The optimized energy for the adsorption of CO_2 and urea on the surface of NiO@Graphene and NiOOH@Graphene, respectively, based on our model.

Species	Optimized energy/eV
CO_2	-1028.03939
Urea	-2077.79804
NiO@Graphene	-9540.52016
NiOOH@Graphene	-9994.29777

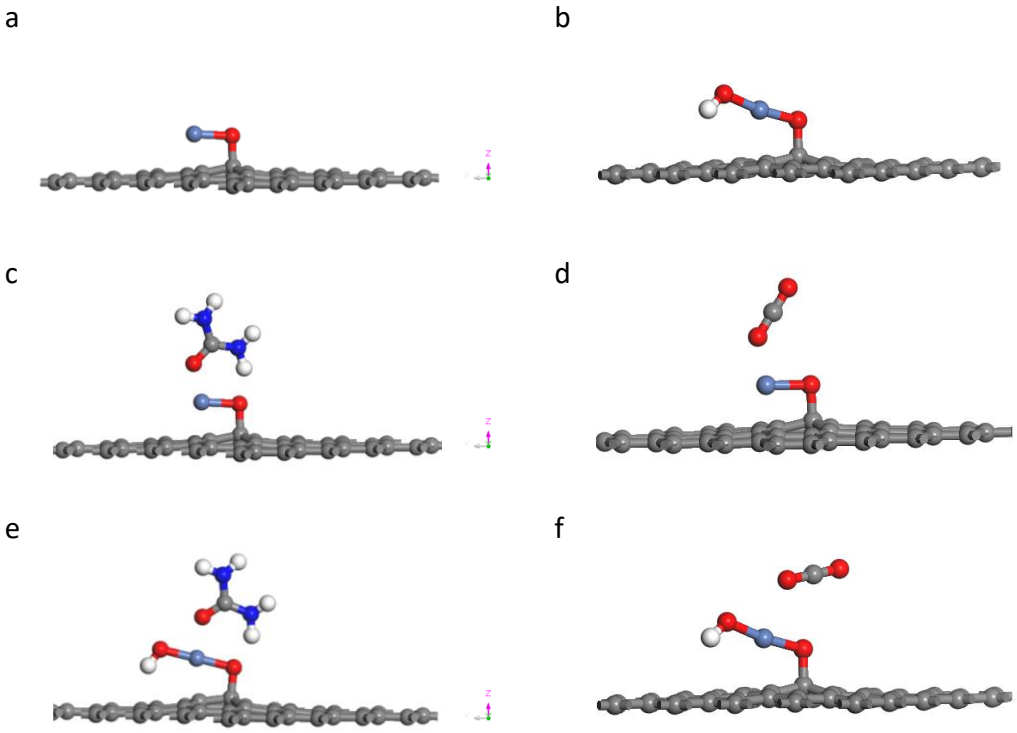

Figure 3.2 The optimized structure of (a) NiO@Graphene and (b) NiOOH@Graphene. The adsorption of urea (c) and CO2 (d) on the surface of NiO@Graphene, and the adsorption of urea (e) and CO2 (f) on the surface of NiOOH@Graphene. Red for oxygen, white for hydrogen, grey for carbon, blue for nitrogen, and light blue for nickel atoms.

Weaker adsorption energy generally corresponds to a more stable system. NiO nanoparticles reacted with the hydroxyl group in the alkaline to form NiOOH, followed by linking the graphene substrate through the Ni-O-C bond. In the case of NiO@Graphene composite, Ni(II) species were assumed to be the active sites, and urea molecules were attracted on the given composite. The most active site of NiO@Graphene composite adsorption is the Ni(II) species with an adsorption energy of -1.37 eV (**Fig. 3.3a**). This interaction may originate from the interaction (Ni-O: urea) between Ni 3d and O 2p orbital electrons of the urea molecule. However, the adsorption energy of NiOOH@Graphene toward the urea molecule is -0.77 eV. Ni(III) species acted as active sites for urea oxidation, the lower urea adsorption energy of

NiOOH@Graphene suggests that it does not adsorb urea well compared to the performance of NiO@Graphene. The possible reason for this phenomenon is the Ni-O: urea bond between NiOOH@Graphene and urea is affected by the around groups (i.e., OH^-). To verify this point, the adsorption energy of NiOOH@Graphene over hydroxyl group was calculated as -2.32 eV, which is a strong interaction. This result further confirms the above explanation and also illustrates that the urea adsorbed on the surface of the catalyst can accelerate the electrochemical process to some extent.

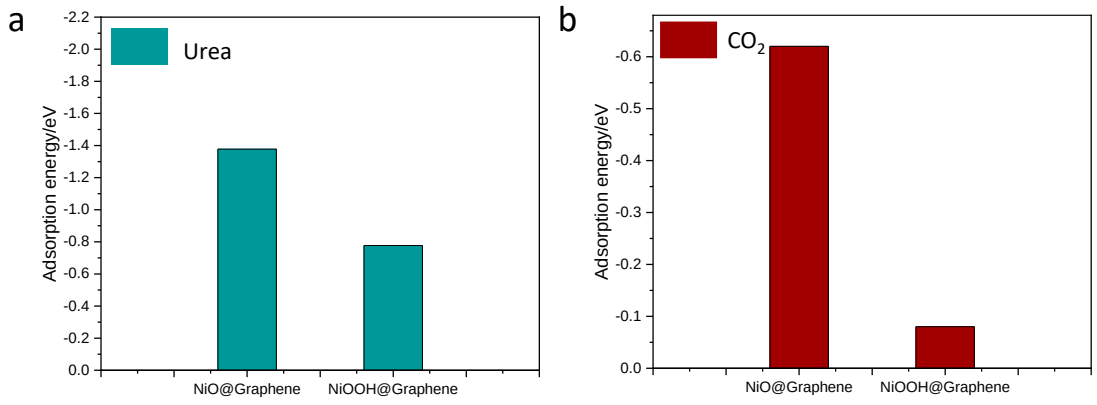

Figure 3.3 The adsorption energy of (a) urea and (b) CO_2 molecules on the NiO@Graphene and NiOOH@Graphene, respectively.

Moreover, the desorption step of CO_2 from Ni species is regarded as the rate-determining step for urea oxidation on the Ni-based electrocatalysts. Therefore, the adsorption of CO_2 on the NiO@Graphene and NiOOH@Graphene were calculated, respectively (Fig. 3.3b). The CO_2 adsorption of NiO@Graphene is -0.62 eV, which is higher than that of NiOOH@Graphene (-0.08 eV). It may be due to the molecule interaction between CO_2 and the catalyst. So, the distance between CO_2 and the catalyst is an important parameter to explain this phenomenon. Consequently, the shortest distance between CO_2 and NiO@Graphene is 2.040 Å, which is slightly smaller than

that of NiOOH@Graphene (Figs. 3.4-3.5). This result further confirms the NiOOH@Graphene easily desorbed the CO_2 molecule during urea oxidation. Moreover, as evidence for Ni(III) species playing the active sites for efficient urea oxidation. This result also is further explained by the electron density difference diagrams.

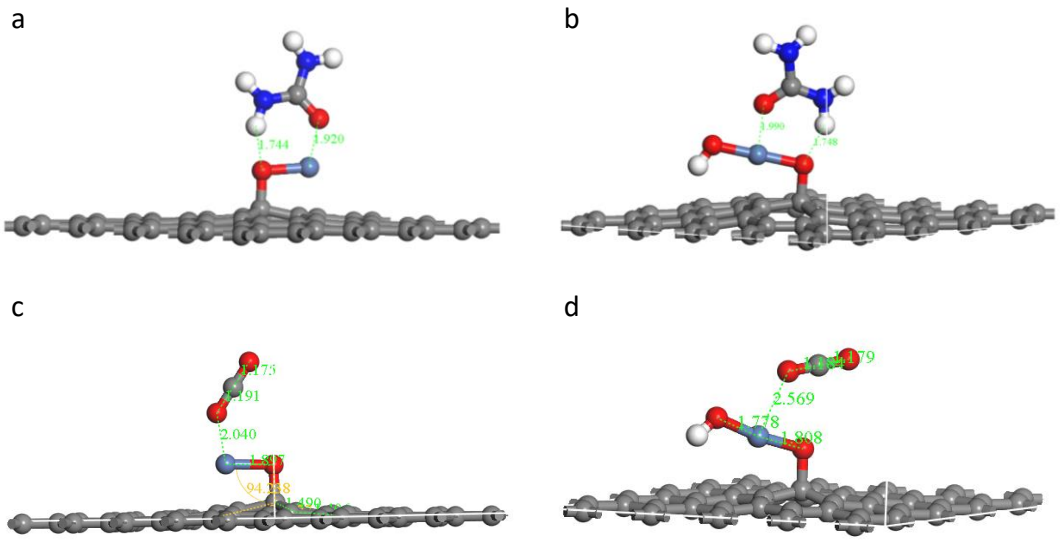

Figure 3.4 The shortest distance between urea and (a) NiO@Graphene, (b) NiOOH@Graphene, and (c) CO_2 and NiO@Graphene, (d) NiOOH@Graphene.

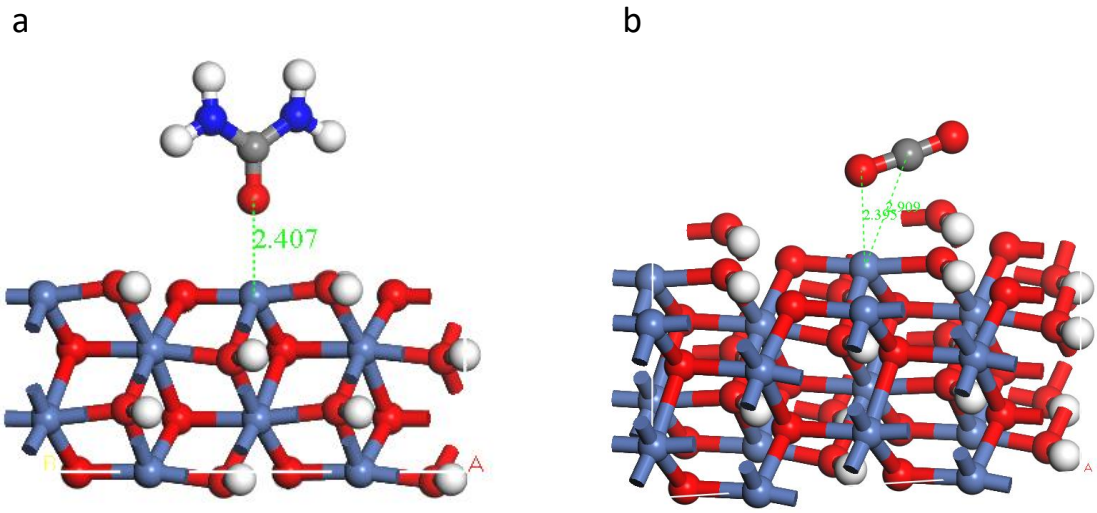

Figure 3.5 The shortest distance between (a) urea, (b) CO_2 and NiOOH.

The electron density difference map is calculated to investigate the electron transfer between the given sample and urea/CO_2 molecules intuitively. It can be observed from Figs. 3.6a-b that electrons transfer from the center Ni atom and the adjacent O atom of urea to the intermediate region between NiO@Graphene or NiOOH@Graphene and urea. There is a significant charge aggregation between Ni and O atoms (Figs. 3.6a-b), suggesting the potential formation of Ni-O covalent bonds. This is due to the charge transfer and redistribution leading to the hybridization of the Ni 3d and O 2p orbitals. Considering the effect of graphene, the control experiments were also carried out under the same condition. Graphene does not have any contributions to urea/CO_2 adsorption (Fig. 3.7).

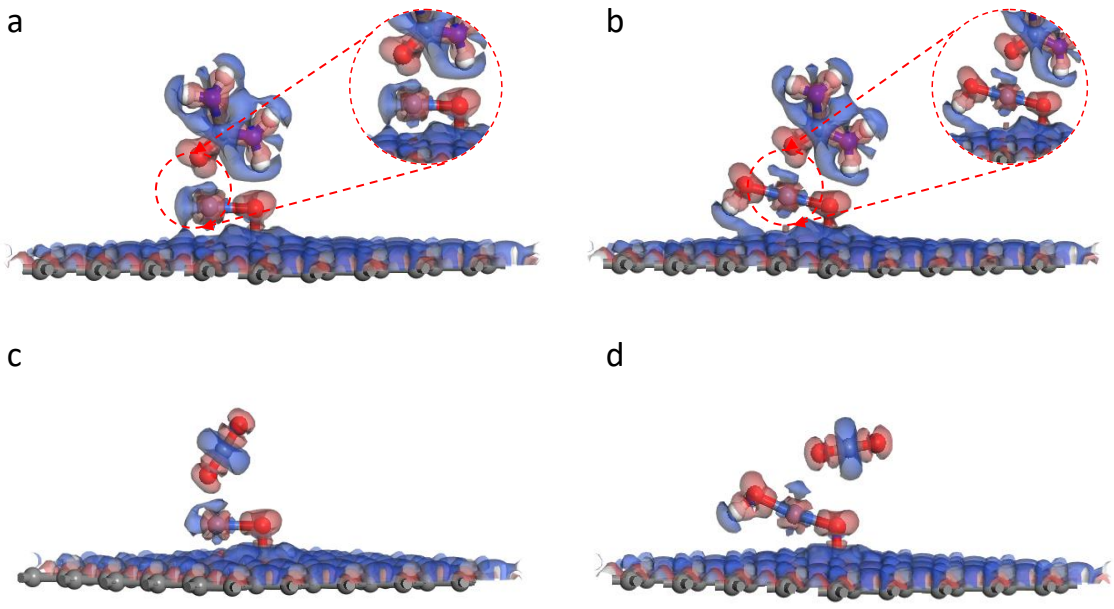

Figure 3.6 The electron density difference of urea molecule adsorbed on (a) NiO@Graphene and (b) NiOOH@Graphene, and CO_2 adsorbed on (c) NiO@Graphene and (d) NiOOH@Graphene. The red hooded face means the enrichment of electrons while the blue means the deficiency of elections.

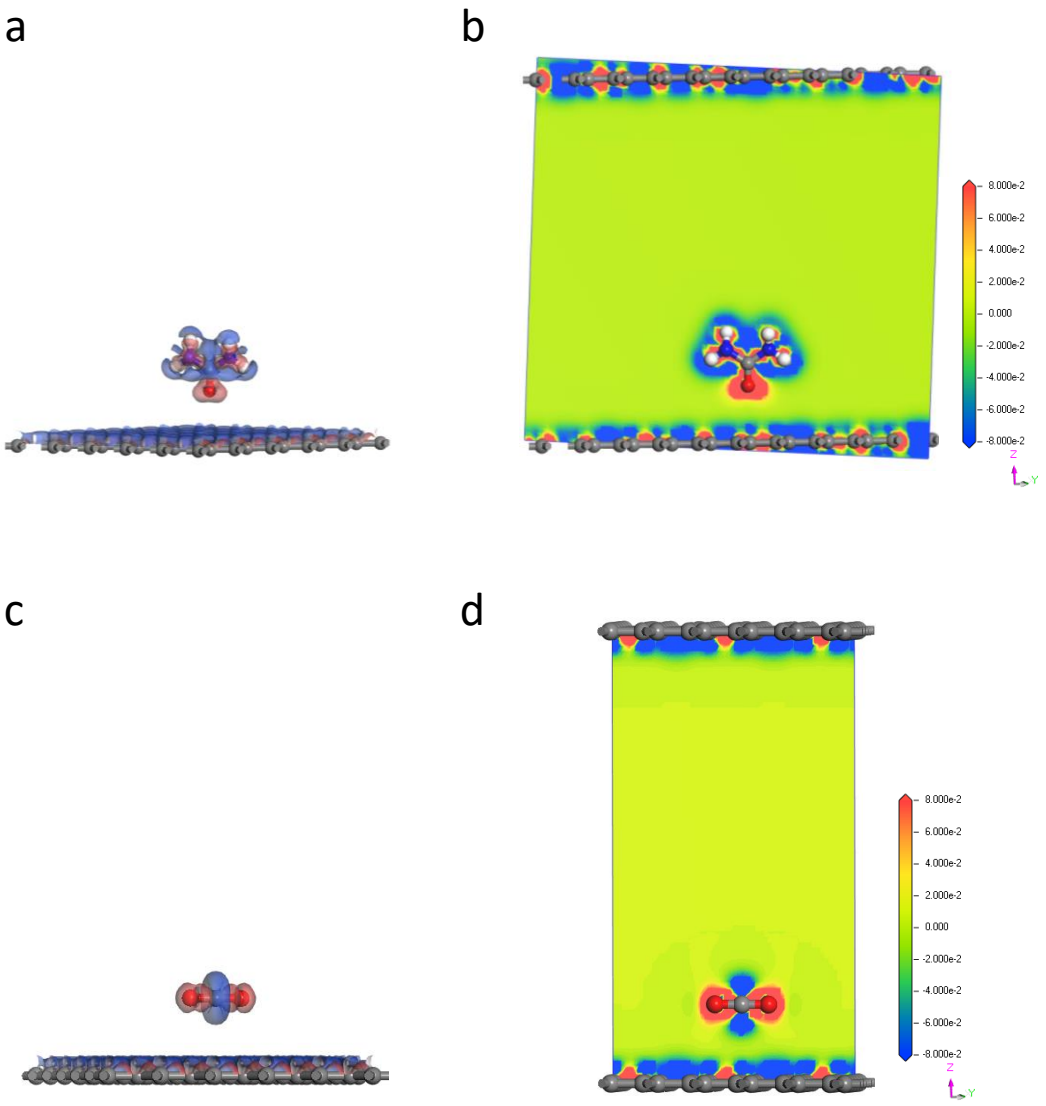

Figure 3.7 (a) The electron density difference of urea molecule adsorbed on the surface of Graphene. (b) Slice image of the adsorption of urea molecule on the surface of Graphene. (c) The electron density difference of CO_2 molecule adsorbed on the surface of Graphene. (b) Slice image of the adsorption of CO_2 molecule on the surface of Graphene. Note: (a, c) The red hooded face means enrichment of electrons while the blue means the deficiency of elections, (b, d) The contour around the atoms represents electron accumulation (red) or electron deletion (blue).

From the viewpoint of electron configuration, Ni(II) species ($[Ar]3d^8$) with two unsaturated d orbitals could be filled by O ($[He]2s^22p^4$) well rather than that of Ni(III) species ($[Ar]3d^7$). Generally, the stronger the hybridization, the stronger the adsorption is toward a urea molecule. NiO@Graphene presents the larger overlapping area of

charge density and with the stronger covalent interaction (Fig. 3.8). As for CO_2 adsorption, the NiO@Graphene composite presents similar adsorption behavior. In the whole electrochemical urea oxidation process, the adsorption/desorption of CO_2 is regarded as the key descriptors for the UOR in an alkaline environment. So, NiOOH@Graphene composite performs better desorption behavior compared to NiO@Graphene (Fig. 3.9).

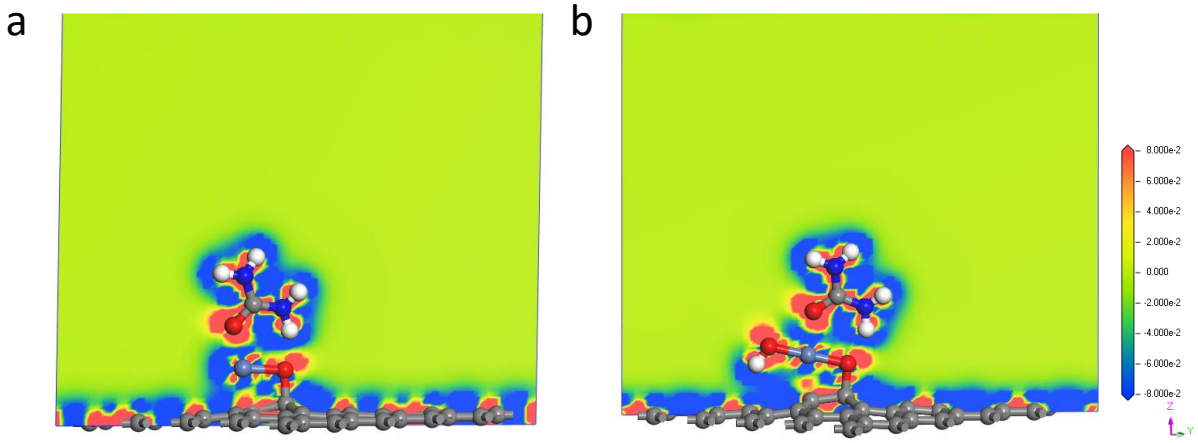

Figure 3.8 Slice images of the adsorption of urea molecule on the surface of (a) NiO@Graphene and (b) NiOOH@Graphene and the corresponding slice of the electron density difference. The contour around the atoms represents electron accumulation (red) or electron deletion (blue).

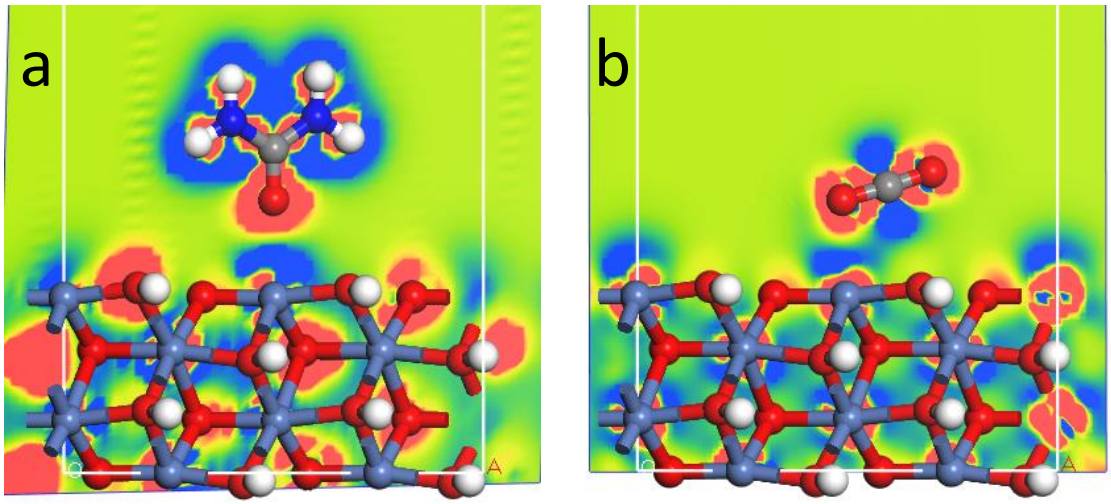

Figure 3.9 Slice images of the adsorption of (a) urea and (b) CO_2 molecule on the surface of NiOOH. The contour around the atoms represents electron accumulation (red) or electron deletion (blue).

To further confirm this conclusion, the slight electron density difference. **Fig. 3.10** shows that a few more electrons from Ni atom to the O atom of urea on the NiOOH@Graphene composite than that on the NiO@Graphene, which indicates that Ni(III) species presented its favorable active sites in the key step of UOR. This is in line with the adsorption energy results that NiO@Graphene composite shows the favorable adsorption toward urea, and NiOOH@Graphene composite shows better CO_2 desorption performance in the key reaction.

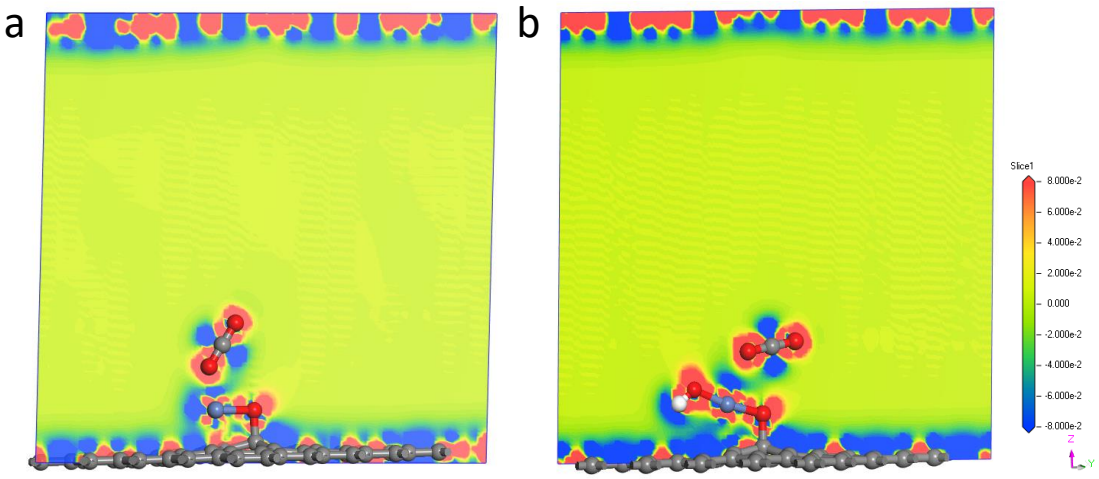

Figure 3.10 Slice images of the adsorption of CO_2 molecule on the surface of (a) NiO@Graphene and (b) NiOOH@Graphene and the corresponding slice of the electron density difference. The contour around the atoms represents electron accumulation (red) or electron deletion (blue).

The above results demonstrate that NiO@Graphene composite can effectively adsorb urea, and then form a Ni-O covalent bond with urea, which is well-related to the adsorption/desorption properties and surface charge density of molecules. After NiOOH@Graphene is formed in the alkaline media, Ni 3d orbitals are bonds to O 2p orbital of urea near the Fermi level, suggesting the charge transfer between Ni and O atoms. Furthermore, based on the DOS (Density of State) diagram in NiO@Graphene and NiOOH@Graphene, the peaks of NiOOH@Graphene become tightened (Fig.

3.11). The peaks of Ni 3d in the NiOOH@Graphene shift to lower energy near the Fermi level than that of NiO@Graphene. The center of Ni 3d orbitals peak moves from -1.61 eV (NiO@Graphene) to -2.42 eV (NiOOH@Graphene). Additionally, more electrons flow from Ni atom to O atom to establish a strong Ni-O bond, resulting in C-O_{ads} with weakened bond energy, and thus facilitating the *COO desorption from urea. Generally, the Fermi level can expose the ability of electron transfer on the electrocatalyst surface. The larger the Fermi level, the higher the electron transfer capability. Compared to the Fermi level of NiO@Graphene (1.61 eV), the much larger Fermi level NiOOH@Graphene (2.42 eV) suggests that the Ni(III) sample can significantly improve the electron transfer ability of NiOOH@Graphene. Besides, the lower d band center leads to weaker adsorption for CO_2. Based on the above DFT analysis, we conclude that the active electron density of NiOOH@Graphene was effectively upshifted in the UOR process.

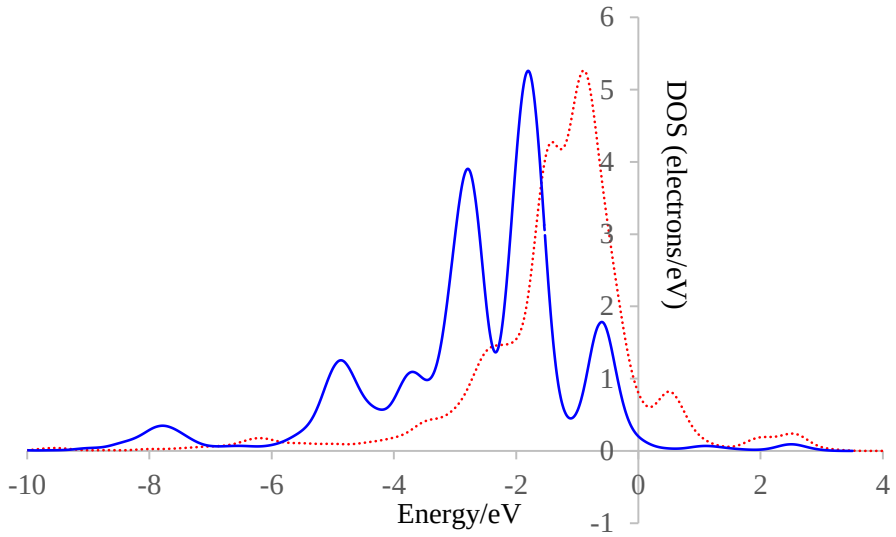

Figure 3.11 The *d* density of states of Ni in NiO (doted red line) and NiOOH (blue line), respectively. The Fermi level is set to zero, and the vertical lines represent the *d* band center.

3.3.3 Comparison of heterojunction model and single-atom model

In our previous work, the heterojunction model based on NiO nanoparticles and graphene was constructed to simplify the theoretical work. The heterojunction structure is a general model to simulate the multi-component composite. DFT calculations with the CASTEP package were employed to reveal the effect of biomass-derived porous carbon on the UOR performance of NiO@C nanocomposite and uncover the Ni(III) species working as active sites for UOR. In this process, NiO@C nanocomposite just played the intermediate role. It turned into NiOOH@C nanocomposite with the assistance of the alkaline media, then Ni(III) species in NiOOH@C acted as active sites for efficient urea oxidation. However, the above model just qualitatively revealed the influence of the porous structure on the electronic structure of NiO nanoparticles and the synergistic effect between NiO nanoparticles and the porous carbon. From the observed SEM and TEM images, it is also applicable for the single-atom model considering the Ni species acting as active sites and the ideal carbon substrate in the UOR. Furthermore, DFT calculations with the Dmol^3 package were used in this study to investigate the role of Ni(III) species in the UOR. A different phenomenon was observed in that NiO@Graphene has the favorable adsorption of urea. It indicates NiO@Graphene turned into NiOOH@Graphene in the alkaline electrolyte first and then urea absorbed on NiO@Graphene.

Based on the above analysis, it can be demonstrated that NiO@Graphene shows favorable adsorption of the hydroxyl group in the first stage, then turned into NiOOH@Graphene under the alkaline condition for efficient urea oxidation. The presence of Ni(III) species and excellent electrical conductivity of NiOOH@Graphene shows better desorption of CO_2. Moreover, benefiting from the excellent conductivity

of graphene, electrons transferred from urea to NiOOH@Graphene through the Ni-O: urea bond easier. Graphene also provides a function for facilitating alkaline electrolyte diffusion, ensuring the formation of Ni(III) species, and promoting mass transfer effectively. Such a composite structure has the above merits to guarantee the stability and efficiency of NiO@Graphene as an efficient UOR electrocatalyst.

3.4 Conclusions

In this work, the single-atom model, NiO nanoparticles was bonded with graphene as NiO@Graphene composite, was constructed for the electrochemical urea oxidation in terms of a theoretical view. DFT calculations showed that NiO nanoparticles dispersed on graphene provide strong adsorption with the hydroxyl group, then NiOOH@Graphene was formed after NiO@Graphene reacted with the hydroxyl group. Compared to NiO@Graphene, NiOOH@Graphene presents higher desorption energy for the CO_2 molecule in the key rate-determining step. Notably, Ni(III) species in the NiOOH@Graphene is the most favorable sites for the urea oxidation reaction. Moreover, NiOOH@Graphene not only guarantees the stability of NiOOH and graphene, but also promotes the electron transfer between NiOOH and graphene. Benefiting from the coupling effect between the Ni(III) species and graphene, the NiO@Graphene can theoretically reach excellent electrocatalytic urea oxidation. These studies provide the theoretical guidance that the NiO@Graphene played the intermediate role in the urea oxidation process before Ni(III) species formed in the alkaline electrolyte. NiOOH@Graphene also facilitates the desorption of CO_2 from the catalyst surface for UOR catalysis. More experimental investigations based on the NiO nanoparticles and graphene will be verified in the followed work.

CHAPTER 4 NICKEL OXIDE IMMOBILIZED ON THE CARBONIZED EGGSHELL MEMBRANE FOR ELECTROCHEMICAL DETECTION OF UREA[4]

4.1 Introduction

Urea ($CO(NH_2)_2$) is the main nitrogen-containing substance from the urine of human activity and mammal animal, which is also an effective and critical indicator in evaluating various metabolic disorders.[17, 91, 92] Urea can decompose naturally to toxic ammonia and nitrates permeating into groundwater, then cause environmental problems and even health issues.[21, 22, 93] Therefore, the detection of urea concentration and decomposition of urea-rich sewage is vitally important in human health and environment industries.[13, 23, 24, 28, 94, 95] The electrochemical urea oxidation reaction (UOR, $CO(NH_2)_2 + 6OH^- \rightarrow N_2 + CO_2 + 5H_2O + 6e^-$) was developed in recent years making urea electrolysis easier, consuming much less energy (0.37 V) compared to the electrochemical process of water splitting (1.23 V) in terms of hydrogen production [11, 17], and also utilizing this reaction for electrochemical sensor for urea.[96-98] Gupta and co-authors reported several electrochemical sensors with metal ions[99-102], uric acid[103], dexamethasone[104], and corticosteroid triamcinolone[105] via voltammetry and amperometry. Electrochemical measurements are regarded as favorable for quantitative analysis due to their fast response and high sensitivity.[99, 106-114]

---

[4] Chapter 4, in full, is a reprint of the research paper titled 'Nickel oxide immobilized on the carbonized eggshell membrane for electrochemical detection of urea' as it published on the journal of ***Journal of The Electrochemical Society***. Shun Lu, Zhengrong Gu, Matthew Hummel, Yue Zhou, Keliang Wang, Ben Bin Xu, Yucheng Wang, Yifan Li, Xueqiang Qi, Xiaoteng Liu. 167.10 (2020): 106509. Shun Lu was the primary investigator and first author of this article.

Eggshell membrane (ESM), is derived from the eggshells of industrial egg processors and regarded as biowaste.[115] ESM is mainly comprised of proteins which form interwoven fibrous structures that has a strong adsorption capacity to bind and confine metal ions.[116] Besides, it also can keep a stable structure in aqueous and alcoholic media and undergo pyrolysis.[117] Interestingly, these biowaste ESM used as a support could effectively immobilize and disperse nanoparticles and is the reason for the unique three dimensional (3D) porous network with plenty of functional groups such as amines, amides and carboxylic surface functional groups and the resulting nanocomposites have been reported to display enhanced catalysis and sensing activity such as $CoFe_2O_4$@C[118], NiO-Ni@C[119], FeS@C[120] and Au network[121], etc.[52, 54] The unique network structure of ESM composed of biomacromolecular fibers provides a novel template for the functional groups, with superior porosity and specific surface area, which can offer multiple transport pathways for both electrons and ions.

In this work, ESM was utilized here as a bio-template for the rational design of the electrode material. Furthermore, nickel ions can be absorbed on its surface to form the precursor ($Ni(OH)_2$/ESM). Consequently, we reported an integrated 3D network composed of NiO nanoparticles anchoring on the carbonized ESM using a mixed method of hydrothermal and pyrolysis. The NiO nanoparticles anchored 3D carbonized network of the catalyst provides more catalytic active sites and enables easy access of reactants to the catalyst surfaces. Experimental results confirmed the synergetic effect between NiO nanoparticles and the *c*-ESM with higher exposed active sites and faster electron transport, ensuring superior performance of urea detection. It is worth mentioning that the biowaste ESM can be converted into a useful support for the as-

prepared sensor. This work also sheds light on the potential for further applications in "trash to treasure".

4.2 Experimental

4.2.1 Chemical and reagents

All reagents were of analytical reagent grade, purchased from Fisher Scientific Co LLC and Alfa Aesar Chemical Reagent Co, Ltd., and used as received without further purification. Fresh eggs were bought from the local market.

4.2.2 Preparation of c-ESM

The eggshell membrane was processed first by removing the eggshell, then rinsed with large amounts of de-ionized water (DIW, 18.4 MΩ cm^{-1}, Milli-Q) to remove excess yolk and egg white and dried at room temperature, followed by calcination at 500 °C for 2 h under a heating rate of 10 °C/min in a N_2 atmosphere. The carbonized ESM (named as *c*-ESM) was collected after washing with DIW and drying at room temperature.

4.2.3 Synthesis of 3D NiO/C nanocomposites

Briefly, 3D NiO/C nanocomposites were fabricated through a simple two-step method, as illustrated in Fig. 4.1. (i) eggshell with a top hole was rinsed with large amounts of DIW in order to obtain a clean container, then 0.1 M $Ni(NO_3)_2$ solution was transferred

into a cleaned eggshell, and 20 mL urea solution was added into a beaker. (ii) eggshell with nickel nitrate aqueous was immersed into urea solution in a beaker and maintained at 70 ℃ for 6 h. In this process, a large amount of Ni^{2+} ions were absorbed on the microporous network of ESM, and hydroxyl (OH^-) ions produced from the urea while heating. (iii) the reaction system was cooled to room temperature naturally, and the $Ni(OH)_2$/ESM precursor was peeled from eggshell reactor. The stripped precursor was rinsed thoroughly with DIW. (iv) $Ni(OH)_2$/ESM was calcined at 500 ℃ for 2 h in the protection of N_2, the final product (NiO/c-ESM) was then cooled to room temperature with N_2 protection. The resulting black powder of 3D NiO/c-ESM nanocomposites was collected for further use. Pure NiO particles were synthesized with the same procedure except for the absence of ESM for comparison.

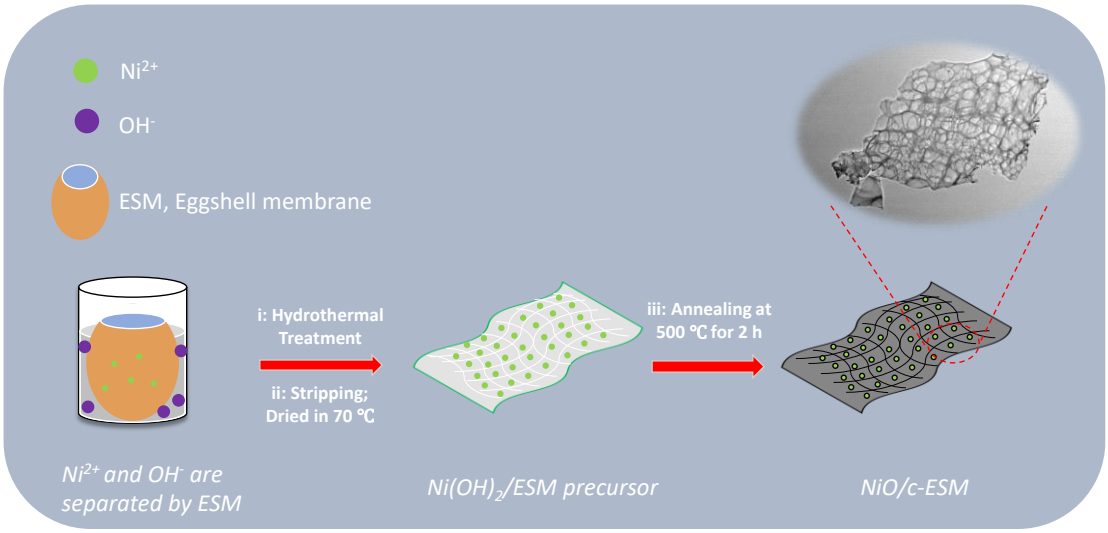

Figure 4.1 Illustration of synthesis procedure of NiO/*c*-ESM

4.2.4 Physical characterization.

Structural information of the samples was carried out with X-ray diffraction (XRD, Rigaku, λ= 1.5418 Å). The scanning electron microscopy (SEM, Hitachi S-3400N) was

used to observe the surface morphologies of the as-prepared samples. Transmission electron microscopy (TEM, JEOL JEM-2100F) and high-resolution transmission electron microscope (HRTEM) were operated under an accelerating voltage of 200 kV. STEM-EDS (Oxford) was used for confirming the possible elements of the as-prepared sample.

4.2.5 Electrochemical characterizations.

All electrochemical tests were carried out on an electrochemical workstation (CHI 760E, Austin, Texas) with a typical three-electrode system. A catalyst-modified glassy carbon electrode (3 mm in diameter), Pt foil, and Ag/AgCl with saturated KCl solution were selected as the working electrode, counter electrode, and reference electrode, respectively. The details of electrode preparation and electrochemical setup were set up according to previously reported work. The loading mass of the as-prepared catalyst (4 μL, 1.33 mg mL^{-1}) on the electrode surface is *ca.* 0.075 mg cm^{-2}. All electrochemical tests were also performed with the same setting as previously reported[112]. Square wave voltammetry (SWV) was chosen as the primary technique for detection. Here, all tests were performed at 25 ℃ and all potentials were converted versus a reversible hydrogen electrode (RHE) based on the Nernst equation: ($E_{RHE} = E_{Ag/AgCl} + 0.059 \times pH + 0.21$ V, 25℃) unless otherwise specified.

4.3 Results and discussion

3D NiO/*c*-ESM nanocomposites were prepared through a simple two-step method, as schematically demonstrated in Fig. 4.1. The mechanism for preparation of NiO/*c*-ESM nanocomposites can be expressed as follows (Equation.1-4):

$$CO(NH_2)_2 + H_2O \rightarrow CO_2 + NH_3 \qquad \text{Equation. 1}$$

$$NH_3 + H_2O \rightarrow NH_4^+ + OH^- \qquad \text{Equation. 2}$$

$$Ni^{2+} + 2OH^- + ESM \rightarrow Ni(OH)_2/ESM \qquad \text{Equation. 3}$$

$$Ni(OH)_{2_{ESM}} \xrightarrow{carbonization} NiO_{c-ESM} + H_2O \qquad \text{Equation. 4}$$

X-ray diffraction has been applied to study the structural information of the as-prepared samples. Fig. 4.2a reveals that the XRD pattern of NiO/*c*-ESM nanocomposites. A series of typical diffraction peaks (2θ: 37.2°, 43.2°, 62.8°) corresponding to (111), (200) and (220) crystal planes, indicating the formation of pure nickel oxide (JCPDS No.47-1049). Furthermore, the broad peak at 2θ of 24.8° corresponds to an experimental *d* spacing of 3.37 Å indicating presence of graphite-like carbon (JCPDS No. 41-1487). Fig. 4.2b presents that the SEM image of NiO/*c*-ESM nanocomposites with an obvious network-like morphology. TEM images (Fig. 4.2c-d) further confirmed the *c*-ESM and NiO/*c*-ESM with the crosslink-like morphological feature and its pore lateral size of ~200 nm, while the transparent characteristic of the *c*-ESM indicates its ultrathin thickness. In the Fig. 4.2e, NiO nanoparticles (size: ~15 nm in diameter) were anchored on the surface of c-ESM with high and even dispersion identified by TEM observation, their morphology appears good dispersion. Fig. 4.2f presents the nitrogen adsorption/desorption isotherm and pore size distribution of NiO/*c*-ESM

nanocomposites. The BET specific surface areas of NiO/*c*-ESM was found to be 79.6 $m^2 g^{-1}$. The isotherms resemble the type IV classification. The hysteresis loop starts at the relative pressure (P/P_0) of about 0.45 and extends almost to 1, indicating that NiO nanoparticles are mesoporous, which is associated with the c-ESM with the filling of the mesopores. The inset of Fig. 4.2f also confirmed NiO nanoparticles with the average diameter of ~15 nm, are consistent with TEM observation.

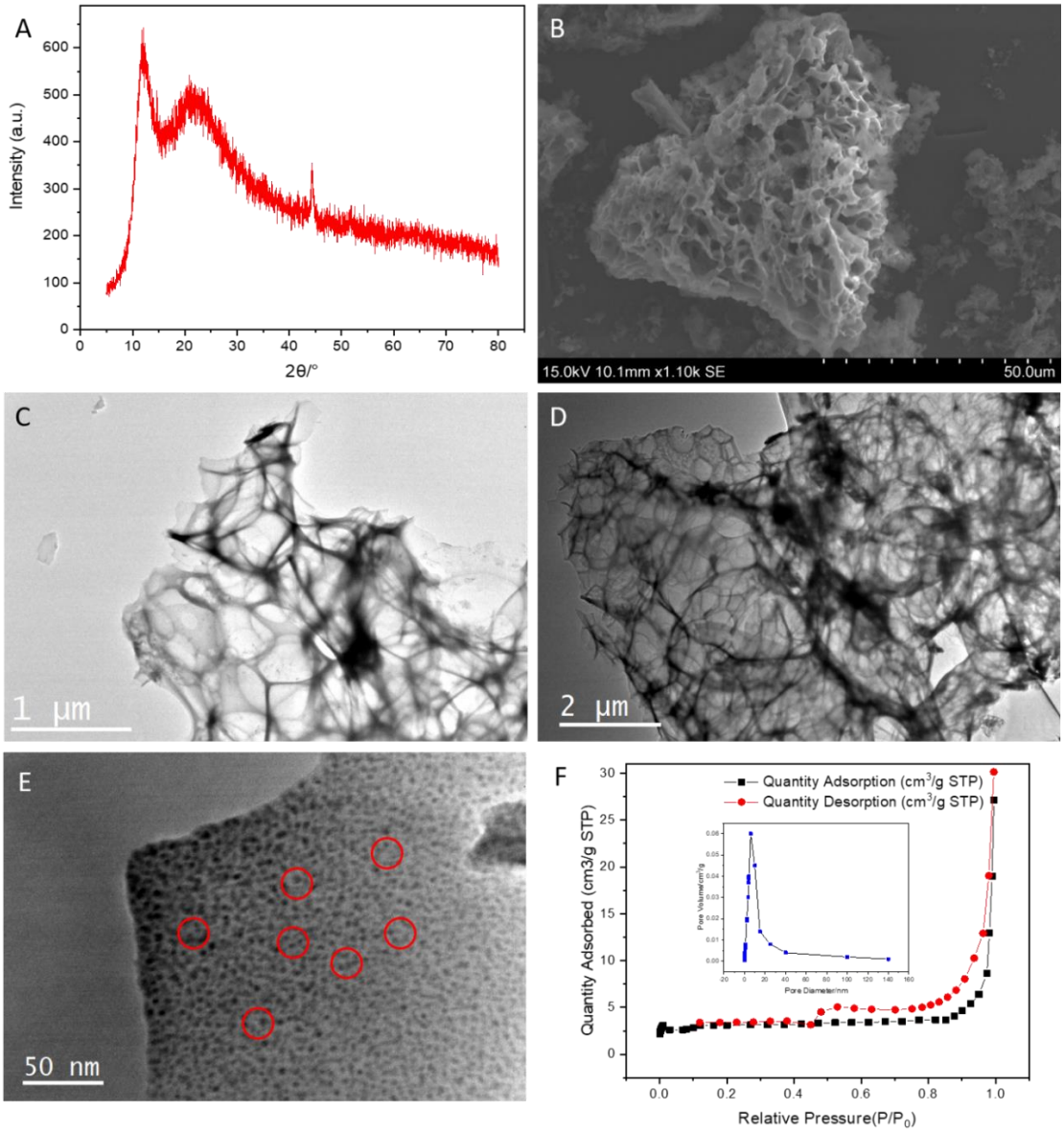

Figure 4.2 (a) XRD pattern and (b) SEM image of NiO/c-ESM, TEM image of (c) c-ESM and (d) NiO/c-ESM, (e) selected area TEM from (d), (f) BET analysis of NiO/c-ESM, inset: pore size distribution of NiO/c-ESM corresponding to (f).

To further verify the surface topology of the 3D NiO/*c*-ESM nanocomposites, the elemental composition is illustrated by using scanning transmission electron microscopy-energy dispersive X-ray spectroscopy (STEM-EDX) mapping. Fig. 4.3 presents EDX results of the 3D NiO/*c*-ESM nanocomposites, they prove that the as-prepared nanocomposite is mainly composed of Ni, O and C (here, the existence of Ca, Cr, and Cu is caused by the Cu mesh), and STEM-EDS mapping in Fig. 4.3c indicates that these elements are dispersed uniformly. Based on the above observation (Fig. 4.1-4.2), it can be proposed that nickel ions are adsorbed on the inner surface of ESM during the preparation of NiO/*c*-ESM nanocomposites and, hydroxyl ions released from urea reacted with the adsorbed nickel ions. This kind of hybrid precursor kept the network-like structure synergistically stable and prevents the shrinkage caused by thermal annealing.[119, 122] Therefore, the surface of NiO/*c*-ESM nanocomposites become an obvious network-like morphology with plenty of porous structure.

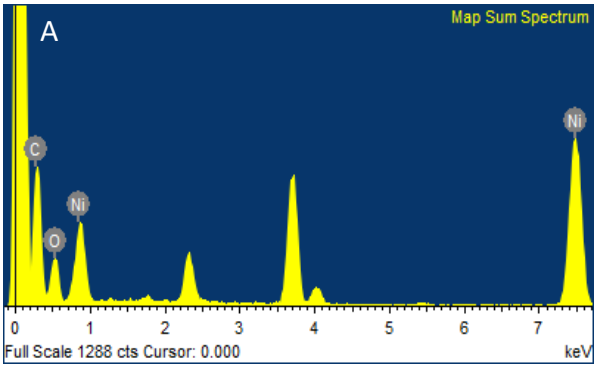

B

Element	Weight%	Atomic%
C K	0.30	1.48
O K	0.11	0.42
Ca K	0.16	0.24
Cr K	0.45	0.51
Ni K	68.13	68.64
Cu K	30.85	28.71
Totals	100.00	

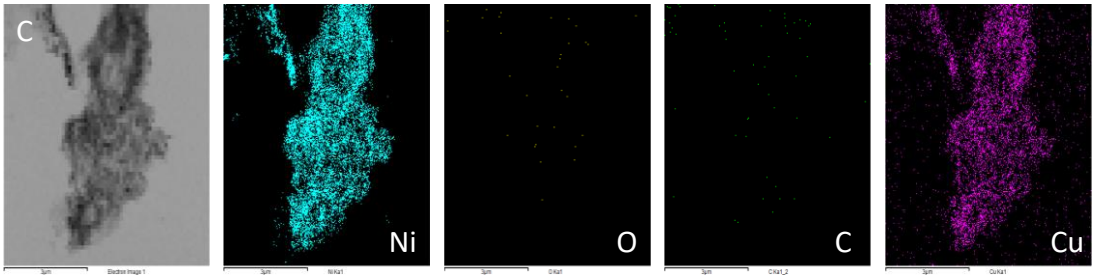

Figure 4.3 (a) EDX spectra, (b) element contents and (c) STEM-EDX mapping images of NiO/c-ESM.

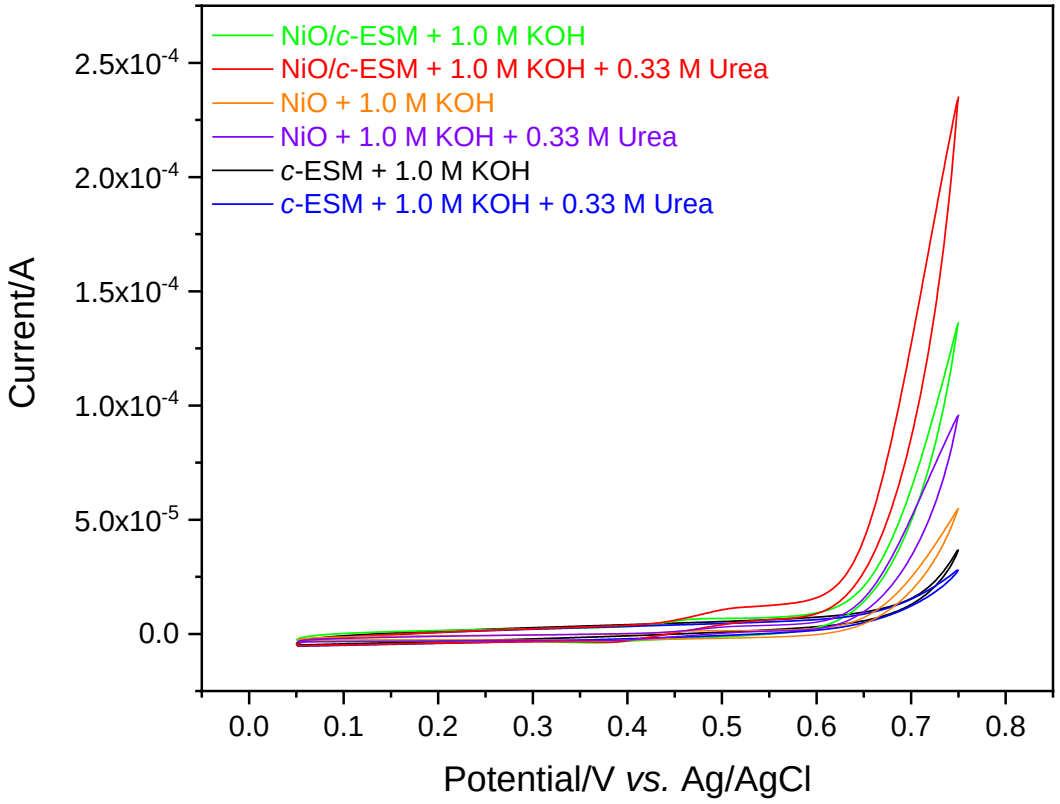

Figure 4.4 Cyclic voltammograms of NiO/c-ESM, NiO and c-ESM electrodes in the presence and absence of urea in 1.0 M KOH solution.

The electrocatalytic performance of NiO/*c*-ESM toward urea is evaluated by CV employing a typical three-electrode testing system. Fig. 4.4 displays CVs of NiO/*c*-ESM in 1.0 M KOH solution in the absence and presence of 0.33 M urea, *c*-ESM was also tested for comparison. It has seen that after the addition of 0.33 M urea, there was almost no change for *c*-ESM in terms of current density. In sharp contrast, NiO/*c*-ESM has an obvious increase in oxidation peak current response due to the oxidation of Ni(II) to Ni(III) in the presence of OH^- ions for NiO nanoparticles anchored on the *c*-ESM.[13] The electrochemical kinetics of urea oxidation reaction was investigated in 1.0 M KOH solution containing 10 mM urea. (Fig. 4.5a). The relationship of peak current (I_p) and scan rate is investigated and compared (Fig. 4.5b-c). The peak current (I_p) plots were

linearly proportional to the square root of the scan rate with a higher correlation coefficients (R^2) of 0.998, suggesting a diffusion-controlled process (Fig. 4.5c).

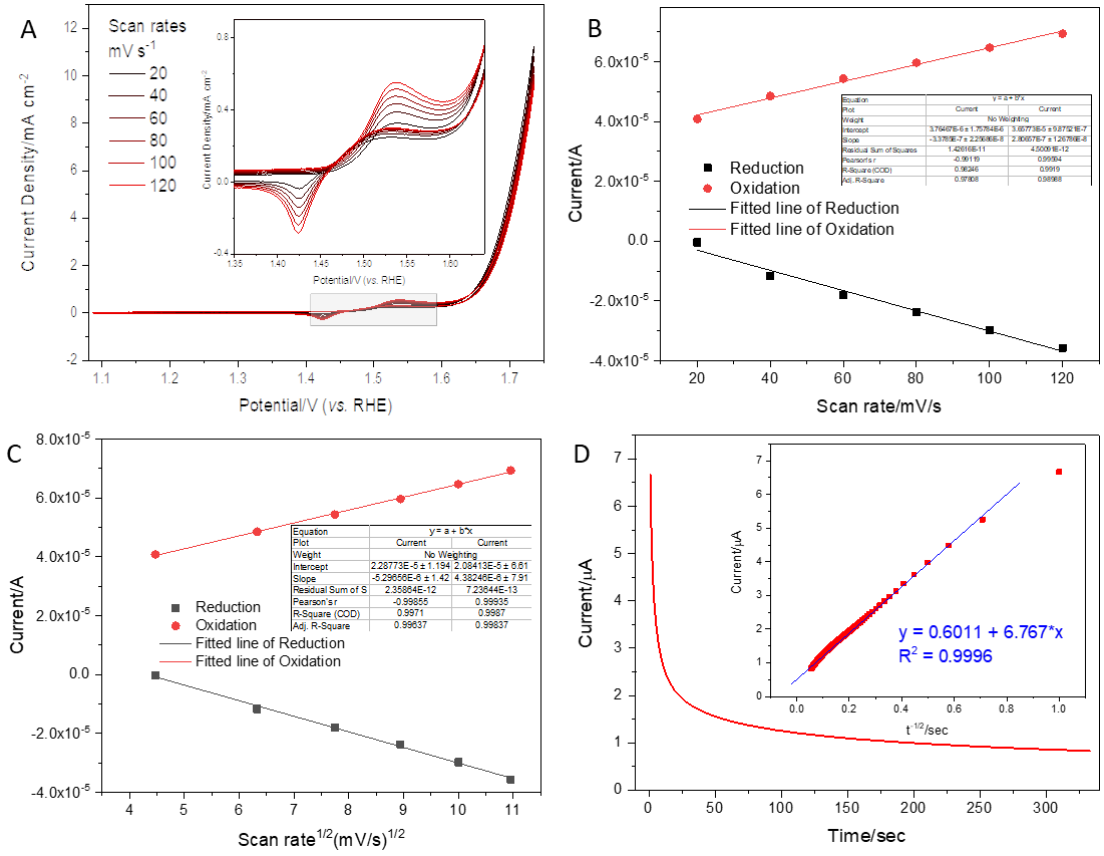

Figure 4.5 (a) Cyclic voltammograms of NiO/c-ESM in the presence of 10 mM urea in 1.0 M KOH at different scan rate (20-120 mV s^{-1}). Comparison of calibration plot of peak current vs. function of scan rate: (b) calibration plot of peak current vs. scan rate, (c) calibration plot of peak current vs. square root of scan rate. (d) Amperometric response of NiO/c-ESM in 1.0 M KOH with 2.0 mM of urea at potential of 1.45 V (vs. RHE), (inset) the plot of I vs. $t^{-1/2}$ derived from the amperometric curve.

Furthermore, the double layer capacitance (C_{dl}) has been studied to measure the electrochemical active surface area (EASA) of NiO/*c*-ESM and *c*-ESM modified electrodes (Fig. 4.6a) by CV technique in a narrow potential range (0.06-0.16 V, nonfaradaic zone) with a series of scan rates.[54, 123-125] After calculation, the EASA of NiO/*c*-ESM electrode is ~70.1 cm^2 higher than NiO electrode (50.3 cm^2) and *c*-ESM

electrode (66.8 cm^2), suggesting that the effective active sites of NiO/*c*-ESM for urea oxidation is higher than that of *c*-ESM.[126]

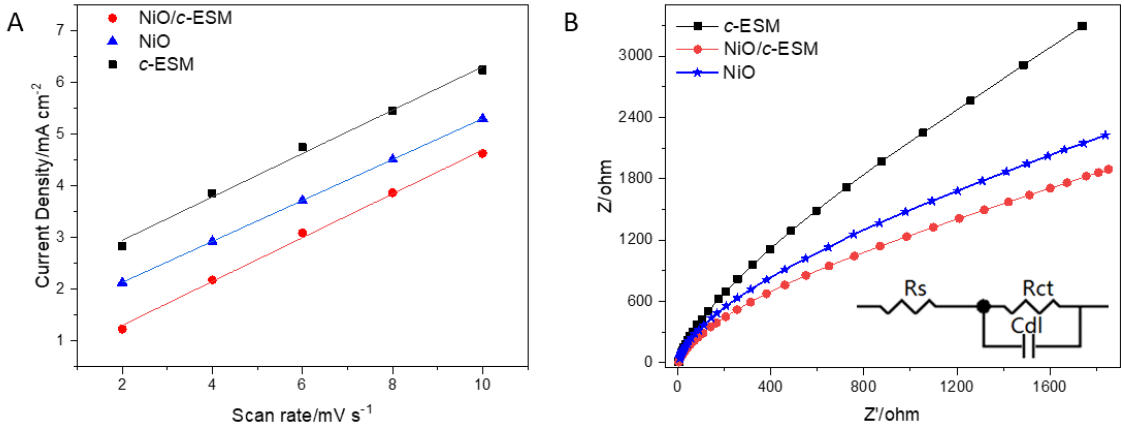

Figure 4.6 (a) The double layer capacitance of NiO/c-ESM, NiO and c-ESM electrode in a narrow potential range in 1.0 M KOH at different scan rates (2-10 mV s^{-1}). (b) Nyquist plots of NiO/c-ESM, NiO and c-ESM electrode in 1.0 M KOH.

Electrochemical impedance spectroscopy (EIS) can be used to analysis the electron transfer process and impedance changes on the surface of the working electrode. Fig. 4.6b displays Nyquist plots of NiO/*c*-ESM and *c*-ESM under a loading potential of 1.45 V. The semicircular diameter of NiO/*c*-ESM (R_{ct}, 4.8 Ω) is smaller than that of NiO (R_{ct}, 8.2 Ω) and *c*-ESM (R_{ct}, 6.4 Ω), revealing that NiO/*c*-ESM has a better charge transfer during urea oxidation. Combined EASA calculation and EIS analysis, it demonstrated that NiO/*c*-ESM could be a potential electrode material for urea determination.

Square wave voltammetry (SWV) measurement was employed to record the response of the NiO/*c*-ESM electrode with a series of urea concentrations. NiO(II) nanoparticles were oxidized to NiOOH(III) during the electrochemical process, then catalyzes the decomposition of urea. The functional Ni(III) which worked as an active species, is

simultaneously oxidized in the process. Benefiting from efficient electron transfer and reversible properties of the NiO nanoparticles and the porous *c*-ESM. The electrons generated from Ni(III)/Ni(II) redox are transferred to the surface of electrode. The NiO/*c*-ESM electrode presents a sensitivity of 0.462 μA mM^{-1} cm^{-2} in the inset of Fig. 4.7. The results show that the limit of detection (LOD) is calculated to be ~20 μM from the SWV curves with the linear range from 0.05 to 2.5 mM with a correlation coefficient of 0.988 (3σ). This electrochemical sensor could achieve urea detection within 7 s (single sample).

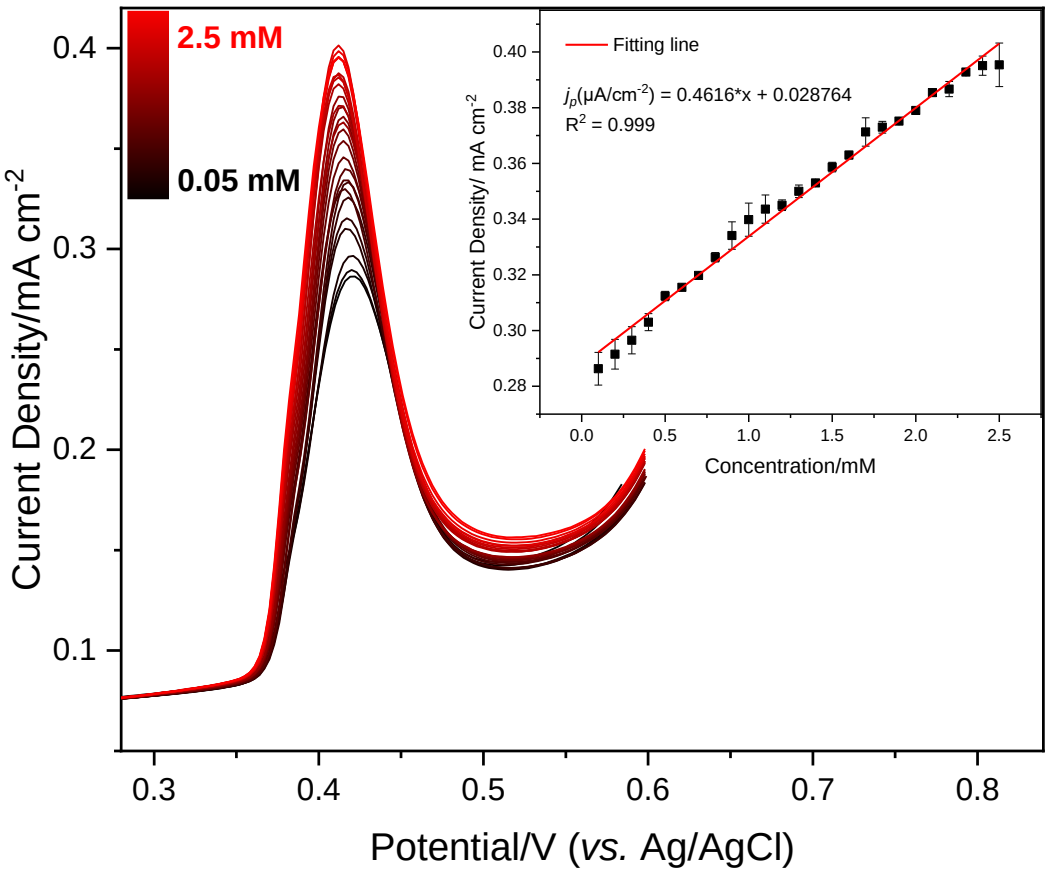

Figure 4.7 SWV curves of NiO/c-ESM to detect urea, inset: calibration curve of current density vs. urea concentration.

Table 4.1 compares the data from the as-proposed sensor and other electrochemical sensors based on the urea determination, the as-proposed sensor exhibits lower LOD and superior sensitivity. The electrocatalytic activity and sensitivity toward urea for NiO/*c*-ESM could be attributed to the 3D network of *c*-ESM and NiO nanoparticles configuration of this electrode while exposes more active sites facilitating sufficient transport of reactants and products.

Table 4.1 Sensing performance of the NiO/*c*-ESM electrode and recently reported electrochemical sensors towards urea

Electrode	Substrate	Linear range /mM	Sensitivity /μA mM^{-1} cm^{-2}	LOD/ μM	References
Ur-NiO	ITO[a]	0.99-11.50	22.39	N/A	[127]
MWCNT[b]	Silica	0.002-1.07	2.3	N/A	[128]
$NiCo_2O_4$/Graphene	ITO	0.06-0.30	166	5	[24]
Rh/Ur[c]	Platinum	0.1-1.75	1.85	50	[96]
NiO/Ur	ITO	0.83-16.65	21.3	830	[129]
MSA-QDs[d]	Optical method	0.01-120	N/A	10	[130]
NiO/*c*-ESM	Glassy carbon	0.05-2.5	0.462	~20	This work

a: Indium tin oxide; b: Multi-wall carbon nanotube; c: Urease; d: Quantum dots.

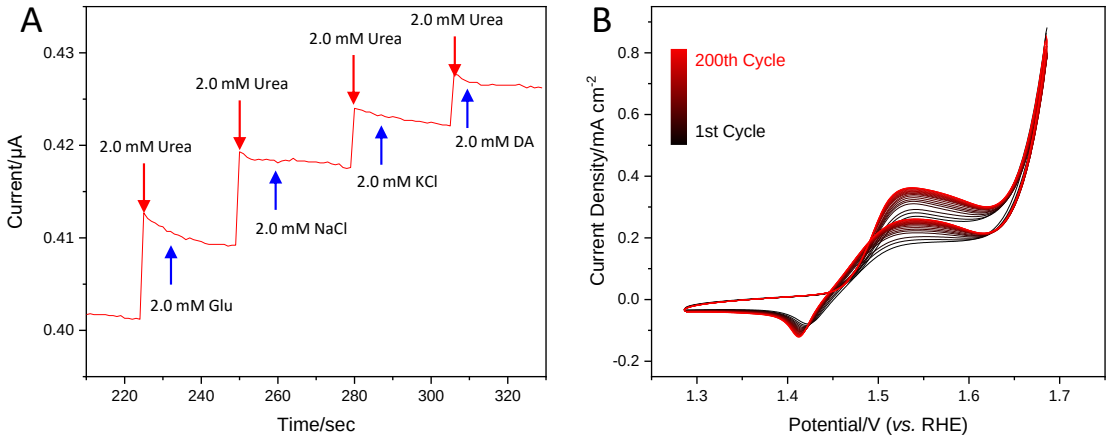

Figure 4.8 (a) The current responses to the addition of urea and different interfering species: 2.0 mM glucose, 2.0 mM Na^+, 2.0 mM K^+, 4.0 mM Cl^- and 2.0 mM uric acid. (d) Cycling stability tests of NiO/c-ESM in 1.0 M KOH with 0.33 M urea at a scan rate of 50 mV s^{-1}.

Selectivity and anti-interfering are another major index in evaluating the performance of electrochemical sensor. As displays in Fig. 4.8a, the current responses to different interfering species, such as Glucose (Glu), Na^+ ions, K^+ ions, and uric acid (UA) and the addition of urea was recorded. Those interfering species have similar electroactive behaviours that are easy to be oxidized, so their influences are non-negligible. It can be found that the stair-like current response towards urea of the as-proposed electrode develops when successive amount of urea, whereas no obvious responses to the other interfering species are obtained, suggesting good selectivity of the electrochemical urea sensor in a diluted urea sample. The stability of NiO/*c*-ESM electrode was also examined. The parameters of the CV tests could remain constant over 200 continuous CV scans through a potential window of 1.3 to 1.7 V in 1.0 M KOH (scan rate: 50 mV s^{-1}). Fig. 4.8b indicates that the current assigned to urea oxidation is 76.4% of the initial value after 200 CV scans, thus suggesting good stability due to the stable structure between NiO nanoparticles and *c*-ESM.

To evaluate the application of the NiO/*c*-ESM electrode, urea detection in real samples were examined. 10 µL tap water sample was spiked with 1.0 M KOH to obtain the test water sample, as shown in Table 4.2. The obtained recovery values for the determination of urea are between 92.8 and 105.2% for the test water samples. The relative standard deviation (RSD) value of <5% was obtained for three measurements of different spiked samples. Given the experimental results, this means the as-prepared NiO/*c*-ESM electrode has good selectivity toward urea determination.

Table 4.2 Determination of urea in alkaline buffer and tap water samples

Samples	Urea added /mM	Total found /mM (n = 3)	RSD% (n = 3)	Recoveries %
KOH buffer	0.01	0.0098	1.83	98
	1.0	1.021	1.92	102.1
	2.0	1.994	2.06	99.7
Tap water	0.01	0.0096	3.20	96
	1.0	0.928	1.76	92.8
	2.0	2.103	2.41	105.2

4.4 Conclusions

3D NiO/*c*-ESM nanocomposites were experimentally prepared by a simple two-step method and employed as an electrocatalyst for urea detection. ESM as biowaste was used as precursor in the synthesis. *c*-ESM with the large surface area provided a possible place for anchoring of the NiO nanoparticles uniformly. NiO/*c*-ESM modified electrode exhibits wider linear range (0.05 to 2.5 mM), and a low detection limit of ~20 µM (signal noise ratio is 3). Besides, the as-prepared electrochemical sensor presented

good selectivity and satisfactory results in real sample application. In this study, 3D NiO/*c*-ESM nanocomposite electrode exhibited good performance and robust durability towards urea detection that is attributed to the synergistic effect of more active sites from NiO nanoparticles and the carbonized porous eggshell membrane.

CHAPTER 5 TRASH TO TREASURE: A NOVEL CHEMICAL ROUTE TO SYNTHESIS OF NIO/C FOR HYDROGEN PRODUCTION[5]

5.1 Introduction

Hydrogen (H_2) with high gravimetric energy density and environmental friendliness, has made H_2 as an ideal energy carrier alternative to the diminishing fossil fuels [131-133]. Hydrogen evolution reaction (HER) from electrolysis of alkaline water is generally regarded as a more promising approach due to alkaline water splitting is more practical for industry than the traditional steam-reforming route ($CH_4 + H_2O \rightarrow H_2 + CO$), which suffers from expensive cost and low purity [134, 135]. Generally, multiple elemental reactions result in the accumulation of energy barriers and further decrease in the electrochemical kinetics of the key half reaction of HER during alkaline water splitting. In addition, HER process in alkaline, the so-called Volmer step, the water dissociation, is identified as the rate-determining step (RDS). However, its sluggish reaction kinetics and hinders the overall HER process. To date, Pt-based materials are still the benchmark electrocatalysts for HER both in acidic and alkaline medium [136-138]. However, their scarcity and high cost are major drawbacks in their large-scale commercialization. Therefore, it is mandatory to develop a cost-effective, non-noble HER electrocatalyst in alkaline environment with better performance [139, 140].

---

[5] Chapter 5, in full, is a reprint of the research paper titled 'Trash to treasure: A novel chemical route to synthesis of NiO/C for hydrogen production' as it published on the journal of ***International Journal of Hydrogen Energy***. Shun Lu, Matthew Hummel, Zhengrong Gu, Yan Gu, Zhisheng Cen, Lin Wei, Yue Zhou, Caizhi Zhang, Chi Yang. 44.31 (2019): 16144-16153.. Shun Lu was the primary investigator and first author of this article.

In recent years, transition metal oxides (TMOs), especially nickel oxide (NiO), have shown high electrocatalytic activity towards HER application [134, 140]. NiO, an important p-type semi-conductive transition metal oxide, has attracted widespread interest as an electrode material in various applications [141], such as supercapacitors [142], Li-ion batteries [143] and fuel cell electrodes [144], due to its high theoretical capacity (2584 F g^{-1}) and cost-effectiveness [142]. Most of the transition metal oxides, could be used as HER electrocatalysts [145]. However, the application of NiO as HER catalyst has been hindered due to its large onset potential, which results from its internal weakness, (I) electric conductivity and (II) accessible surface area. Many efforts have been tried to solve these issues, for instance, Yu et al. [142]prepared a hierarchical flower-like NiO/NCHS composite (NCHS means N-doped carbon hollow spheres) for supercapacitors. This strategy not only provides a conductive matrix with fast electron/ion transportation, but also increases the electrochemical active surface area for the as-prepared supercapacitor. Chinnappan et al. [146]fabricated C@NiO/Ni nanofibers via a simple electrospinning approach and examined their HER performance. Yang et al. [147]prepared NiO/C nanofibers composites derived from metal-organic framework compound as electrode materials for supercapacitors. We can easily found that metal foam and carbon materials are often used as common conductive matrixes, which could improve the conductivity as well as increase the structural stability in the electrochemical fields [140, 142]. Synergistic effect also is an important strategy to improve HER performance of composites. For example, Yu et al. [148]reported that Ni/NiO nanohybrids anchored on $CoSe_2$ nanobelts or carbon nanotube (CNT) sidewalls have shown superior HER performances as a result of the synergistic effect between metallic nickel and NiO. According to the above examples,

it has been observed that NiO has excellent performance as an electrocatalyst and is considered one of the most promising candidates in several experimental conditions.

The disposal of eggshell waste has also attracted much attention due to its environmentally and economically challenging problems [149-152]. ‘Trash to Treasure’ also becomes an interesting and important topic for those wastes, especially for eggshell and eggshell membrane (ESM) [152-154]. Deng et al. [152]demonstrated a novel application of waste eggshell as a multifunctional reaction system for the preparation of Co_9S_8 nanorod arrays on carbon fibers and put forward a new strategy of making use of eggshell to achieve in situ carbonization and sulfurization. Besides, numerous NiO/ESM-based materials with novel structures have been investigated and reported in the literature, such as NiO-Ni nanowires on a carbonized eggshell membrane (Li-ion batteries) [155], porous C@$CoFe_2O_4$ nanocomposites derived from eggshell membrane (microwave absorption) [118], and SnO_2@ESM(energy storage) [156]. It has been observed that eggshell membrane plays a vital important roles in energy storage and conversion according to the above examples [157, 158]. Additionally, it is important that more active sites are easily found to absorb, activate and convert reactants at the interfaces [159]. However, few HER investigations of NiO/C composite derived from $Ni(OH)_2$/ESM have been reported in the literature.

In the present work, the eggshell membrane was selected as the carbon source for the construction of NiO/C nanocomposite to achieve integrated use of eggshell waste as a micro-reactor and the use of eggshell membrane as a functional bio-template. This kind of structure not only enhances the conductivity of composites, but also can provide robust support for functional group. Herein, NiO/C nanocomposites were prepared via a facile and green approach. $Ni(OH)_2$/ESM was obtained through self-assembly of

$Ni(OH)_2$ grown on the ESM surface in an alkaline solution (urea + $H_2O \rightarrow CO_2 + 2NH_3$). Subsequently, the NiO/C nanocomposite was successfully constructed with large surface area after carbonization under N_2 atmosphere. To the best of our knowledge, there is no article on the electrocatalyst for HER application of NiO/C nanocomposites prepared using an eggshell membrane. The as-prepared NiO/C nanocomposite as HER electrocatalyst exhibited better performance than pure NiO particles and carbonization of ESM. The novel design outlined in this paper provides new utility for eggshell waste while also creating in situ functional nanocomposites.

5.2 Experimental

5.2.1 Materials

Nickel (II) nitrate hexahydrate [$Ni(NO_3)_2\ 6H_2O$] and urea (CH_4N_2O) were purchased from ACROS organics™. Nafion (5%) was obtained from Alfa Aesar Co., Ltd. Commercial activated carbon was gotten from Fisher Scientific Co., Ltd. Eggshell waste both eggshell and eggshell membrane (ESM) was obtained from fresh hen eggs purchased from Walmart by removing the liquid content of yolk and white via a hole cut in the eggshell. The eggshell waste with its membrane was washed with deionized water (DIW). DIW (>18.4 MΩ cm^{-1}) was used for preparation of aqueous solution and all chemicals used in this investigation were analytical grade and were used without further purification.

5.2.2 Preparation of the NiO/C nanocomposites

In a typical procedure, NiO/C nanocomposites were obtained using a two-step method with minor revision [152, 160]. To the eggshell "container", a 25 mL water solution of 0.4 M $Ni(NO_3)_2$ $6H_2O$ was added (inside), then the eggshell reactor was partially immersed in a 40 mL solution with 0.4 M urea inside a beaker, and the two solutions were separated by an eggshell with its membrane. The reactor was transferred into an oven and maintained at 70 ℃ for 6 h. The as-coated eggshell membrane pieces were peeled off from eggshell and washed with water thoroughly and dried in a vacuum oven (60 ℃ for 4 h). The color changed from the white bare ESM to a light green when coated with $Ni(OH)_2$. Second, the as-coated ESM was then heated at a ramp rate of 15 ℃/min to 300 ℃ and kept at the set temperature for 1 h under N_2 protection, then the heating continued at a ramp rate of 10 ℃/min to 500 ℃. Finally, the product (NiO/C) was cooled to room temperature with N_2 protection. Aside from, the compared samples, NiO powders and carbonization of ESM, were prepared with the same procedure.

5.2.3 Fabrication of working electrode

Initially, a glassy carbon electrode (GCE) was polished to remove any form of contaminants from the surface. The as-prepared catalyst (4 mg) was dispersed in water/ethanol solution with a volume ratio of 1:1 (with the total volume of 2 mL). The mixture was kept under continuous sonication at (frequency of sonicator) for (time of sonication) to obtain a homogenous catalyst ink. 6 μL of this ink (2 mg/mL) was coated onto the surface of a polished GCE with a diameter of 4 mm, then 6 μL Nafion solution was dropped on the modified GCE in order to keep the catalyst ink stable and enhance

its conductivity. It was dried under ambient environment condition to obtain a uniform catalyst film with geometric surface area of 0.1256 cm^2 and the mass loading of active materials of about ~0.09 mg/cm^2. The modified electrodes containing NiO/C nanocomposites, NiO powders, carbonization of ESM were named as NiO/C@GCE, NiO/GCE and C/GCE respectively.

5.2.4 Characterization

The crystalline information and morphology of those samples were characterized by X-ray diffraction (XRD) with Cu Kα irradiation (λ = 1.54056 Å), Scanning electron microscopy (SEM, FEI Siri200), Transmission electron microscopy (TEM, JEOL 2100F) under an acceleration voltage of 200 kV and element mapping on a Philips Tecnai G2 microscope. All the electrochemical tests were performed on an electrochemical workstation (BioLogic SP-150, France). The electrochemical impedance (EIS) study was performed within the frequency range of 100 kHz to 0.1 Hz with an AC amplitude of 10 mV.

5.2.5 Electrochemical measurements

All the electrochemical measurements were performed on a BioLogic potentiostat/galvanostat/EIS analyzer (SP-150, France) in a typical three-electrode system consisting of the working electrode (WE), counter electrode (CE) and reference electrode (RE). Herein, the glassy carbon electrode (GCE, Φ = 4 mm) coated with the as-prepared catalyst loading was used as the WE, the Pt wire and the saturated Ag/AgCl

electrode as the CE and RE, respectively. The mass loading of active materials was about 0.03 mg/cm^2. The HER performance was investigated by cyclic voltammetry (CV) and linear sweep voltammetry (LSV) which conducted from -0.8 to -1.8 V with a scan rate of 5 mV/s in 1 M KOH. EIS measurements were performed inside the three-electrode electrochemical cell. The Nyquist plot was carried out with over-potential of 135 mV and over a frequency range of 0.1 to 10^6 Hz. An equivalent Randles circuit model was used to fit the data to calculate the charge transfer resistance R_{ct} for each catalyst system. All potentials were referenced to the reversible hydrogen electrode (RHE) scale according to the Nernst equation. ($E_{RHE}=E_{Ag/AgCl}$ + 0.059*pH + 0.21 V, 25℃). The collected data were IR-corrected for an ohmic drop of ~10 Ω in 1 M KOH. All the tests were carried out at room temperature (~25 ℃).

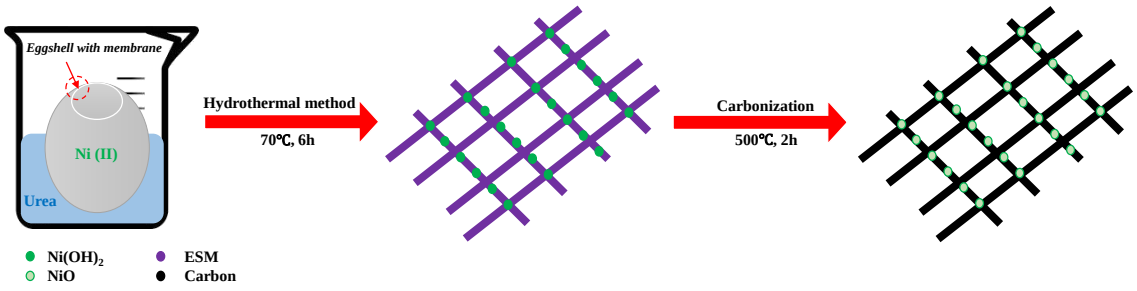

Figure 5.1 Schematic diagram for the formation of NiO/C nanocomposites

5.3 Results and discussion

5.3.1 Characterizations of the as-prepared samples

The successful synthesis of NiO/C nanocomposites by the procedure is outlined in Fig. 5.1. The NiO/C nanocomposites were fabricated via a green chemical route which

combined the hydrothermal method and pyrolysis. The surface morphologies of carbonization of ESM, NiO particles and NiO/C nanocomposites were observed by SEM and TEM. The SEM images of the above samples can be seen in Fig. 5.2. As shown in Fig. 5.2a-b, it exhibits a uniformly structure and high surface porosity with a smooth surface after carbonization of ESM. The carbonized sample seemed to easily provide more open space for anchoring nanoparticles [161]. Then NiO particles, were used in a simple method that combined hydrothermal approach and pyrolysis, is presented in Fig. 5.2c-d. It can be clearly seen that most of the particles were aggregated and with different sizes (~4±1 μm). It can be said that the structural morphology of the NiO particles is the result of two factors: the formation of $Ni(OH)_2$ happened in liquid environment without dispersed protection and the particles easily aggregated during pyrolysis. The carbonization of ESM and NiO particles were also confirmed by using an EDS technique. However, there was a morphological difference observed from the single component, that NiO particles and carbonization of ESM, with the hybrid nanocomposites. In Fig. 5.2e-f, the NiO nanoparticles are homogeneously distributed on the curly surface of the carbonized nanosheet. There are two possibly reasons for this phenomenon, (1) Ni(II) ions were absorbed on the surface of ESM, then $Ni(OH)_2$ grew on the surface of the ESM uniformly after OH^- was introduced into the eggshell reactor. (2) $Ni(OH)_2$/ESM was carbonized into NiO/C nanocomposites after a high temperature procedures [155], therefore the carbonized ESM kept the positions of Ni(II) stable in the process, as shown in Fig. 5.1. Finally, the successful synthesis of NiO/C nanocomposites were also confirmed by corresponding Ni, O and C elemental mapping (Fig. 5.2g).

The morphological structure of NiO/C nanocomposites were further investigated by TEM images. Fig. 5.3 shows the different magnification of NiO/C nanocomposites. It reveals that there are a large number of nanoparticles anchored on the surface of carbonized ESM without any appearance of particle agglomeration. From the histogram shown insert Fig. 5.3b, it can be calculated that the average size of NiO in NiO/C nanocomposites is approximately 5±1 nm. The NiO particles in the eggshell reactor formed at smaller diameters (4 ± 1nm) compared to the control (5 ± 1 nm). This difference is possibly due to the protection of the eggshell membrane, avoiding direct contact between Ni(II) ions and OH^- in solution [162]. The carbonized ESM provided more conductive media for NiO nanoparticles [157], simultaneously, the density of NiO nanoparticles increased due to shrink of ESM during carbonization [150]. This change may also bring the enhancement of catalytic performance toward the hydrogen evolution. Therefore, carbonization of ESM plays an important role in passivating the nanoparticles from further growth and provides a narrow particle size distribution of the NiO nanoparticles.

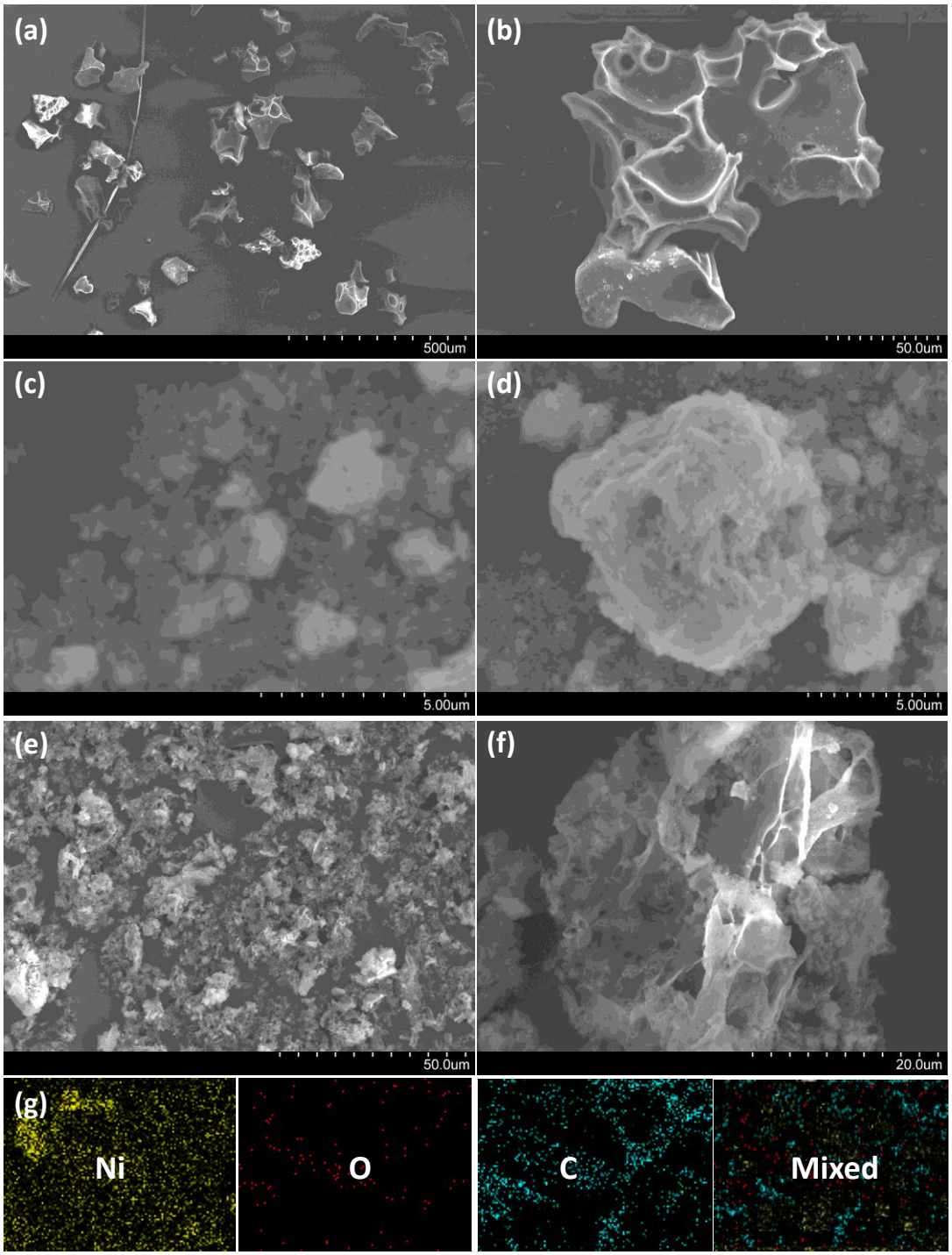

Figure 5.2 SEM images of: (a-b) *carbonization of ESM*, (c-d) NiO powders, (e-f) NiO/C nanocomposites. (g) EDS elemental mapping images of the NiO/C nanocomposites

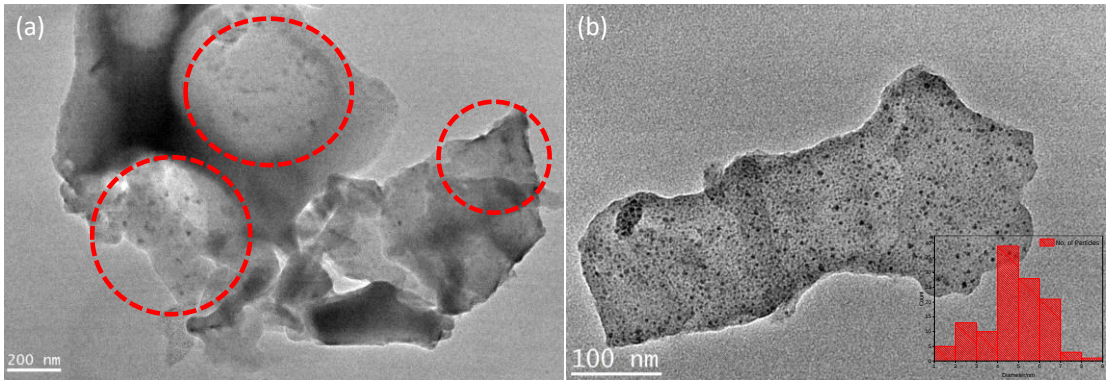

Figure 5.3 TEM images for NiO/C nanocomposites with different magnifications, (a) 200 nm and (b) 100 nm

To further investigate the phase purity and crystalline structure, the as-prepared samples were examined by X-ray diffraction (XRD). As shown in Fig. 5.4, it displays the XRD patterns of the comparison sample (activated carbon) and the as-obtained NiO/C nanocomposites which was synthesized by the two-step approach. There are five well-defined diffraction peaks at 37.2, 43.2, 62.8, 75.4 and 79.4 degree (2theta), which are well indexed to (111), (200), (220), (311), and (222) crystal planes indicated that the formation of NiO nanoparticles from the intermediated $Ni(OH)_2$. The nature and positions of the above XRD result are in good agreement with standard XRD data (JCPDS No. 47-1049) and other previously reported research [146], and NiO nanoparticles shows the cubic (fcc) phase. In addition, the diffraction angle (2theta) around 24 degree is amorphous carbon (JCPDS No. 41-1487). It also proved that this as-prepared activated carbon is made of amorphous carbon. No peaks from other impurities such as $Ni(OH)_2$ were observed. Furthermore, the as-obtained nanocomposites confirmed the existence of NiO nanoparticles and amorphous carbon without any detectable impurities. The co-existence of NiO nanoparticles and amorphous carbon peaks in XRD pattern confirms that the NiO/C nanocomposites are

synthesized well. The XRD and SEM characterization results are in line with TEM observation and EDS results (Figs. 5.2 and 5.4).

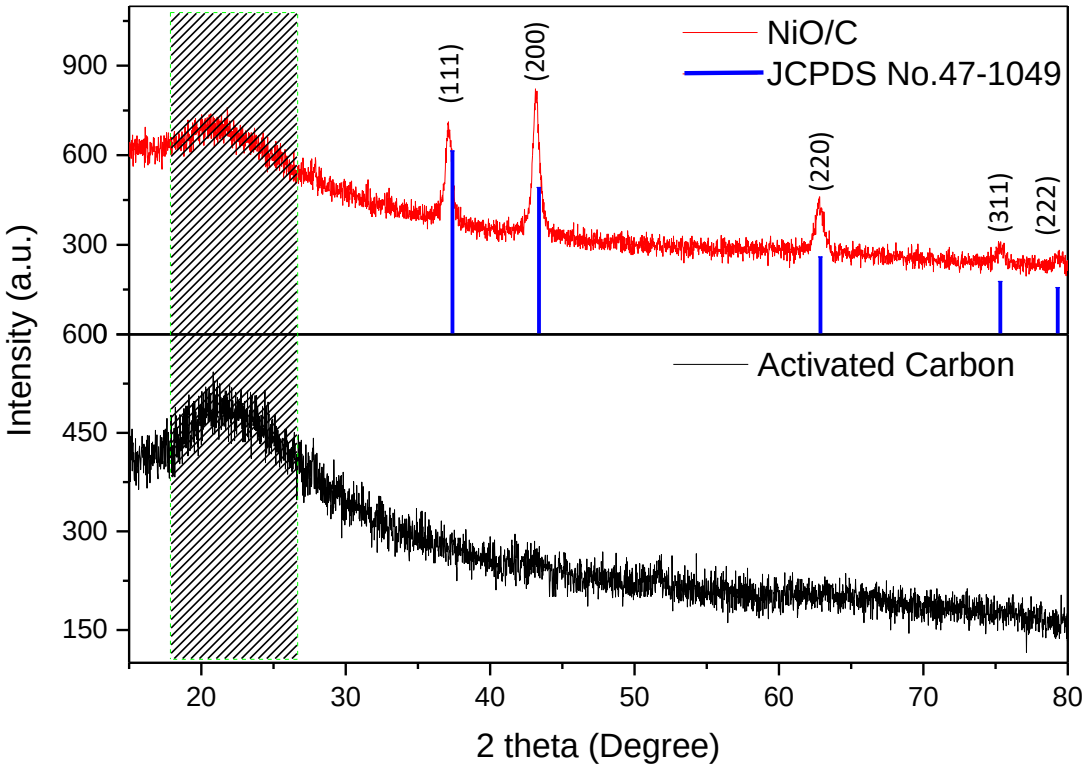

Figure 5.4 The XRD patterns of *carbonization of ESM* (black line), NiO/C (red line) and NiO's JCPDS card (blue line)

5.3.2 Formation mechanism

From the observed SEM, EDS, TEM and XRD results, the possible pathway for the formation of the NiO/C nanocomposites was proposed. The whole process mainly undergoes the following three steps as presented in Fig. 5.5. At first, urea acts as the hydrolysis agent which decomposes to form OH^- ions in aqueous condition as $Ni(NO_3)_2$ $6H_2O$ solution was added into the empty eggshell. Ni^{2+} ions were gradually absorbed on the surface of ESM through the pores of ESM (blue layer). Then, the ESM served

as bio-template to provide a reactor for the Ni^{2+} ion and OH^- ion to form $Ni(OH)_2$. The relative reactions are presented as follows [160, 163]:

$$CO(NH_2)_2 + H_2O \rightarrow CO_2\uparrow + 2NH_3\uparrow \quad (1)$$

$$NH_3 + H_2O \rightarrow NH_4^+ + OH^- \quad (2)$$

$$Ni^{2+} + 2OH^- \rightarrow Ni(OH)_2\downarrow \quad (3)$$

After this process, the resultant $Ni(OH)_2$/ESM hybrid had a morphology very similar to the ESM template. Finally, $Ni(OH)_2$/ESM hybrids were transformed into NiO/C nanocomposites after carbonization. The $Ni(OH)_2$ formed-nanoparticles, rather than aggregated powders or particles because the ESM provides specific pore sites for Ni^{2+} ions, and prevents aggregation of $Ni(OH)_2$ during drying and carbonization. Therefore, NiO/C nanocomposites were successfully constructed via a hydrothermal and pyrolysis approach using ESM as the carbon source.

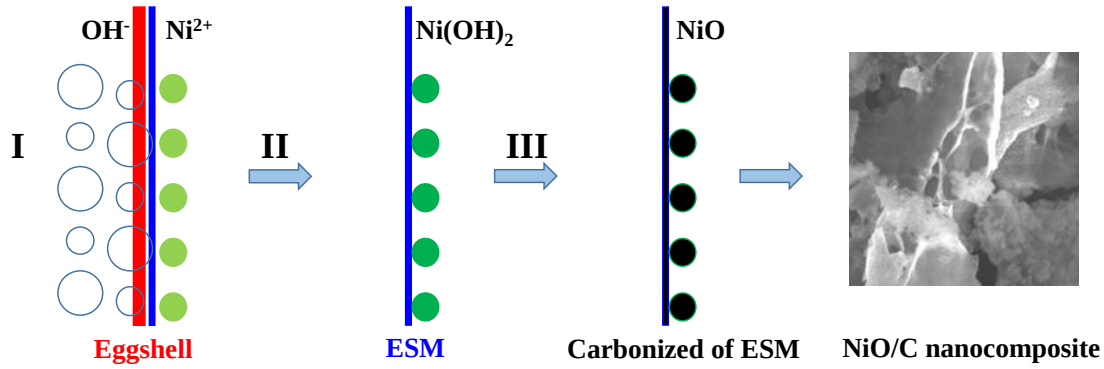

Figure 5.5 Schematic illustration of proposed formation mechanism of NiO/C nanocomposites

5.3.3 HER performance of the NiO/C nanocomposite

The HER performance of NiO/C nanocomposites was tested by linear sweep voltammetry technique (LSV) by sweeping the potential from 0.05 V to negative potentials in 1.0 M KOH solution with a scan rate of 5 mV/s. Fig. 5.6a exhibits that the polarization curve for NiO/C nanocomposite modified electrode (red line), named NiO/C@GCE. For comparison, we also investigated bare GCE, carbonization of ESM modified electrode and NiO particle modified electrode, called GCE (black line), C@GCE (pink line) and NiO/GCE (blue line), respectively, as presented in Fig. 5.6a. The overpotential of NiO@GCE reaching at -10 mA/cm^2 and -30 mA/cm^2 were 670 mV and 753 mV respectively. Additionally, the open circuit potential (E_{oc}) of NiO@GCE is obviously lower than ideal NiO vs. 0.132 V_{RHE}[164]. This may due to the structure of NiO (Figs. 5.2c-d) and aggregation of NiO particles reducing the number of active sites, decreasing electron transfer rate during the HER process, compared with NiO nanoparticles in Figs. 5.2e-f. In another comparison of carbonization of ESM, C@GCE, it had better performance with values of 617 mV and 688 mV at -10 mA/cm^2 and -30 mA/cm^2 respectively, than NiO@GCE did. The overpotential of the reported current density of -10 mA/cm^2 and -30 mA/cm^2 of NiO/C@GCE is 565 mV and 644 mV, respectively. This HER activity is better than pure NiO and carbonization of ESM, indicating that NiO/C@GCE can reach higher current density than NiO@GCE and C@GCE under the same testing conditions. It is also easier to find the hydrogen bubble released during NiO/C@GCE'LSV test (inset of Fig. 5.6a). Here, carbonization of ESM provided a support for NiO nanoparticles to reduce aggregation [165, 166], as can be seen from the TEM images. This is due to the

coupling effect of carbon with NiO nanoparticles, which greatly improves the conductivity of nanocomposites and electron transfer rate [146, 167].

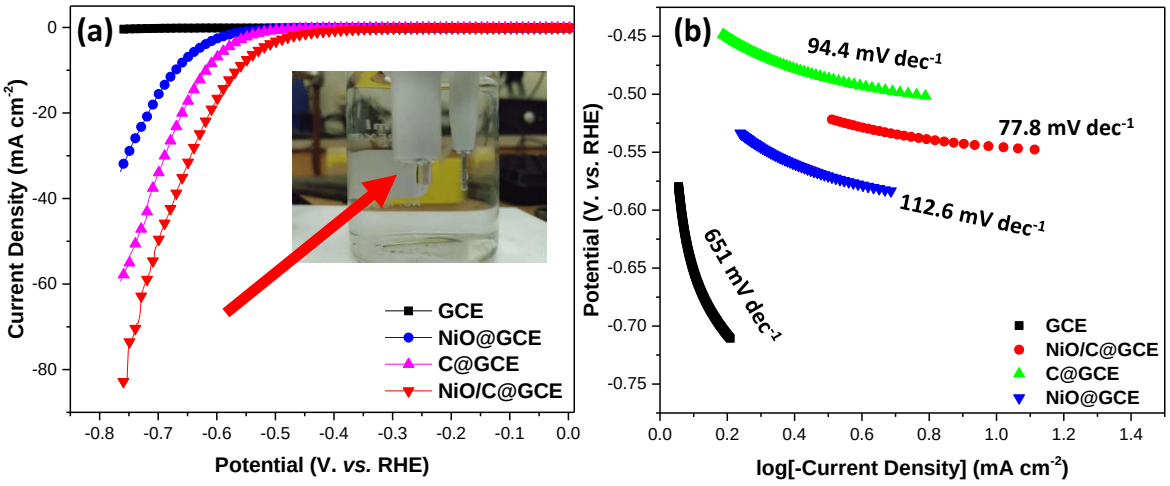

Figure 5.6 (a) Comparison of the polarization curves of GCE, NiO@GCE, C@GCE and NiO/C@GCE, scan rate: 5 mV/s, inset: image of HER process; (b) Tafel plots of GCE, NiO@GCE, C@GCE and NiO/C@GCE in an N_2-saturated 1M KOH solution.

The HER kinetics of the catalysts were further studied by corresponding Tafel slopes. The Tafel slope is derived from the polarization curves by fitting data to the Tafel equation:

$$\eta = a + b*\log[\text{-current density}]$$

Where, b is the Tafel slope, as presented in Fig. 5.6b.

The NiO/C@GCE shows a smaller Tafel slope (77.8 mV dec^{-1}) compared to NiO@GCE's Tafel slope (112.6 mV dec^{-1}) and C@GCE's Tafel slope (94.4 mV dec^{-1}) respectively. This result also supports the enhanced HER activity of NiO/C@GCE via

coupling effect between the HER performances of NiO@GCE and C@GCE. Normally, HER process often includes three typical reactions (I) Volmer reaction, (II) Heyrovsky reaction and (III) Tafel reaction with corresponding different Tafel slopes of 120, 40 and 30 mV dec^{-1}, respectively, as shown in Equation4-6. However, there are two possible pathways in alkaline solution: they have the same start procedure producing H adsorbed (H_{ads}), in which the H_2O molecule was adsorbed on the surface of electrode via molecule interaction and electrochemical reduction (Equation 4). Then for the (1) pathway, the next step is H_2O molecule is reacted with H_{ads} in order to obtain H_2 (Equation 5). But for the (2) pathway, the continued step is that different H_{ads} reacted each other generating H_2 directly (Equation 6). Consequently, the experimentally measured Tafel slope of 77.8 mV dec^{-1} for NiO/C@GCE indicates that the HER occurred by Volmer-Heyrovsky mechanism [148, 168]. The comparison list of Tafel slope of the various electrocatalysts is reported in Table 5.1. NiO/C nanocomposites showed higher Tafel slope value as compared with the other metal oxide-based catalyst reported in the literature.

$$H_2O + e^- \rightarrow H_{ads} + OH^- \qquad \text{Volmer} \qquad (4)$$

$$H_2O + H_{ads} \rightarrow H_2 + OH^- \qquad \text{Heyrovsky} \qquad (5)$$

$$H_{ads} + H_{ads} \rightarrow H_2 \qquad \text{Tafel} \qquad (6)$$

Table 5.1 Comparison of Tafel slope value of various electrocatalysts.

Catalyst	Tafel Slope (mV dec^{-1})	Medium	Reference
C@NiO/Ni nanofibers	152	Alkaline	[146]
Ni/NiO	244	Alkaline	[139]
$CoNi_2S_4$	85	Alkaline	[169]
$NiCo_2O_4$/CuS carbon fiber paper	41	Acidic	[170]
Ni/NiO/C	44	Acidic	[171]
NiO/C nanocomposites	77.8	Alkaline	In this work

To probe the reasons for the enhanced electrocatalytic performance of the NiO/C nanocomposites, the electrochemical impedance spectroscopy (EIS), the CV and LSV techniques were employed. The EIS test was employed to evaluate the transport kinetics for electrochemical reaction process. Fig. 5.7a shows that the Nyquist plots of NiO/C and activated carbon (Commercial product, as comparison). It is observed that the Nyquist plot of NiO/C is almost linear, while that of the carbonization of ESM and activated carbon displayed a similar trend which consists of a quasi-semicircular arch at high frequencies and an oblique line at low frequencies. It is well established that a larger semicircle means a larger charge transfer resistance (R_{ct}) and a steeper slope represents a lower resistance of electrolyte ions (Warburg impendence, Z_w). According to the Nyquist plot fitted by the equivalent circuit (inset of Fig. 5.7a), the R_{ct} of NiO/C nanocomposites, carbonized of ESM, activated carbon and NiO particles are 0.68, 1.04, 0.97 and 1.06 Ω, respectively. Thus, it is obvious that the NiO/C composite has a smaller R_{ct} than the carbonization of ESM and NiO particles. This indicates that the as-prepared nanocomposites has a faster electron transfer process due to the coupling effect between carbonization of ESM and NiO nanoparticles. In additional, the double-

layer capacitances (C_{dl}) which is linearly proportional to the effective electrochemical active surface area, were also calculated. We found that the C_{dl} of NiO/C was significantly higher 1.5 times that of NiO's, though the C_{dl} of NiO is only 0.48 mF cm^{-2} (Fig. 5.7b). We believe that this larger effective active surface area is due to more uniform distribution of NiO nanoparticles on the surface of carbonized ESM, as can be found from the TEM images. Besides, we found the carbonized of ESM and activated carbon has similar electrochemical properties in terms of R_{ct} and C_{dl}, it also confirmed the performance of that carbonized of that ESM can replace commercial activated carbon. Overall, the smaller R_{ct} and the larger C_{dl} suggest achievement of synergistically electronic and structural modulations for HER performance between the carbonization of ESM and the NiO nanoparticles.

The influence of scan rate was also tested by conducting LSV curves with a NiO/C@GCE. According to the LSV curves (Fig. 5.7c), the current density increases at the same potential with increasing scan rate. Because the larger scan rate induces larger reaction current and electric double layer charging current [172]. As a result, more hydrogen was generated and diffused from the surface of the working electrode. All these factors should contribute to the enhanced catalytic performance of the NiO/C nanocomposites. Finally, the stability of the NiO/C nanocomposite was also evaluated by conducting a CV test between 0.25 V and 0.55 V in 1 M KOH solution. As can be seen from Fig. 5.7d, after 500 cycles, change of the current density at certain overpotential is small. Although metal oxides are not known for good performance on HER, the as-prepared NiO/C nanocomposites showed a good durability [134, 140].

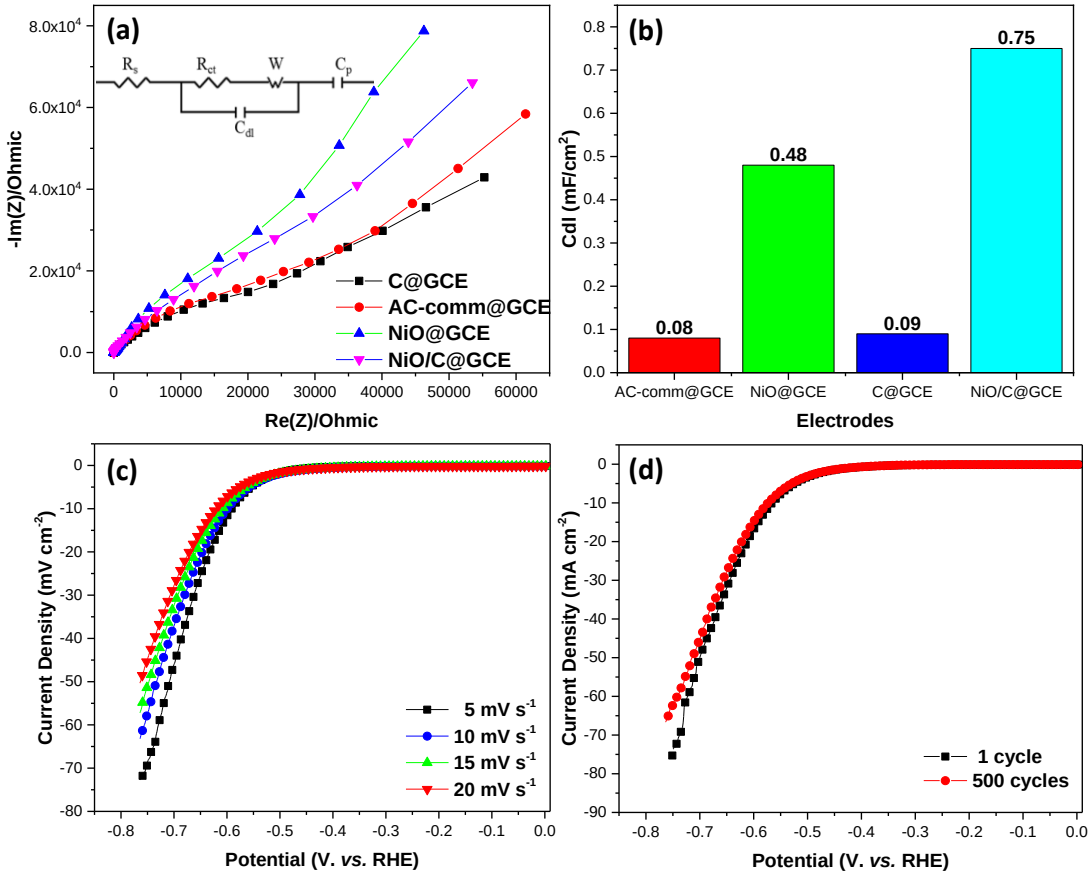

Figure 5.7 (a) EIS plots of C@GCE, AC-comm@GCE, NiO@GCE and NiO/C@GCE at 0.10 V vs. RHE, Inset: equivalent circuit; (b) Current density differences plotted as a function of the potential scan rate (the slope for C_{dl}) pink plots for GCE, black for NiO/GCE, blue for C@GCE and red for NiO/C@GCE; (c) Polarization curves of NiO/C nanocomposites at different scan rates. (d) Durability testing of NiO/C@GCE by cycling the electrode between 0.25 and 0.55 V in an N_2-saturated 1M KOH solution.

5.4 Conclusions

In summary, NiO/C nanocomposite derived from $Ni(OH)_2$/ESM composite was successfully prepared by a facile and green approach that combined simple hydrothermal and pyrolysis methods. Here, the waste eggshell was regard as an useful resource for the as-synthesized sample. It not only provides ESM for the adsorbed Ni(II) ions, but only works as a reactor for this preparation. Consequently, it has been observed that NiO nanoparticles distributed on the surface of ESM uniformly. The as-prepared NiO/C nanocomposite showed stable electrocatalytic and high activity

towards HER in alkaline solution. It also needs a lower overpotential of 565 mV to drive -10 mA cm^{-2} with Tafel slope of 77.8 mV dec^{-1} than the compared samples. Moreover, the preparation approach addressed a facile, economic and green strategies for the preparation of other metal oxides with a carbon support and provided an important example for a strategy to enhance their electrical conductivity and improve their HER performance in alkaline solution.

CHAPTER 6 CONCLUDING REMARKS

6.1 Conclusions

In this dissertation, we conducted a series of investigations based on the eggshell membrane-derived carbon and employed the novel porous material as a multifunctional electrocatalyst for urea oxidation, urea detection, and hydrogen production. In addition, the theoretical investigation was also performed to explore the mechanism of urea oxidation on the eggshell membrane-derived carbon. Based on the research works which have been done, the following conclusions can be made:

- The nickel oxide nanoparticles supported on the carbonized eggshell membrane with interwoven networks as a low-cost electrocatalyst (C@NiO) toward urea oxidation. The resulting C@NiO electrode exhibited much better electrocatalytic urea oxidation performance than that of commercial 20% Pt/C under the same test conditions. It can achieve a current density of 10 mA cm^{-2} at 1.36 V (*vs* RHE) and 25 mA cm^{-2} at 1.46 V (*vs* RHE) and a low Tafel slope of 87.2 mV dec^{-1}. Such an excellent urea oxidation performance can be attributed to the synergetic effect of the porous carbon and NiO nanoparticles that provide excellent electrocatalytic activity and stability in the C@NiO nanocomposites. Moreover, benefitting from theoretical calculations, Ni(III) species and porous carbon further enabled the electrocatalyst to effectively inhibit the CO_2 poisoning of the electrocatalyst, guaranteeing its superior UOR performance. This study may promote a low-cost UOR electrocatalyst design with a porous structure and uniform composition and develop biomass-derived applications in urea conversion based on the concept of trash to treasure.

- In this work, the single-atom model where NiO nanoparticles were bonded with graphene as the NiO@Graphene composite was constructed for the electrochemical urea oxidation in terms of a theoretical view. DFT calculations showed that NiO nanoparticles dispersed on graphene provide strong adsorption of the hydroxyl group; then, NiOOH@Graphene was formed after NiO@Graphene reacted with the hydroxyl group. Compared to NiO@Graphene, NiOOH@Graphene presents a higher desorption energy of CO_2 molecules in the key rate-determining step. Notably, the Ni(III) species in NiOOH@Graphene is the most favorable site for the urea oxidation reaction. Moreover, NiOOH@Graphene not only guarantees the stability of NiOOH and graphene but also promotes the electron transfer between NiOOH and graphene. Benefiting from the coupling effect between the Ni(III) species and graphene, NiO@Graphene can theoretically reach excellent electrocatalytic urea oxidation. These studies provide theoretical guidance that NiO@Graphene played the intermediate role in the urea oxidation process before Ni(III) species formed in the alkaline electrolyte. NiOOH@Graphene also facilitates the desorption of CO_2 from the catalyst surface for UOR catalysis. More experimental investigations based on the NiO nanoparticles and graphene will be performed in the future.
- As for urea detection part, NiO/*c*-ESM nanocomposites were experimentally prepared by a simple two-step method and employed as an electrocatalyst for urea detection. ESM as biowaste was used as precursor in this synthesis and making full use it. *c*-ESM with the large surface area provides a place for anchoring of the NiO nanoparticles uniformly. NiO/*c*-ESM modified electrode exhibits a wider linear range (0.05 to 2.5 mM), and a low detection limit of

~20 μM (signal noise ratio is 3). Besides, the as-prepared electrochemical sensor presents good selectivity and satisfactory results in real sample application. In this study, 3D NiO/*c*-ESM nanocomposite electrode exhibits good performance and robust durability towards urea detection is attributed to the synergistic effect of more active sites from NiO nanoparticles and the carbonized porous eggshell membrane.

- Lastly, NiO/C nanocomposite derived from $Ni(OH)_2$/ESM composite was successfully prepared by a facile and green approach that combined simple hydrothermal and pyrolysis methods. Here, the waste eggshell was regarded as an useful resource for the as-synthesized sample. It not only provides ESM for the adsorbed Ni(II) ions, but works only as a reactor for this preparation. Consequently, it has been observed that NiO nanoparticles distributed on the surface of ESM uniformly. The as-prepared NiO/C nanocomposite showed stable electrocatalytic and high activity towards HER in alkaline solution. It also needs lower overpotential of 565 mV to drive -10 mA cm^{-2} with a Tafel slope of 77.8 mV dec^{-1} than the compared samples. Moreover, the preparation approach addressed a facile, economic and green strategies for the preparation of other metal oxides with carbon support and provided an important example for the strategy to enhance their electrical conductivity and improve their HER performance in alkaline solution.

In summary, the research and development of bio-inspired materials will become a wise choice for getting excellent quality and reasonable price in the application of electrochemical devices.

6.2 Significance

- Based on the concept of ‘trash to treasure’, the common wastes can be converted into energy efficiently to achieve the goal of ‘one stone two birds’
- The mechanism of urea oxidation was both understood by using experimental and theoretical investigations.
- The biomass-derived carbon can be used for more electrochemical applications. It is not limited to the use all described in this dissertation.

6.3 Recommendations for Future work

In the future, the research work should be developed deeply. More detailed parameters and mechanism of the urea oxidation should be figured out through more experiments and characterizations. Specifically, more stable and cheaper devices are going to be constructed and applied to wider fields. For example, urea oxidation reaction was extensively studied, the related work ‘urea-assisted hydrogen production’ is also important as well as single hydrogen evolution reaction. The porous biomass-derived carbon has more merits. It is worth exploring in the future.

APPENDIX A SYNTHESIS OF AU@ZIF-8 NANOCOMPOSITES FOR ENHANCED ELECTROCHEMICAL DETECTION OF DOPAMINE[6]

A1 Introduction

Dopamine (DA) is a well-known neurotransmitter, playing important roles in the brain and body [173, 174]. However, a deficiency of DA in the human body could lead to neurological disorders, but a high level of DA could cause an increased risk of depression [175]. So, the significance of DA in the clinical diagnostic perspectives has drawn great awareness for the development of sensitive and reliable techniques for their determination [176-178]. A series of detective methods have been reported for DA determination, such as spectrophotometry, flow injection, and electrophoresis [112, 173, 179-181]. Among them, electrochemical methods have the advantages of simple instrumentation, high sensitivity and selectivity, and rapid response [173, 182-185].

Zeolitic imidazolate framework-8 (ZIF-8), which is a kind of ZIFs built from Zn^{2+} ions and 2-methylimidazolate, is an attractive subclass of metal-organic frameworks (MOFs) due to the ease preparation, the great thermal, hydrothermal and chemical stabilities [186-189]. There have been increasing concerns about the application of MOFs in the electrochemical field [190-192]. However, most of the MOFs are insulators and the direct application of single MOFs in electrochemistry is limited by their poor conductivity and weak electrocatalytic abilities [188, 192-194]. To address this problem,

---

[6] Appendix A, in full, is a reprint of the research paper titled 'Synthesis of Au@ZIF-8 nanocomposites for enhanced electrochemical detection of dopamine' as it published on the journal of ***Electrochemistry Communications***. Shun Lu, Matthew Hummel, Ke Chen, Yue Zhou, Shuai Kang, Zhengrong Gu. 114 (2020): 106715. Shun Lu was the primary investigator and first author of this article. It is noted that this article received the honor of highly cited paper from Web of Science.

it was proposed to introduce the highly electrically conductive and electroactive materials into MOFs, further improving the sensitivity of the modified electrode. Metal nanoparticles decorated MOF compounds exhibit significantly enhanced performance including high electrical conductivity and outstanding electrocatalytic activity [195-197]. These features have led to the increasing use of MOFs/metal nanoparticle (NP) composites in the fabrication of electrochemical biosensors [198-200]. Among the more commonly used metal NPs, gold (Au) is the most widely studied. Au NPs have been broadly reported for their high catalytic activity which could facilitate the electron transfer rate [201].

Herein, Au@ZIF-8 nanocomposites were successfully fabricated and modified on glassy carbon electrode (GCE) for electrochemical determination of dopamine. The as-prepared nanocomposites show high sensitivity, low LOD (limit of detection), good selectivity, reproducibility and stability for the determination of DA due to the synergistic effect of Au NPs and ZIF-8 with larger surface area. It is expected to be applied in practical DA detection.

A2 Experimental

A2.1 Materials

Gold (III) chloride hydrate ($HAuCl_4$, AR), sodium borohydride ($NaBH_4$, AR), polyvinyl pyrrolidone (PVP, M = 20000), zinc nitrate hexahydrate ($Zn(NO_3)_2$ $6H_2O$, 98%), 2-methyimidazole (abbreviated to 2-MeIm) were purchased from Fisher Scientific™ and Sigma-Aldrich™ in USA. Methanol and ethanol were both used with AR grade. The phosphate buffer solution (PBS, 0.1 M was prepared by mixing

Na_2HPO_4 and NaH_2PO_4 stock solution and adjusted pH value with 0. 1 M H_3PO_4 or NaOH, which was used as the supporting electrolyte during the whole process. Ultrapure water (18.5 MΩ, made in Lab) was used throughout the whole experiment.

A2.2 Synthesis of Au@ZIF-8 nanocomposites

Au@ZIF-8 NPs were synthesized using the solvothermal method with minor revision [186, 194]. Briefly, the gold nanoparticle (Au NP) solution was prepared by the reduction of $HAuCl_4$ (39.1 mg) with $NaBH_4$ (38 mg) with the protection of PVP (111 mg). Then, the PVP-stabilized Au NPs were collected by centrifugation and washed three times with ethanol solution after vigorous stirring (30 min). Furthermore, the synthesized Au NP solution (2 mL, 1 mg mL^{-1}) mixed with 2-MeIm (15 mL, 50 mM) in methanol. Afterward, $Zn(NO_3)_2$ $6H_2O$ (15 mL, 50 mM) in methanol was added quickly. The mixed solution was sonicated for 30 min. Subsequently, the violet precipitate was collected by centrifugation and washed three times with ethanol, then dried under vacuum at 60 ℃ for 4 h to yield a dark red powder (named Au@ZIF-8 nanocomposites, seen in **Fig. A.1**). Additionally, ZIF-8 NPs were prepared with the same procedures as a comparison.

A2.3 Fabrication of Au@ZIF-8 nanocomposites modified GCE

For fabrication of electrode, Au@ZIF-8 nanocomposites (1.5 mg) were ultrasonically dispersed in ethanol (1.5 mL) for ~30 min, as shown in Scheme 1. Before modification, the glassy carbon electrode (GCE, 4 mm in diameter) was polished sequentially with

5.0 μm, 0.5 μm Al_2O_3 powder and then washed ultrasonically in distilled water before each experiment. Then, a drop of the suspension (4.0 μL, 1.0 mg mL^{-1}) was covered on the surface of GCE, then cast with Nafion (wt. 5.0%, 4.0 μL) and dried in an inverted beaker at room temperature. The loading catalyst on the GCE is 0.08 mg cm^{-2}.

A2.4 Physical characterization

The morphology and crystalline information were characterized by Scanning electron microscopy (SEM, FEI Siri200), energy dispersive x-ray spectroscopy (EDX), X-ray diffraction (XRD, Rigaku-SmartLab) and transmission electron microscopy (TEM, JEM-2100, Japan) equipped with STEM-EDX. Nitrogen adsorption-desorption isotherms were measured with a Micrometrics instrument (ASAP 2020, USA) at 77 K.

A2.5 Electrochemical measurements

The electrochemical measurements were performed by cyclic voltammetry (CV), electrochemical impedance spectroscopy (EIS), differential pulse voltammetry (DPV) and amperometric *i-t* using a potentiostat (CHI 760e, USA) with equipped software. The electrochemical tests were conducted at room temperature using the three-electrode setting in 0.1 M PBS as an electrolyte. Here, Ag/AgCl (saturated KCl solution) and platinum wire were used as a reference electrode and a counter electrode, Au@ZIF-8 and ZIF-8 were modified on glassy carbon electrodes (GCE) using as working electrode, respectively.

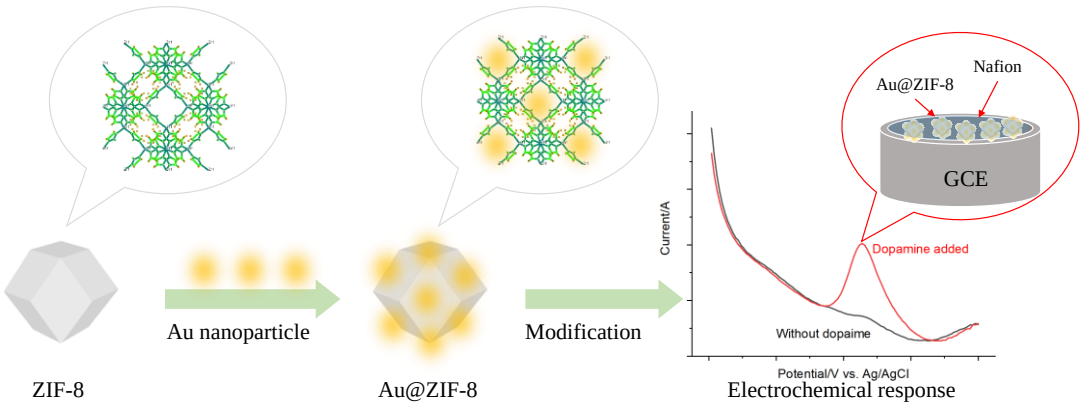

Figure A.1 Illustration of synthesis of Au@ZIF-8 nanocomposite and its electrochemical response toward dopamine.

A3 Result and discussion

The morphologies and structures of the as-prepared nanomaterials were presented in Fig. A.2. Fig. A.2a clearly displays that these nanoparticles are found to be monodisperse, polyhedral in shape with an average size of 270 ± 10 nm. And all the peaks observed in the XRD keep consistency with the simulated result of ZIF-8 (Fig. A.2b) [194]. Fig.1C shows a typical TEM image of Au@ZIF-8 nanocomposites, and the presence of well-distributed Au on ZIF-8 NPs was confirmed by STEM-EDX mapping (Fig. A.2e) which shows uniform distribution of Au on ZIF-8 NPs. The ZIF-8 provided more surface area for Au NPs (black dots in Fig. A.2c) and Au NPs in the edge were dispersed on the surface of the as-prepared nanocomposites. The synergistic effect of between the selectivity of Au NPs and the large surface of ZIF-8 NPs could enhance the analytical performance of this electrochemical sensor. Combined with the above characterizations, it implies that the Au@ZIF-8 nanocomposites were successfully synthesized.

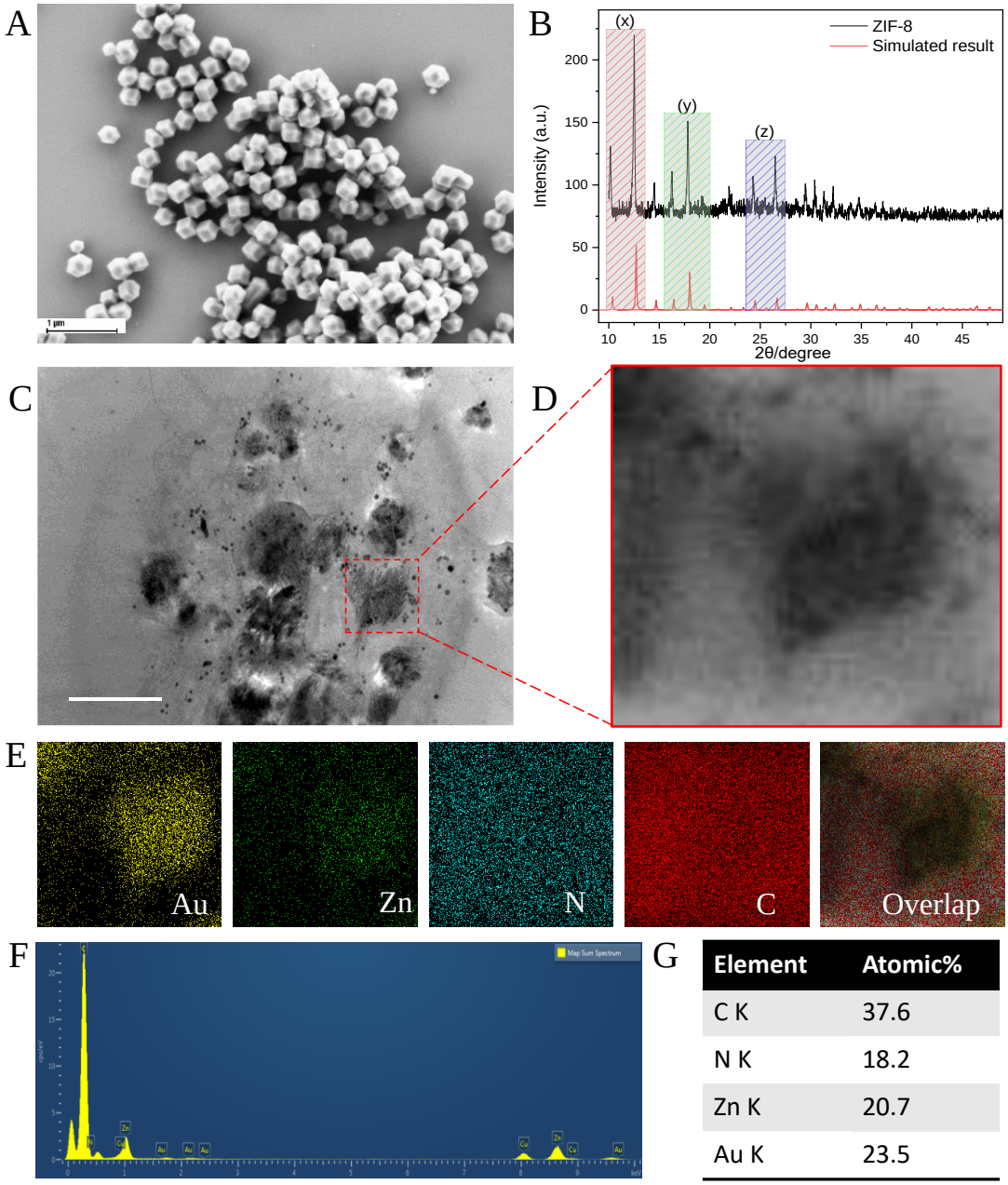

Element	Atomic%
C K	37.6
N K	18.2
Zn K	20.7
Au K	23.5

Figure A.2 (A) SEM image of ZIF-8 NPs, and (B) XRD pattern of ZIF-8 NPs, simulated result from Mercury v3.10.3; (C) TEM image of Au@ZIF-8 nanocomposites, (D) enlarged area from (C), (E) STEM-EDX mapping (Yellow for Au, Green for Zn, Cyan for N, Red for C element) of Au@ZIF-8 nanocomposites, (F) EDX spectrum with detailed table (G).

Nitrogen adsorption-desorption isotherms of Au@ZIF-8 nanocomposites and pore size distribution are shown in Fig. A.3. The N_2 adsorption of Au@ZIF-8 nanocomposites exhibited type I profile, which indicated that Au@ZIF-8 nanocomposites were dominated by microporous structure, as presented in Fig. A.3a. The surface area of

Au@ZIF-8 nanocomposites is 1594 m^2 g^{-1}, and a microporous volume of 0.65 cm^3 g^{-1}, which is a little higher than the pure ZIF-8 nanoparticles' surface area [194, 202]. This is due to the introduction of Au NPs on the surface of ZIF-8, further increase the surface area of the as-obtained materials [202]. The increase in the volume adsorbed at very low relative pressures is owing to the existence of microspores. The pore size distribution calculated using the DFT method showed that Au@ZIF-8 nanocomposites were composed of the uniform pore with a narrow distribution (Fig. A.3b). The above-analyzed results implied that increased specific surface area and unique porous nanostructure of Au@ZIF-8 nanocomposites may provide more active sites or structure for the adsorption of DA on the larger surface, which will contribute to improving the electrocatalytic performance of the modified electrode [173, 197].

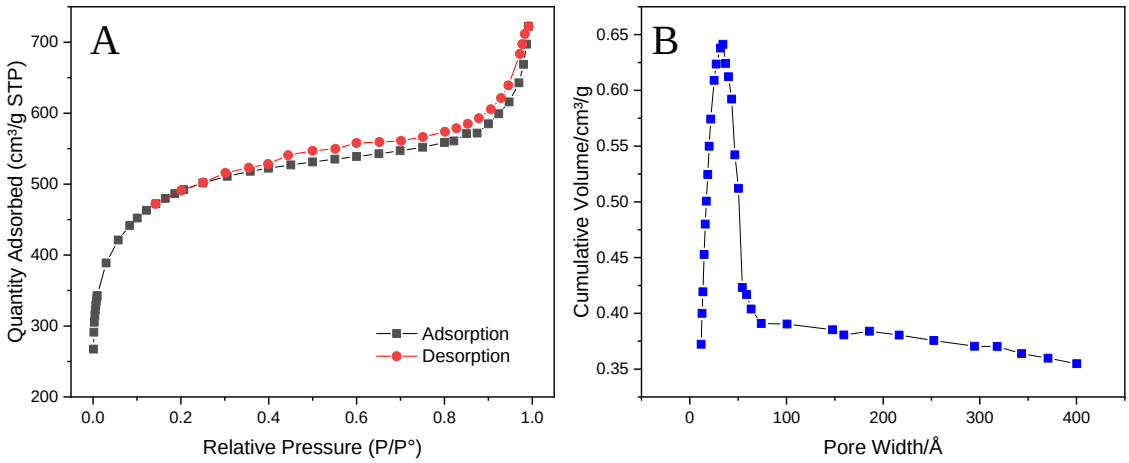

Figure A.3 Nitrogen adsorption and desorption isotherm (A) and the corresponding pore size distribution curve (B) of Au@ZIF-8 nanocomposites.

Electrochemical detection of DA using the Au@ZIF-8/GCE was evaluated by electrochemical measurements. Cyclic voltammogram (CV) was employed to study the electrochemical redox of DA at the different modified electrodes. The electrochemical behavior of two modified electrodes (Au@ZIF-8/GCE and ZIF-8/GCE) in 0.1 M PBS (pH = 7.0) solution in the absence and presence of 0.5 mM DA was examined using

CV from the potential range from -0.2 to 0.6 V (*vs.* Ag/AgCl), as shown in Fig. A.4a. The Au@ZIF-8/GCE exhibits a larger peak current compared to the oxidation current obtained at the ZIF-8/GCE. It indicated that Au@ZIF-8/GCE has a larger relatively electrochemical surface area.

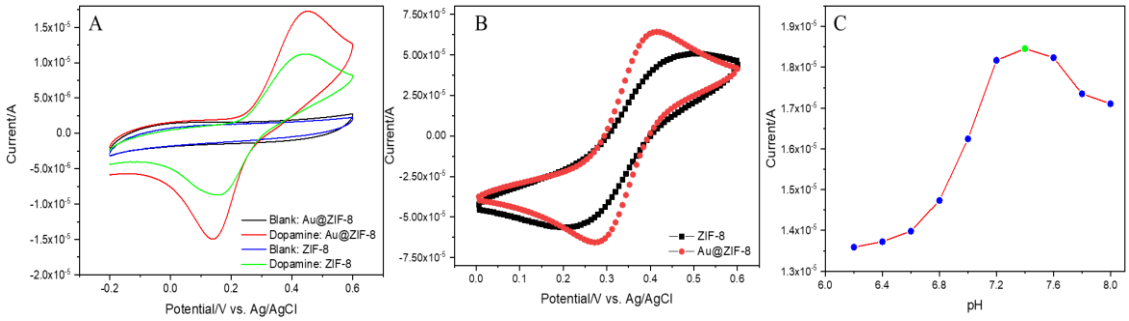

Figure A.4 (A) CVs on the Au@ZIF-8/GCE and ZIF-8 in 0.1 M PBS (pH 7.0) with 0.5 mM DA, scan rate: 50 mV s^{-1}, (B) CVs at Au@ZIF-8/GCE and ZIF-8/GCE in 1.0 mM $[Fe(CN)_6]^{3-/4-}$ solution containing 0.1 M KCl, scan rate: 50 mV s^{-1}. (C) The effect of pH on the current response of 0.5 µM DA at Au@ZIF-8/GCE.

The stepwise fabrication of the electrochemical sensor was also characterized by using CV (Fig. A.4b). The ZIF-8/GCE showed a pair of reduction and oxidation peaks in 1.0 mM $[Fe(CN)_6]^{3-/4-}$ containing 0.1 M KCl (black line in Fig. 3B) with *ca.* area of 1.741 × 10^{-5} (calculated from the given closed curve). After the introduction of Au NPs, a larger pair of redox peaks were appeared (red line in Fig. A.4b) with *ca.* area of 2.104 × 10^{-5}, further confirmed its better charge transferability due to the presence of Au NPs. The effect of pH value of the detecting electrolyte on the electrooxidation of DA was investigated. As shown in Fig. A.4c, the oxidation peak current of DA increased with increasing pH value from 6.2 to 7.4, and decreased from 7.4 to 8.0, therefore, pH 7.6 in 0.1 M PBS was selected as the optimal experimental condition.

Fig. A.5 depicts the linear dependence of the reduction/oxidation peak currents on the square root of the scan rate, which confirming that the oxidation of DA is a typical

diffusion-controlled process. Tafel slopes (Fig. A.6) of Au@ZIF-8/GCE and ZIF-8/GCE were obtained from linear sweep voltammetry (LSV, Fig. A.7), suggesting Au@ZIF-8/GCE performed better electrochemical kinetics than that of ZIF-8/GCE [184, 203].

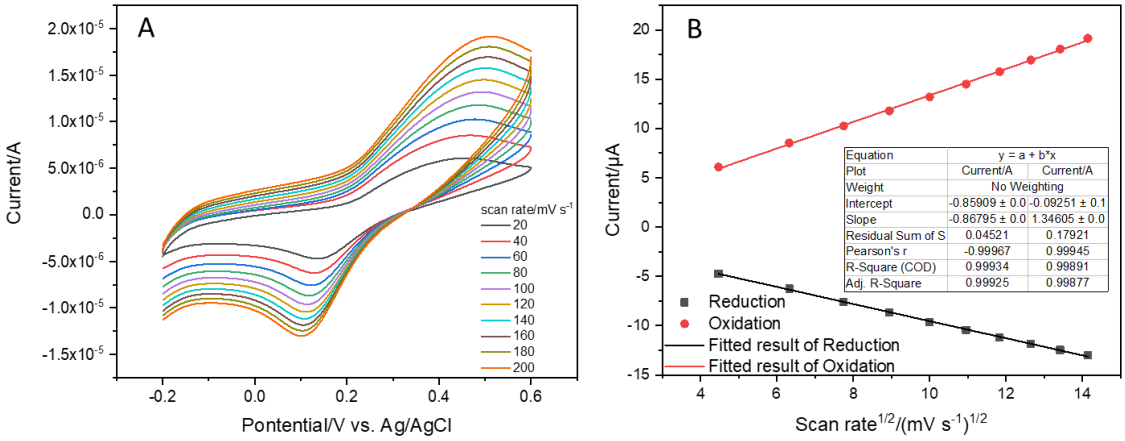

Figure A.5 (a) CVs of Au@ZIF-8 in 0.1 M PBS containing 0.5 μM DA at different scan rates from 20 to 200 mV s^{-1}, and (b) the linear dependence of the reduction peak current and oxidation peak current on the square root of the scan rate.

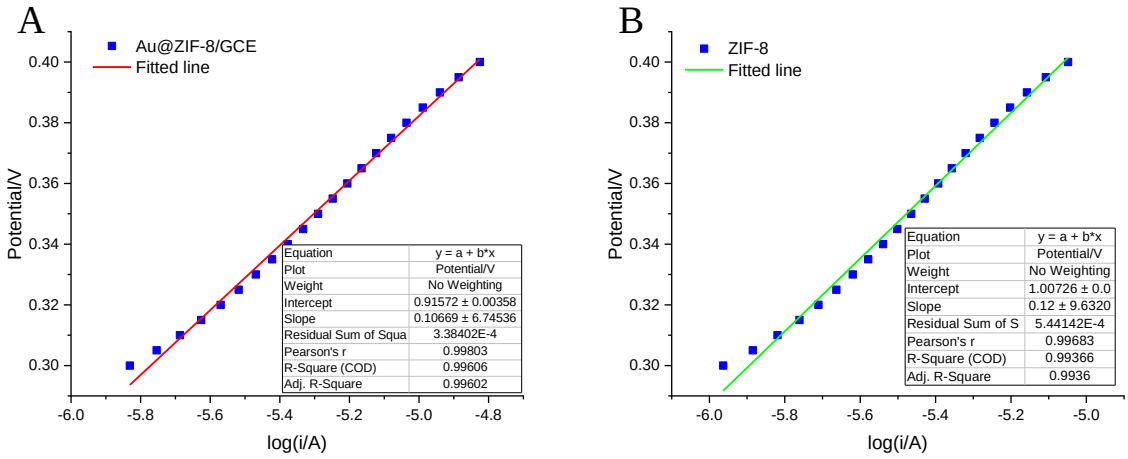

Figure A.6 Tafel plots of (A) Au@ZIF-8/GCE and (B) ZIF-8/GCE with fitted results in 0.1 M PBS (pH 7.4) with 0.5 mM DA.

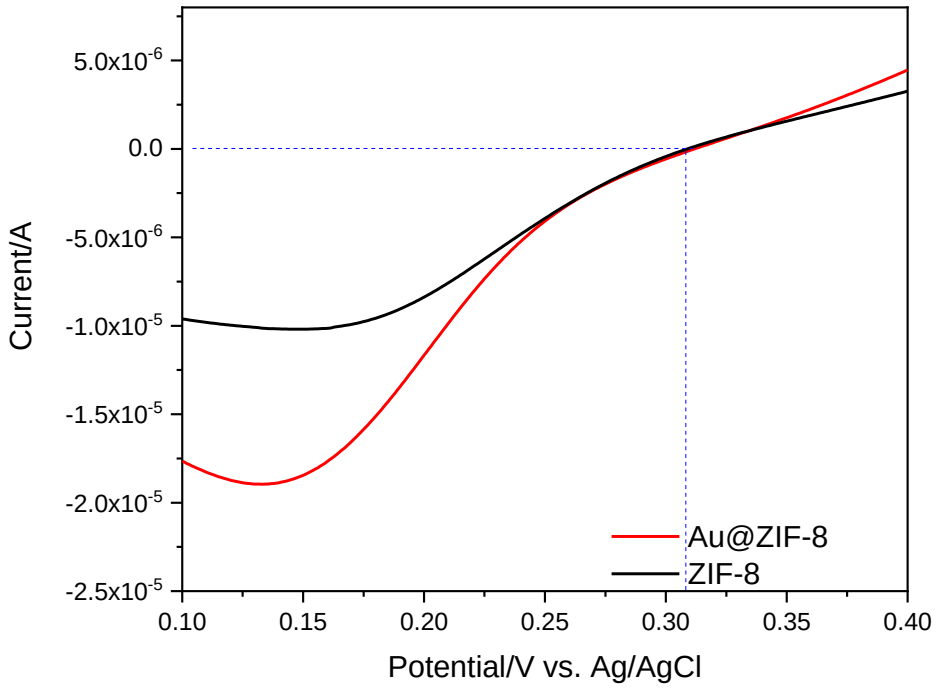

Figure A.7 LSV plots of Au@ZIF-8 and ZIF-8 electrodes in 0.1 M PBS (pH 7.4) with 0.5 mM DA.

The electrochemical double-layer capacitances (C_{dl}) of Au@ZIF-8 is 3 times higher than that of ZIF-8, further confirming its larger active surface areas in the Fig. A.8a [54]. EIS is an effective tool for probing the interfacial behavior of modified electrodes. Fig. A.8b shows that the Nyquist plots of Au@ZIF-8/GCE and ZIF-8/GCE, it is observed that the Nyquist plot of Au@ZIF-8/GCE is almost linear, while that of ZIF-8/GCE with the similar trend which consists of a quasi-semicircular arch at high frequencies and an oblique line at low frequencies. It implies that Au@ZIF-8/GCE acts as a better conducting material and accelerates the electron transfer process at the electrode surface [194]. Consequently, it concluded that the presence of Au NPs, and larger electrochemical surface area and low electrochemical resistance, which synergistic facilitate the oxidation of DA.

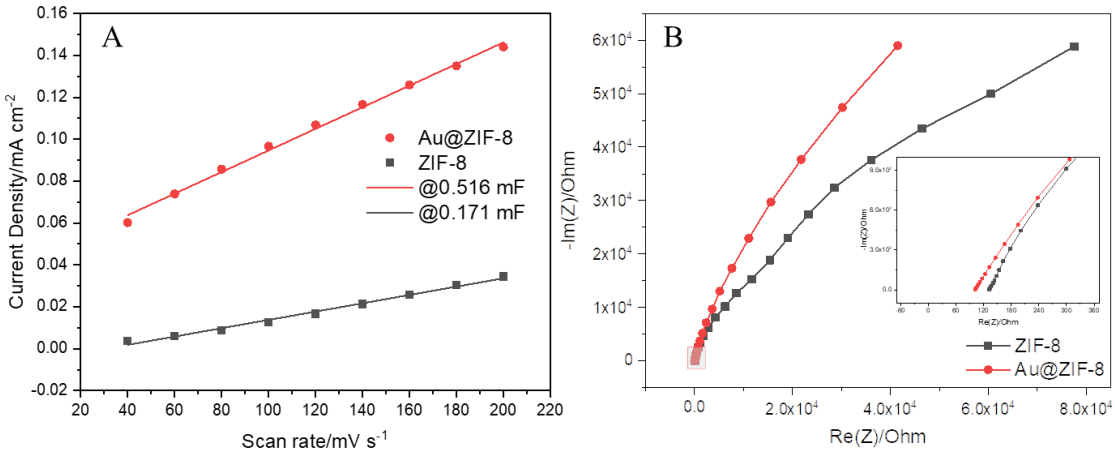

Figure A.8 (a) Plots of the averaged current density at -0.1 V against scan rates. (b) Nyquist plots of ZIF-8/GCE and Au@ZIF-8/GCE in the presence of 0.1 M PBS solution (pH 7.4).

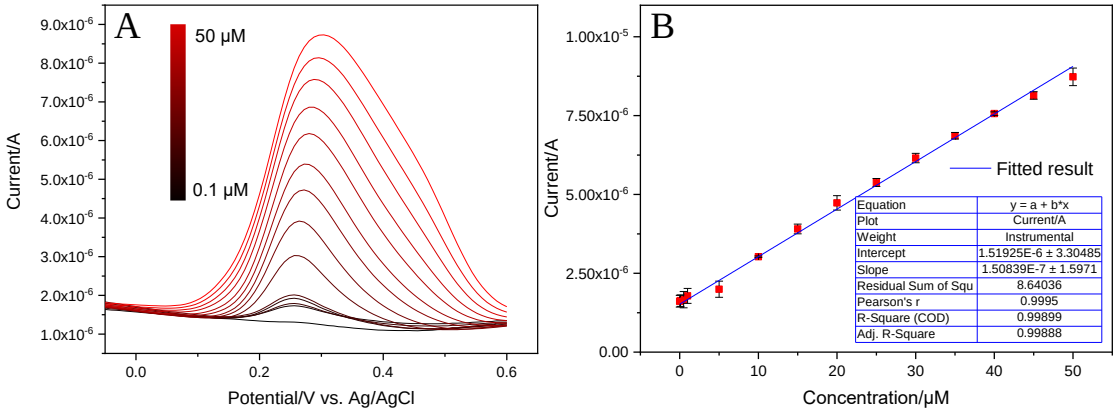

Figure A.9 (A) DPV of DA with increasing concentration (from black to red: 0.1 to 50 μM), (B) The relationship of the oxidation peak current (Ipa) with the concentration of DA.

The performance of the as-prepared electrochemical sensor was investigated by the DPV measurements using the Au@ZIF-8/GCE in 0.1 M PBS (pH 7.4) upon the successive addition of different concentrations of DA solutions, as shown in Fig. A.9a. The electrolyte was stirred for ~10 sec to confirm that the added DA was fully mixed in the electrolyte. The peak at around 0.25 V appeared with the addition of DA. And the peak current gradually increased and was proportional to the DA concentrations

with a wide linear range from 0.1 to 50 μM with the correlation coefficient of 0.998 (Fig. A.9b). The sensitivity of Au@ZIF-8/GCE is calculated to be 6.452 μA mM^{-1} cm^{-2} in the detected concentration range. The proposed Au@ZIF-8/GCE has a larger concentration range than ZIF-8/GCE (Table A.1). Furthermore, the estimated value of LOD (limit of detection) is approximately 0.01 μM (S/N = 3). This may be due to the high conductivity which is essential to the enhancement of electrocatalytic to the detection of DA [204]. It can be found that Au@ZIF-8/GCE exhibited a broader detection range and lower LOD, which had better sensitivity for the DA detection.

Table A.1 Comparison of analytical parameters for detection of dopamine over various modified electrodes

Electrode	Range/μM	LOD/μM	Sensitivity/ μA μM^{-1} cm^{-2}	Method	Ref.
MoS_2 NSB/CNFs[a]	1-60	0.04	6.24	DPV	[205]
P-Arg/rGO/Au NP[b]	1-50	0.001	2.48	DPV	[206]
IL-RGO/ZIF-8[c]	0.1-100	0.035	N/A	DPV	[207]
NPG-μE[d]	0.1-10	0.03	N/A	SWV[e]	[208]
Fe_2Ni MIL-88B/GCE	1.2-1800	0.40	124.7	*i-t*	[209]
RGO-CdSe QD/GCE	4.9–74	0.11	0.16	DPV	[210]
ZIF-8/GCE	0.5-20	0.195	N/A	DPV	[194]

Au@ZIF-8/GCE	0.1-50	0.01	6.45	DPV	This study

a: NSB/CNFs, nanosheet ball/carbon nanotubes

b: poly(L-arginine), reduced graphene oxide and gold nanoparticle modified

c: ionic liquid (IL, [BF_4]) functionalized reduced graphene oxide

d: nanoporous gold-gold microelectrode

e: Square wave voltammetry

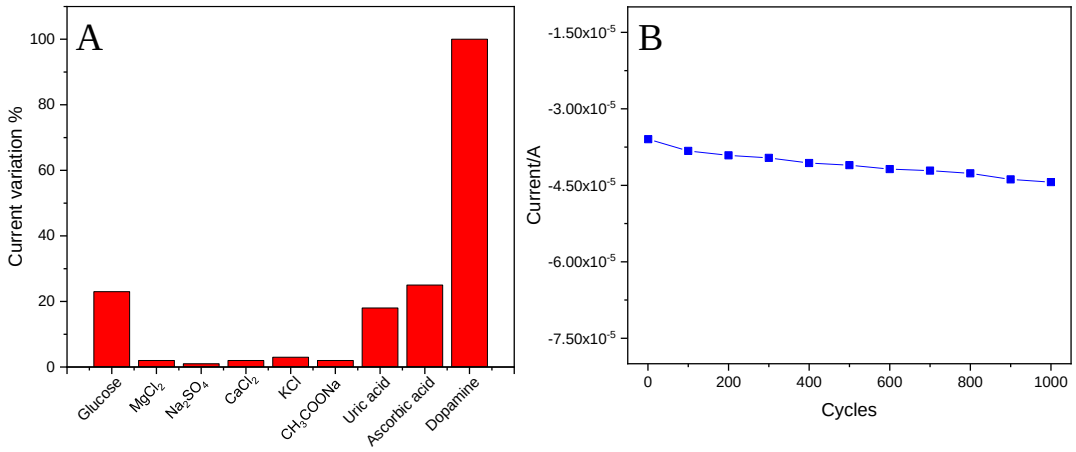

Figure A.10 (A) The signal enhancement of current in the presence of diverse kinds of interfering substance, respectively. (B) The peak currents collected after 1000-cycle CVs run in 0.1 M PBS (pH 7.4) solution containing 5.0 mM DA.

The selectivity of Au@ZIF-8/GCE is studied by detecting DA in the presence of several inorganic salts, glucose (Glu), uric acid (UA), and ascorbic acid (AA). As shown in Fig. A.10a, the addition of inorganic salts, Glu, AA, and UA represented negligible current response compared with DA, suggesting Au@ZIF-8/GCE has an excellent selectivity

to DA. The stability and repeatability of the proposed sensor was also studied. The stability of Au@ZIF-8/GCE was verified after successive 1000-cycle CVs. The oxidation peak current of DA decreased by 18% after 1000 CV cycle, as shown in Fig. A.10b, indicating that good stability and reproducibility can be obtained for electrochemical detection by Au@ZIF-8/GCE. Three paralleled modified-electrodes were prepared with the same condition for evaluating the reproducibility of Au@ZIF-8/GCE by detecting current signal in 0.1 M PBS (pH 7.4) solution with successive addition of 10 μM DA and 0.5 μM urine. The relative standard deviation (RSD) of the electrodes are distributed from 0.9% to 3.3%, as displayed in Table A.2, indicating that Au@ZIF-8 modified electrode is indeed reliable in practical applications.

Table A.2 Determination of DA in the actual samples using Au@ZIF-8/GCE (pH 7.4, n=3)

Sample	Added/μM	Found/μM	Recovery	RSD%
DA injections	0	0	0	-
	10	10.06	100.6%	1.2
	20	19.87	99.35%	2.6
	30	30.72	102.4%	1.8
Urine sample	0	0	0	-
	0.5	0.52	102%	0.9
	1.0	9.86	98.6%	2.4
	1.5	1.62	108%	3.3

A4 Conclusions

In summary, Au@ZIF-8 nanocomposites were successfully fabricated and modified on glassy carbon electrode (GCE) for electrochemical determination of dopamine. The proposed Au@ZIF-8/GCE exhibits better sensitivity than ZIF-8/GCE, it also shows good selectivity and long-term stability. Such selectivity and comparable performance can be attributed to the synergetic electrochemical performance between Au nanoparticles and ZIF-8, and fast charge transferability between the electrochemical sites and the electrode. Therefore, Au@ZIF-8/GCE presents promising performance as a potential non-enzymatic dopamine sensor.

APPENDIX B TWO-DIMENSIONAL CONDUCTIVE PHTHALOCYANINE-BASED METAL–ORGANIC FRAMEWORKS FOR ELECTROCHEMICAL NITRITE SENSING[7]

B1 Introduction

Nitrite (NO_2^-) is a common environmental contaminant that is appeared in the water, soil and other environments, also served as a kind of preservative for the food industry.[211, 212] Nitrite-rich contaminants caused terrible impacts on the ecological environment and public health due to unreasonable utilization/treatment of nitrite in the field of farming, food industry, and environmental protection.[213] Therefore, it is of great importance for the accurate determination of nitrite in the drinking water or pickle foods.[214] Moreover, the World Health Organization (WHO) has established a maximum limit of nitrite dosage of 65.2 μM (3 mg L^{-1}) in drinking water. So, the determination strategy with highly sensitive, selectively and rapid response toward nitrite is imperative. Capillary electrophoresis[215], spectrophotometry[216], and ion chromatography[217], etc. are useful with high sensitivity, but time-cost, more operation skills are required toward the above analytical methods.[218, 219] Over the above approaches, the electrochemical determination has been widely developed owing to its extra merits including real-time, low-cost, feasibility.[55, 112, 220-222]

Metal-organic frameworks (MOFs) were constructed by assembling transition metal ions and organic linkers through coordination reactions. MOFs were firstly utilized for

[7] Appendix B, in full, is a reprint of the research paper titled 'Two-dimensional conductive phthalocyanine-based metal-organic frameworks for electrochemical nitrite sensing' as it published on the journal of *RSC Advances*. Shun Lu, Hongxing Jia, Matthew Hummel, Yanan Wu, Keliang Wang, Xueqiang Qi, Zhengrong Gu. 11.8 (2021): 4472-4477. Shun Lu was the primary investigator and first author of this article.

gas adsorption and storage application due to their porous structure and large surface area.[223] With the exploration of MOFs in the field of electrocatalysis, researchers found MOFs exposed more potential active sites on their larger surface, promoting easily the contact with target molecules, which further improve the electrocatalytic performance of MOFs[224], made MOFs be perfect candidates for sensing.[225] However, great challenges remain for conventional MOFs due to their poor conductive/electronic properties, it is dramatically limited the usage of MOFs in the electrochemical applications.[226-229]

To remove the above challenges, several strategies were put forward, such as i) pyrolysis of MOFs, the carbonized MOFs possessed metal-doped or multi-atoms doped porous carbon, enhancing their electrocatalytic activity[230, 231]; ii) preparation of MOF-based hybrids, conductive supports (carbon nanotube, graphene, metal foams, etc.) were introduced for promoting their electrical conductivity[113, 232]; iii) synthesis of conductive MOFs, the novel conductive MOFs can improve electron transfer capacity directly without pre-treatments[27, 226]. However, well-defined molecular active sites on MOFs are decomposed after the high-temperature process.[233] Also, the second method can promote their electrocatalytic activity to some extent, but it may reduce the inherent advantages of MOFs as well as decrease the surface area and reduce the accessible active sites. The later have more advantages over the other strategies, owing to the development of conductive MOFs which can solve these challenges fundamentally and avoid the former approaches' negative effects.[27]

Two-dimensional (2D) conductive MOFs represent an emerging class of nanomaterials, presenting their exceptional 2D characteristic, enhanced the ability of electron transfer

and the high efficiency of active sites, except the intrinsic merits of conventional MOFs.[234] Such 2D conductive MOFs offer a perfect platform for the study of the mechanism of electroanalysis, which is helpful for the enhanced sensing performance of MOFs.[235] Recently, 2D Ni_3HHTP_2 ($HHTP_2$, hexahydroxytriphenylene) was synthesized for neurochemicals detection due to favorable electron transfer and large surface area.[236] 2D Cu-TCPP (TCPP, tetrakis (4-carboxyphenyl) porphyrin) modified with gold nanoparticles and polyxanthurenic acid with exceptional conductivity was demonstrated as an excellent electrochemical sensor towards dopamine with a low detection limit.[237] 2D conductive materials also played an important role in the gas analysis owing to its excellent conductivity.[235] Based on the above examples, 2D conductive MOFs present their possibilities for achieving superior electrocatalytic performance for electrochemical sensors.[237, 238] However, the usage of 2D conductive MOFs on the electrochemical determination of small molecules has been rarely reported.

In this work, nickel phthalocyanine (NiPc) was selected as an organic linker to assemble 2D NiPc-MOF. Three main reasons arise from using this linker for synthesizing 2D MOF: i) metal active sites are atomically dispersed on metallophthalocyanines theoretically; ii) NiPc-MOFs extended in two-dimension with fully in-plane π delocalization and weak out-of-plane π–π stacking, further promoting electron transfer between electrocatalysts and analytes; iii) the larger surface area of 2D NiPc-MOF, the easier absorbed on the electrode, keeping its electrochemical stability, then achieving excellent sensitivity. Herein, 2D conductive NiPc-MOF was synthesized through the solvothermal method and used for electrochemical determination of nitrite for the first time.

B2 Experimental

B2.1 Synthesis of NiPc-MOF

In a typical synthesis[27], NiPc-NH_2 (60 mg) and $NiCl_2$ $6H_2O$ (42 mg) were both dissolved in DMSO (80 mL). Then, the mixed solution was heated to 70 ℃, followed by the continuous addition of 1.0 mL aqueous ammonia (NH_3 H_2O). After that, the final dark red mixture was softly stirred for 12 h under air at 70 ℃. After cooling to room temperature, the resulting black powder was collected by filtration and the solid product was washed thoroughly with hot DMSO (20 mL * 3), deionized water (20 mL * 3) MeOH (20 mL * 3), and acetone (20 mL * 3) serially. The product as a pure black powder (~65 mg, yield 93.2%) was collected and stored in refrigerator. All raw materials were purchased from chemical reagent company in the USA (Fisher and Sigma-Aldrich) without further purification.

B2.2 Fabrication of the NiPc-MOF electrode

To prepare the 2D NiPc-MOF nanosheets modified electrode, a bare GCE (ø = 4 mm) was polished with alumina slurry (different particle sizes ranging from 50 μm to 10 μm) and then in turn ultrasonically washed in distilled-water and ethanol for 5 min, respectively. 1 mg of 2D NiPc-MOF nanosheets was dispersed into 1 mL ethanol for ultrasonication lasting for 30 min. Then, the prepared suspension was mixed with 5.0 % nafion until a well-dispersed solution was achieved. After that, 10 μL of the uniform mixture solution was cast on the polished GCE and then dried naturally, through which the modified electrode (NiPc-MOF@GCE) was obtained. Also, the NiPc@GCE was fabricated via the same way.

B2.3 Physical characterization

Morphological structure was observed employing a transmission electron microscope (TEM, JEM-2100, JEOL) equipped with scanning transmission electron microscope energy-dispersive X-ray spectroscopy (STEM-EDX, Gatan Inc.). The transmission spectrum was recorded by Fourier transform infrared (FTIR) spectrometer (Nicolet 380, Thermo Fisher, USA) in a range from 400 cm^{-1} to 4000 cm^{-1}. Atomic force microscopy (AFM, FEI SIRION200) was used to study the morphology of the as-prepared sample. In addition, X-ray photoelectron spectroscopy (XPS, Thermo ESCALAB 250XI, Thermo Fisher, USA), and powder X-ray diffraction spectra (PXRD; BL14B station, Shanghai) were recorded to investigate the internal structure of 2D NiPc-MOF nanosheets. All the electrochemical tests were performed on an electrochemical workstation (CHI 760E, CH instruments. Inc., USA).

B2.4 Electrochemical measurements

All electrochemical measurements were carried out using an electrochemical workstation (CHI 760E, CH instruments. Inc., USA) with a typical three-electrode system consisting of the working electrode (WE), counter electrode (CE) and reference electrode (RE). Herein, the glassy carbon electrode (GCE, ø = 4 mm) coated with the as-prepared catalyst loading was used as the WE, the Pt wire and the saturated Ag/AgCl electrode as the CE and RE, respectively. The mass loading of 2D NiPc-MOF nanosheets was about 0.03 mg cm^{-2}. The electrocatalytic performance of 2D NiPc-MOF electrode was investigated by cyclic voltammetry (CV) and differential pulse voltammetry (DPV) in 0.1 M buffer solution. The electrochemical impedance (EIS)

measurements were performed inside the three-electrode electrochemical cell. EIS study was performed within frequency range of 100 kHz to 0.1 Hz with an AC amplitude of 10 mV. An equivalent Randles circuit model was used to fit the data to calculate the charge transfer resistance R_{ct} for each catalyst system. All potentials were referenced to the Ag/AgCl electrode if no specified. All the tests were carried out at room temperature (~25 °C).

B3 Result and discussion

The structural information of the as-prepared sample was explored by powder X-ray diffraction spectroscopy (PXRD), X-ray photoelectron spectroscopy (XPS), transmission electron microscopy (TEM) and atomic force microscopy (AFM). The XRD pattern of the sample in Fig. B.1a exhibits peaks at $2\theta = 4.15°$, 9.85°, and 14.26°, indexed to the lattice planes of (200), (001), and (300), respectively. Long-range order within the *ab*-plane with a center-to-center (Ni···Ni) distance of 9.27Å is further confirmed, which keeps well with the simulation results of NiPc-MOF ($Ni_3(C_{32}H_{16}N_{16})_n$) and no typical peaks of NiPc is found. XPS analysis indicates that the as-prepared sample is composed of Ni, C, N, and O. The Ni 2p spectrum exhibits the typical peaks for Ni $2p_{3/2}$ and Ni $2p_{1/2}$ at 854.6 eV peak 871.9 eV, respectively, which are the characteristic peaks of Ni(III) species (Fig. B.1b).

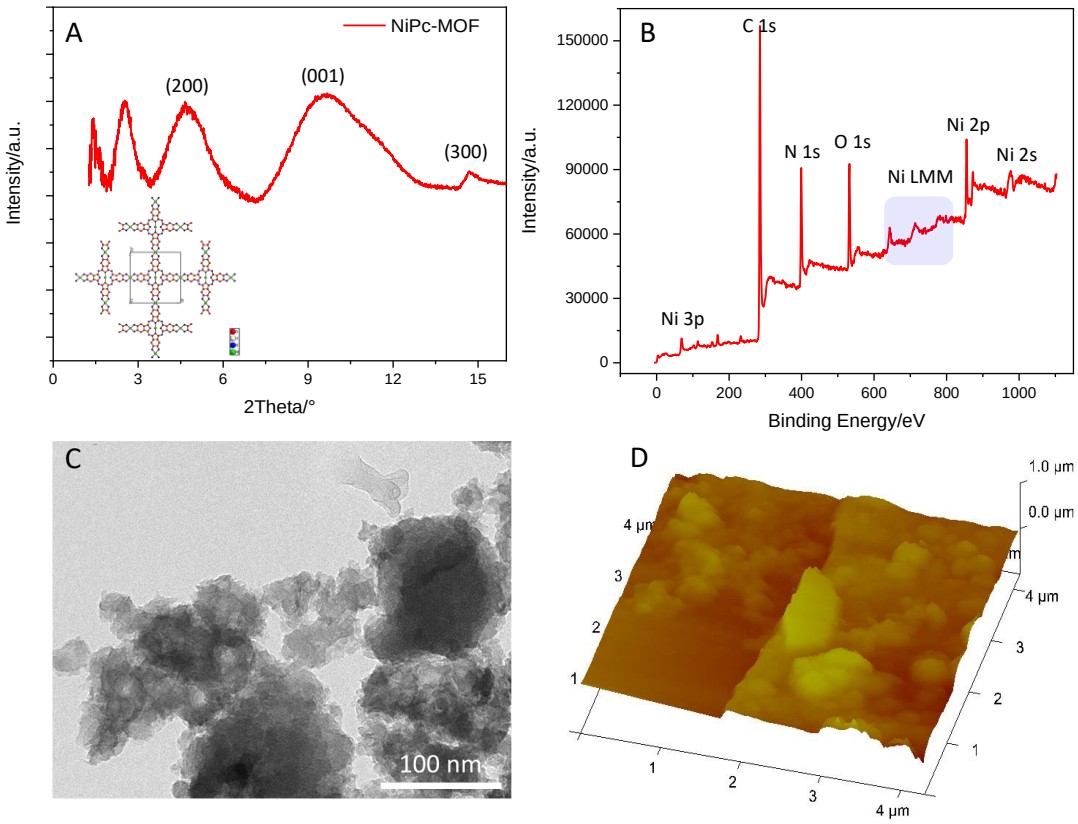

Figure B.1 (a) PXRD patterns of NiPc-MOF and simulated results from its predicted structure; (b) XPS survey spectrum; (c) TEM image and (d) AFM image of 2D NiPc-MOF nanosheets.

TEM image of the as-prepared sample exhibits it has an irregular shape with a nanosheet-like structure, several nanosheets are dispersed well in the view (Fig. B.1c). EDX spectrum of Fig. S3 further confirms its chemical contents including carbon, nitrogen, oxygen and nickel. The AFM (Fig. B.1d) image of the sample exhibits its rough surface, and the corresponding height profile reveals its thickness ranging from 50 nm to 100 nm, indicating the as-prepared sample possesses a multi-layered structure. Furthermore, the FT-IR spectrum of the as-prepared sample presents the typical vibration absorptions of the basic building unit (NiPc) that three peaks at *ca.* 1628 cm^{-1}, 1552 cm^{-1} and 1114 cm^{-1} assigned to C=N stretching, C=C stretching and C-H bending, respectively. Nitrogen adsorption-desorption isotherms of NiPc-MOF

nanosheets was performed at 77 K in Fig. S6. The surface area of NiPc-MOF nanosheets is 543 $m^2 g^{-1}$, which is a little smaller than we previously reported.[27] Combined with the above analysis, it is demonstrated that we have successfully synthesized NiPc-based MOF (NiPc-MOF) nanosheets with both 2D features and typical MOF characteristics.

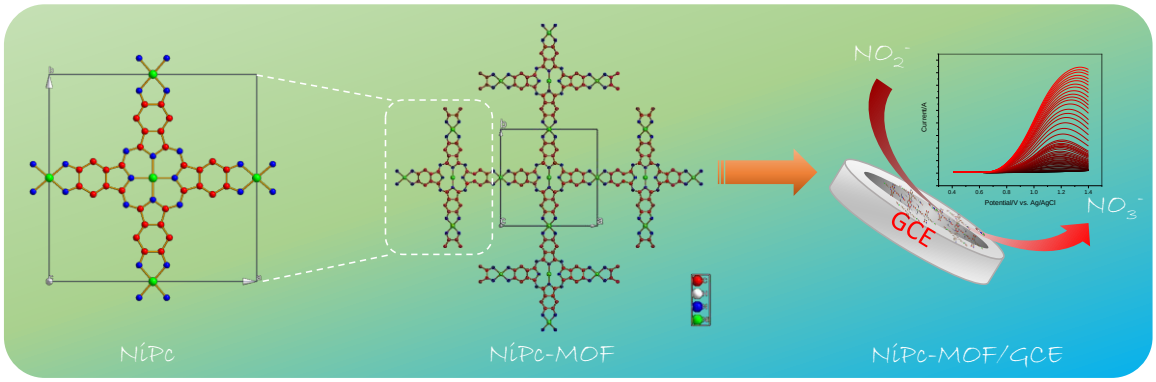

Figure B.2 Schematic of preparation of 2D NiPc-MOF and its electrochemical nitrite detection.

The electrocatalytic performance of the NiPc-MOF electrode towards nitrite was studied, as illustrated in Fig. B.2. Fig. B.3a shows Cyclic voltammograms (CV) curves of NiPc-MOF electrode in 0.1 M phosphate-buffered saline (PBS, pH 7.0) solution with/without 1.0 M nitrite. It can be found that the current response of the NiPc-MOF electrode increases sharply with the addition of nitrite compared to its response in the blank experiment. This means it is possible to achieve nitrite sensing on the surface of the NiPc-MOF electrode. To verify the NiPc-MOF electrode's feasibility, a series of nitrite solution with different concentrations (0.35-0.75 M) was added into the test system, as shown in Fig. B.3b. The result exhibits the relationship of the current response versus concentration is linear well with a co-efficient value of 0.9998 (Fig.

B.3c). It demonstrated that the NiPc-MOF electrode has potential to realize nitrite determination.

Under the optimal conditions, the electrochemical sensing of the NiPc-MOF electrode for nitrite oxidation was carried out by differential pulse voltammogram (DPV). Fig. B.3d presents that the DPV curves at the NiPc-MOF electrode by the successive adding of nitrite with various concentrations from 0.01 mM to 11500 mM. Each DPV curve can be completed within 6 s, exhibiting a fast response toward nitrite sensing. Figs. B.3e-f display the well linear curves between the current response of NiPc-MOF electrode and nitrite concentration with the regression equation: (i) I/μA = 1.995 + 0.028*c (R^2 = 0.999, inset of Fig. B.2e), (ii) I/μA = 53.67 + 0.01*c (R^2 = 0.9999, inset of Fig. B.3f). The sensitivity of the NiPc-MOF electrode is calculated as 0.40 μA mM^{-1} cm^{-2} and 0.14 A mM^{-1} cm^{-2} at low (0.01-2000 mM) and high concentration (2500-11500 mM) region, respectively. Then, a limit of detection (LOD) is estimated as 2.3 μM at signal to noise ratio of 3 (S/N = 3). Additionally, the sensitivity of the NiPc-MOF electrode is slightly greater in the low concentrations from 0.01 to 2000 mM. This phenomenon can be explained as (i) all nitrite ions absorbed on the surface of the NiPc-MOF electrode; (ii) enough active sites on the NiPc-MOF electrode can catalyze them efficiently at a low concentration region. However, the electrocatalytic process is influenced by the competitive effects including nitrite adsorption and catalytic activation on the surface of the NiPc-MOF electrode as the concentration increased, finally decreasing its sensitivity. As well, it is noted that the oxidation peak current appears slightly unstable when the nitrite concentration was beyond 2000 mM. it may be attributed to the adsorption saturation of NO_2^- on the active sites of the NiPc-MOF electrode. Compared with the recent literatures (Table B.1), the sensing performance of

the NiPc-MOF electrode presents a very quick response, low LOD and ultra-wide linear range (0.01-11500 mM).

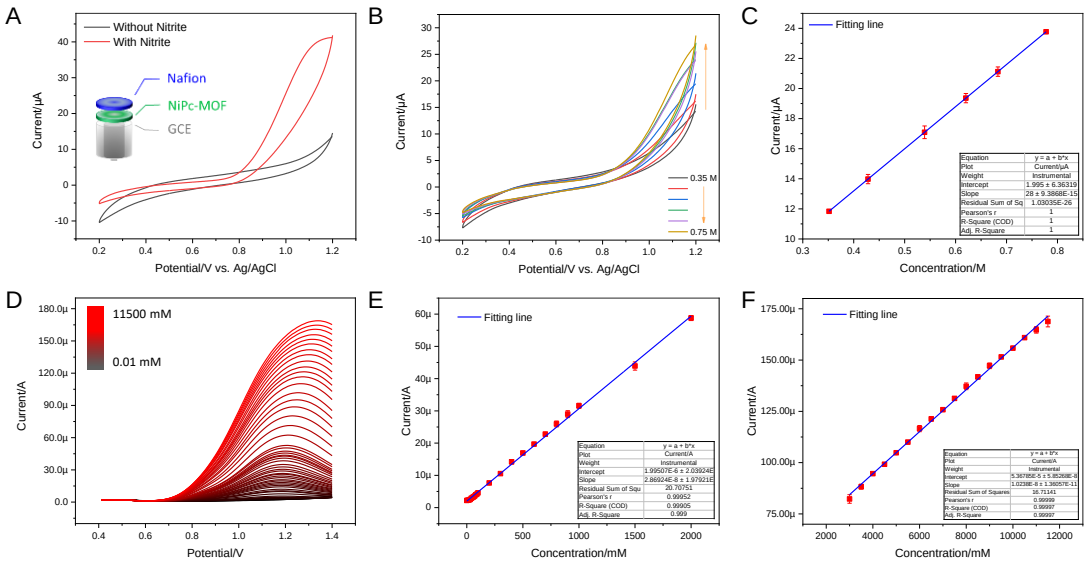

Figure B.3 (a) CV curves of NiPc-MOF electrode in 1.0 M PBS buffer (pH 7.0) in presence and absence of nitrite. (b) CV curves of NiPc-MOF electrode under different nitrite concentrations (0.35-0.75 M), scan rate: 50 mV s-1. (c) Linear calibration curve of Fig. 3c, concentration range: 0.35-0.75 M. (d) DPV curves of 2D NiPc-MOF electrode toward nitrite detection with successive addition (0.01-11500 mM), DPV parameters: amplitude, 0.05 V; pulse width, 0.2 s; sampling width, 0.067 s; pulse period, 0.5 s. (e) Linear calibration curve of Fig. 3d (concentration range: 0.01-2000 mM). (f) Linear calibration curve of Fig. 3d (concentration range: 2500-11500 mM).

Table B.1 Table S1 Comparisons of analytical performance of nitrite on the modified electrodes (from 2018-2020 year)

Material	Electrode	Technique	Linear range	LOD	Refs.
Co_3O_4-rGO/CNTs[a]	GCE[l]	Amperometric i-t	0.1 μM-8 mM	1 μM	[239]
CoTL-MethPc/MWCNTs[b]	GCE	DPV[c]	50-1050 nM	35 nM L^{-1}	[240]
CoPc/MWCNT[d]	GCE	DPV	0.01–1050 mM	2.11 μM	[112]
a-Fe_2O_3/CNTs hybrids	GCE	Amperometric i-t	0.5-4000 μM	0.15 μM	[241]

TiO_2-Ti_3C_2TX/CTAB/CS[e]	GCE	DPV	0-1.25 mM	0.85 μM	[242]
Au/CNHN[f]	GCE	Chronoamperometry	0.05–1150 μM	0.017 μM	[243]
GO-Ag	GCE	LSV[g]	1.0-1000 μM	0.24 μM	[244]
SFh	GCE	Amperometric i-t	0.02–3600 μM	6.3 μM	[245]
$CaFe_2O_4$	SPEi	Amperometric i-t	0.016–1921 μM	6.6 μM	[246]
Poly(TazoCoPc)/CNP[j]	GCE	Amperometric i-t	0.02–1 μM	0.006 μM	[247]
CoTM-QOPc/CNP[k]	GCE	Chronoamperometry	0.1–350 μM	0.033 μM	[248]
2D NiPc-MOF	GCE	DPV	0.01-11500 mM	2.3 μM	This work

a rGO/CNTs, reduced graphene oxide and carbon nanotubes.

b CoTL-MethPc/MWCNTs, tetra L-Methionine cobalt (II) phthalocyanine/Multi-wall carbon nanotubes.

c DPV, Differential pulse voltammogram.

d CoPc, Cobalt phthalocyanine.

e TiO_2–Ti_3C_2TX nanohybrid, hexadecyl trimethyl ammonium bromide (CTAB) and chitosan (CS)

f CNHN, CuNi-based hollow nanoarchitecture

g LSV, linear sweep voltammogram.

h SF, Strontium ferrite

i SPE, screen-print electrode

j Poly(TazoCoPc)/CNP, tetraazo-bridged cobalt phthalocyanine polymer

k CoTM-QOPc/CNP, Cobalt (II) tetra methyl-quinoline oxy bridged phthalocyanine

l GCE, glassy carbon electrode

As shown in Fig. B.4a, CV measurements of the NiPc-MOF electrode were studied in an electrochemical probe solution (5.0 mM ferricyanide and 0.1 M KCl), the NiPc electrode was employed for comparison. It is clearly found that the NiPc-MOF electrode has a larger closed curve area than that of NiPc electrode. This phenomenon means NiPc-MOF nanosheets have better electrical conductivity, faster electron transfer during electrochemical redox. EIS measurement provides valuable information about the interfacial properties of the modified electrode. Fig. B.4b reveals the Nyquist plots of the NiPc and NiPc-MOF electrodes, which exhibit semicircles at the high frequency range corresponding to the electron-transfer-limited process and a straight line at the low frequency range corresponding to the diffusion-limited process.[249] Then, the Randle's equivalent circuit was employed to simulate the obtained Nyquist plots, further understand the electrical properties of the modified electrodes. The electron charge transfer resistance (R_{ct}) could be obtained based on the semicircle diameter of the Nyquist plots. The value of R_{ct} (803.8 Ω) of the conductive NiPc-MOF electrode was much smaller than that of NiPc electrode (1680 Ω), indicating that the NiPc-MOF electrode brought better conductivity to the electrode surface. The acceleration of electron transfer rate was ascribed to the excellent conductivity of 2D NiPc-MOF nanosheets.

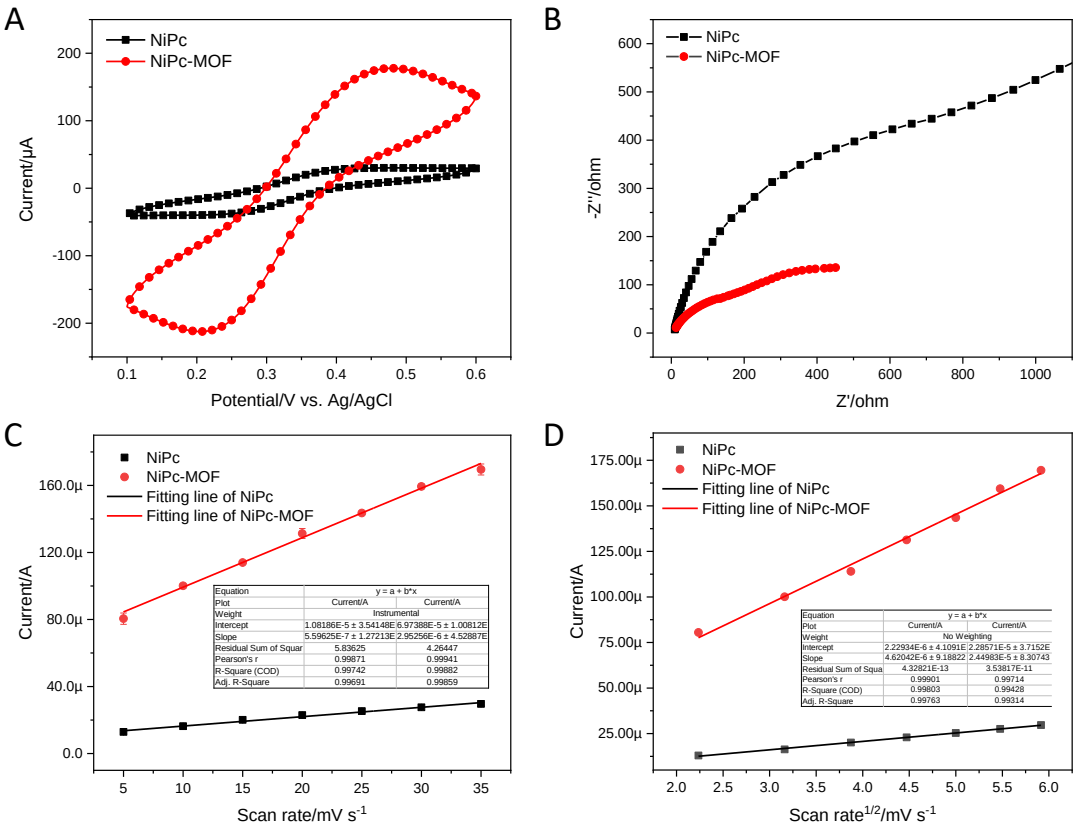

Figure B.4 (a) CV curves of NiPc electrode and 2D NiPc-MOF electrode in 1.0 mM ferricyanide with 0.1 M KCl, scan rate: 50 mV s^{-1}. (b) Nyquist plots of NiPc electrode and NiPc-MOF electrode in 1.0 mM ferricyanide containing 0.1 M KCl. (c) Electrochemical capacitance of NiPc and NiPc-MOF electrode, respectively. (d) The linear relationship between the oxidation peak currents and the square root of the scan rate.

Generally, the double-layer capacitance (C_{dl}) was utilized to evaluate the modified electrode's active surface area. As shown in Fig. 4c, the effective active sites of the NiPc-MOF electrode for nitrite oxidation is obviously larger than that of the NiPc electrode due to the C_{dl} of NiPc-MOF electrode is five times larger than that of NiPc electrode (4.45 μF cm^{-2}). Moreover, the electrochemical active surface area of the modified electrode also reveals the transferred electron on the surface of electrode and determine the active sites for nitrite oxidation.[54, 112] As presented in Fig. B.4d, it has a good linear relationship between the oxidation peak current (I_{pa}) and the square

root of scan rate ($v^{1/2}$). Therefore, the electrochemical active surface area could be determined as stated by the Randles-Sevcik Equation. 1[250]

$$I_{pa} = (2.69 \times 10^5)\, n^{3/2} A D^{1/2} v^{1/2} C_0 \qquad (1)$$

In this Eq. 1, n, A, C_0, D, and *v* are the number of transferred electron, the surface area of the working electrode, reactant concentration, diffusion coefficient, and scan rate, respectively. Based on the known information, the electrochemical active surface area for NiPc-MOF electrode is 5.31 times larger than that of NiPc electrode. Consequently, the NiPc-MOF electrode is favorable for nitrite sensing due to more sensitive response, higher charge transfer efficiency, more catalytically sites and increased the electrochemically active surface area.

Table B.2 Table S2 Determination of nitrite in 0.1 M PBS on the NiPc-MOF electrode (under optimized conditions, n = 3)

Sample		Added/mM	Found/mM	Recovery/%	RSD/% (n = 3)
0.1 M PBS	#1	-	-	-	-
	#2	100	101.7	101.7	3.16
	#3	500	498.4	99.6	2.43
	#4	1000	989.3	98.9	4.27
Tap water	#1	-	-	-	-
	#2	100	93.6	93.6	4.13
	#3	500	508.2	101.6	3.56
	#4	1000	976.4	97.6	3.24

To verify the feasibility of the sensor, the fabricated sensor was utilized to monitor nitrite in real samples (tap water, 0.1 M PBS was employed here as comparison) through a standard addition method. From the analysis results (Table B.2). The recovery values of real samples by the electrochemical method in this work were between 93.6 % and 101.6 %, and the RSD was less than 5%. To confirm the accuracy of the proposed method, 0,1 M standard PBS solution was selected to detect the spiked samples, and the results are consistent with these of our proposed method, suggesting the approach is reliable for nitrite sensing in the real complex environment.

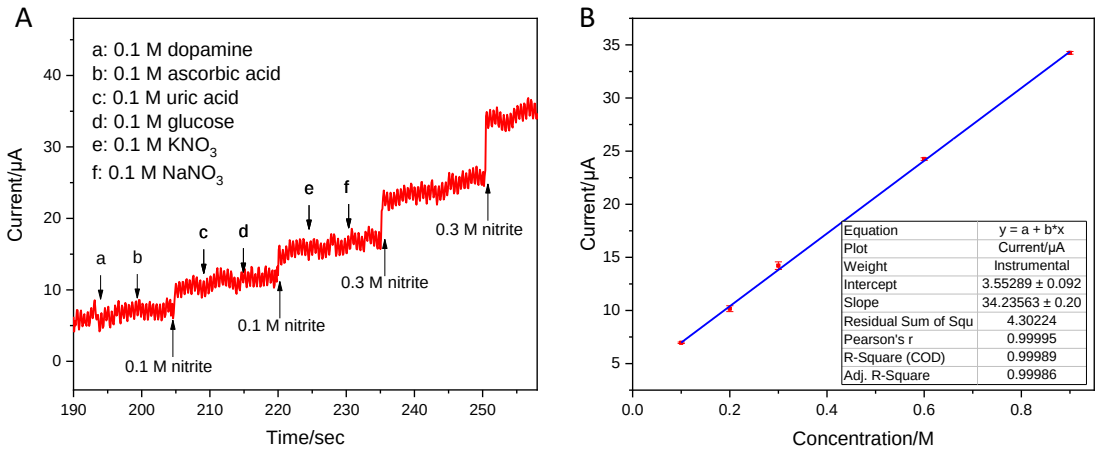

Figure B.5 (a) Amperometry curve of NiPc-MOF electrode in 0.1 M PBS (pH 7.5) with successive addition of dopamine, ascorbic acid, uric acid, glucose, KNO_3 and $NaNO_3$ (all concentrations of interfere species are 0.1 M) at applied potential of 0.9 V. (b) Linear calibration curve of Fig. 5a in the presence of interfere species.

The excellent selectivity is also an important standard for the prepared sensor, the effect of interfere species which possibly coexists with nitrite on the response of the sensor was assessed. Fig. B.5a shows the interference measurement at the applied potential of 0.9 V with continuous additions of 0.1 M nitrite, 0.1 M dopamine, 0.1 M ascorbic acid, 0.1 M uric acid, 0.1 M glucose, 0.1 M KNO_3, 0.1 M $NaNO_3$ and 0.3 M $NaNO_2$ in 0.1

M PBS (pH 7.5). Obviously, a clear i-t response increased is revealed by injection of 0.1 M nitrite into the blank buffer solution. And comparison with the response of NO_2^-, the i-t responses of other interfering species on the sensor were negligible. This phenomenon may be due to the specific electrocatalytic activity toward nitrite. In addition, as shown in Fig. B.5b, the calibration curve of Fig. B.5a exhibits good linearity with a co-efficient value of 0.9998. TEM image of NiPc-MOF nanosheets after nitrite detection is presented, keeping an original morphological structure. This result confirmed that NiPc-MOF electrode possesses great selectivity for the electrochemical detection of nitrite in the presence of multi-interfering species.

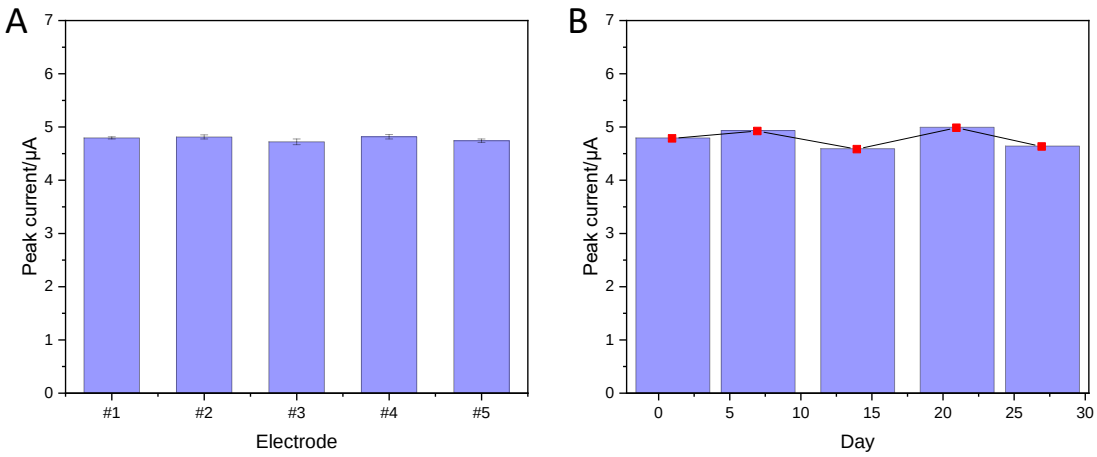

Figure B.6 (a) The repeatability of NiPc-MOF electrodes (#1-5) in 0.1 M PBS (pH 7.5) containing 0.1 M nitrite. (b) The stability of NiPc-MOF electrode: Peak current of DPV in 0.1 M PBS (pH 7.5) containing 0.1 M nitrite. DPV parameters: DPV parameters: amplitude, 0.05 V; pulse width, 0.2 s; sampling width, 0.067 s; pulse period, 0.5 s.

In addition, the repeatability of the as-prepared sensor was also investigated. Five individual electrodes were selected to study the repeatability of the NiPc-MOF electrode here. Five individual electrodes (#1-5) were prepared at the same conditions and applied to detect 0.1 M nitrite, the relative standard deviation (RSD) value was estimated to be 1.65 %. As shown in Fig. B.6a, the repeatability of the sensor was

evaluated with 5 electrodes for detecting 0.1 M nitrite with low RSD value (1.65 %). As displayed in Fig. B.6b, the peak current response of NiPc-MOF electrodes has similar behavior during 4-week (Day 1, Day 7, Day 14, Day 21, and Day 28). During stability tests, the NiPc-MOF electrode was stored at ambient environment and monitored every week via DPV method. The RSD value of 3.82 % was obtained, suggesting the stability of the NiPc-MOF electrode is suitable for long-term nitrite detection. Therefore, all the results suggest the NiPc-MOF electrode is reliable for nitrite sensing due to its excellent stability, repeatability, and long-term repeatability.

B4 Conclusions

In conclusion, two-dimensional nickel phthalocyanine-based metal-organic framework nanosheets (2D NiPc-MOF) based non-enzymatic biosensor for the electrochemical detection of nitrite is firstly developed. The as-prepared sensor exhibited an ultra-wide detection range (0.01-11500 mM) with low limit detection (2.3 μM), meanwhile, it also presents excellent stability and competitive selectivity. The excellent electrocatalytic activity of NiPc-MOF electrode is explained by the following reasons: i) NiPc-MOF nanosheets possess high catalytic sites with the larger electrochemical active surface area for nitrite oxidation; ii) the 2D characteristic of NiPc-MOF nanosheets results in the large surface area to increase the active sites for nitrite detection; iii) Differ from the semi-conductivity of NiPc molecular, NiPc-MOF nanosheets present excellent electrical conductivity, which could enhance electron transfer, improving its sensitivity towards nitrite determination. Overall, the prepared 2D NiPc-MOF nanosheets have great potential in the field of electroanalysis.

BIBLIOGRAPHY

Shun Lu was born in Huaibei, Anhui Province, China on August 19, 1991, the son of Deming Lu and Huimin Ren. After graduating from the Huaibei Normal Middle School and Suixi No.2 Middle School in 2010, then he enrolled at Huaibei Normal University in Anhui, China. Shun received his Bachelor of Science in Materials Chemistry in July of 2014. In September of 2014, he began his graduate education at Southwest University and conducted his research under the supervision of Dr. Ming Nie and Dr. Chi Yang studying the synthesis of metal-organic framework compounds and their energy application. During his Master period, he worked as a visiting student in Southeast University in Nanjing under the supervision of Dr. Chi Yang and Prof. Chunxiang Xu investigating the novel nanomaterials' biomedical application. He earned his Master of Science in Material Science in June of 2017. In August of 2018, Shun entered the Graduate School at the South Dakota State University (SDSU) at Brookings as a Graduate research fellow and began work with Dr. Zhengrong Gu in the Department of Agricultural Biosystems Engineering. In the summer of 2019, he conducted research at Northumbria University in Newcastle, United Kingdom with Dr. Xiaoteng Liu on the electrochemical reduction of CO_2 on the nanostructured materials. Shun obtained the Bob Sather Memorial Scholarship from the Renewable Fuels Foundation in 2021. Following completion of his degree at the South Dakota State University, Shun will continue to work the research group of Prof. Zhengrong Gu at SDSU as a postdoctoral fellow.

REFERENCE

[1] Office HaFCT. Hydrogen Production: Electrolysis.

[2] Kirubakaran A, Jain S, Nema R. A review on fuel cell technologies and power electronic interface. Renewable and Sustainable Energy Reviews. 2009;13(9):2430-40.

[3] Meng J, Chernev P, Mohammadi MR, Klingan K, Loos S, Pasquini C, et al. Self-supported Ni (OH) 2/MnO2 on CFP as a flexible anode towards electrocatalytic urea conversion: The role of composition on activity, redox states and reaction dynamics. Electrochimica Acta. 2019;318:32-41.

[4] Peighambardoust SJ, Rowshanzamir S, Amjadi M. Review of the proton exchange membranes for fuel cell applications. International journal of hydrogen energy. 2010;35(17):9349-84.

[5] Vedharathinam V, Botte GG. Direct evidence of the mechanism for the electro-oxidation of urea on Ni (OH) 2 catalyst in alkaline medium. Electrochimica Acta. 2013;108:660-5.

[6] Venugopal NKA, Joseph J. Electrochemically formed 3D hierarchical thin films of cobalt–manganese (Co–Mn) hexacyanoferrate hybrids for electrochemical applications. Journal of Power Sources. 2016;305:249-58.

[7] Wu Z-S, Yang S, Sun Y, Parvez K, Feng X, Müllen K. 3D nitrogen-doped graphene aerogel-supported Fe3O4 nanoparticles as efficient electrocatalysts for the oxygen reduction reaction. Journal of the American Chemical Society. 2012;134(22):9082-5.

[8] Feng Y, Yu X-Y, Paik U. N-doped graphene layers encapsulated NiFe alloy nanoparticles derived from MOFs with superior electrochemical performance for oxygen evolution reaction. Scientific reports. 2016;6(1):1-8.

[9] Yang D, Yang L, Zhong L, Yu X, Feng L. Urea electro-oxidation efficiently catalyzed by nickel-molybdenum oxide nanorods. Electrochimica Acta. 2019;295:524-31.

[10] Ludewig U, Neuhäuser B, Dynowski M. Molecular mechanisms of ammonium transport and accumulation in plants. FEBS letters. 2007;581(12):2301-8.

[11] Boggs BK, King RL, Botte GG. Urea electrolysis: direct hydrogen production from urine. Chem Commun. 2009(32):4859-61.

[12] Guo F, Ye K, Cheng K, Wang G, Cao D. Preparation of nickel nanowire arrays electrode for urea electro-oxidation in alkaline medium. Journal of Power Sources. 2015;278:562-8.

[13] Zhu D, Guo C, Liu J, Wang L, Du Y, Qiao S-Z. Two-dimensional metal–organic frameworks with high oxidation states for efficient electrocatalytic urea oxidation. Chem Commun. 2017;53(79):10906-9.

[14] Xia L, Liao Y, Qing Y, Xu H, Gao Z, Li W, et al. In Situ Growth of Porous Ultrathin Ni (OH) 2 Nanostructures on Nickel Foam: An Efficient and Durable Catalysts for Urea Electrolysis. ACS Applied Energy Materials. 2020;3(3):2996-3004.

[15] Guo F, Ye K, Du M, Cheng K, Gao Y, Wang G, et al. Nickel nanowire arrays electrode as an efficient catalyst for urea peroxide electro-oxidation in alkaline media. Electrochimica Acta. 2016;190:150-8.

[16] Yang D, Gu Y, Yu X, Lin Z, Xue H, Feng L. Nanostructured Ni2P‐C as an Efficient Catalyst for Urea Electrooxidation. ChemElectroChem. 2018;5(4):659-64.

[17] Zhang J-Y, He T, Wang M, Qi R, Yan Y, Dong Z, et al. Energy-saving hydrogen production coupling urea oxidation over a bifunctional nickel-molybdenum nanotube array. Nano Energy. 2019;60:894-902.

[18] Rollinson AN, Jones J, Dupont V, Twigg MV. Urea as a hydrogen carrier: a perspective on its potential for safe, sustainable and long-term energy supply. Energy & Environmental Science. 2011;4(4):1216-24.

[19] Chen S, Duan J, Vasileff A, Qiao SZ. Size Fractionation of Two‐Dimensional Sub‐Nanometer Thin Manganese Dioxide Crystals towards Superior Urea Electrocatalytic Conversion. Angewandte Chemie International Edition. 2016;55(11):3804-8.

[20] Sha L, Ye K, Wang G, Shao J, Zhu K, Cheng K, et al. Hierarchical NiCo2O4 nanowire array supported on Ni foam for efficient urea electrooxidation in alkaline medium. Journal of Power Sources. 2019;412:265-71.

[21] Yue ZH, Yao SY, Li YZ, Zhu WX, Zhang WT, Wang R, et al. Surface engineering of hierarchical $Ni(OH)_2$ nanosheet@nanowire configuration toward superior urea electrolysis. Electrochim Acta. 2018;268:211-7.

[22] Urbańczyk E, Maciej A, Stolarczyk A, Basiaga M, Simka W. The electrocatalytic oxidation of urea on nickel-graphene and nickel-graphene oxide composite electrodes. Electrochim Acta. 2019;305:256-63.

[23] Radenahmad N, Afif A, Petra PI, Rahman SM, Eriksson S-G, Azad AK. Proton-conducting electrolytes for direct methanol and direct urea fuel cells–A state-of-the-art review. Renewable and Sustainable Energy Reviews. 2016;57:1347-58.

[24] Nguyen NS, Das G, Yoon HH. Nickel/cobalt oxide-decorated 3D graphene nanocomposite electrode for enhanced electrochemical detection of urea. Biosensors and Bioelectronics. 2016;77:372-7.

[25] Yu Z-Y, Lang C-C, Gao M-R, Chen Y, Fu Q-Q, Duan Y, et al. Ni–Mo–O nanorod-derived composite catalysts for efficient alkaline water-to-hydrogen

conversion via urea electrolysis. Energy & Environmental Science. 2018;11(7):1890-7.

[26] Yan W, Wang D, Botte GG. Electrochemical decomposition of urea with Ni-based catalysts. Applied Catalysis B: Environmental. 2012;127:221-6.

[27] Jia H, Yao Y, Zhao J, Gao Y, Luo Z, Du P. A novel two-dimensional nickel phthalocyanine-based metal–organic framework for highly efficient water oxidation catalysis. Journal of Materials Chemistry A. 2018;6(3):1188-95.

[28] Zhan S, Zhou Z, Liu M, Jiao Y, Wang H. 3D NiO nanowalls grown on Ni foam for highly efficient electro-oxidation of urea. Catalysis Today. 2019;327:398-404.

[29] Ma G, Xue Q, Zhu J, Zhang X, Wang X, Yao H, et al. Ultrafine Rh nanocrystals decorated ultrathin NiO nanosheets for urea electro-oxidation. Applied Catalysis B: Environmental. 2020;265:118567.

[30] Wang Z, Liu W, Hu Y, Guan M, Xu L, Li H, et al. Cr-doped CoFe layered double hydroxides: Highly efficient and robust bifunctional electrocatalyst for the oxidation of water and urea. Applied Catalysis B: Environmental. 2020;272:118959.

[31] Sayed ET, Eisa T, Mohamed HO, Abdelkareem MA, Allagui A, Alawadhi H, et al. Direct urea fuel cells: Challenges and opportunities. Journal of Power Sources. 2019;417:159-75.

[32] Simka W, Piotrowski J, Nawrat G. Influence of anode material on electrochemical decomposition of urea. Electrochim Acta. 2007;52(18):5696-703.

[33] Baker DR, Lundgren CA. Expansion of the urea electrocatalytic oxidation window by adsorbed nickel ions. Journal of Applied Electrochemistry. 2019;49(9):883-93.

[34] Yue Z, Zhu W, Li Y, Wei Z, Hu N, Suo Y, et al. Surface engineering of a nickel oxide–nickel hybrid nanoarray as a versatile catalyst for both superior water and urea oxidation. Inorg Chem. 2018;57(8):4693-8.

[35] Yang W, Yang X, Hou C, Li B, Gao H, Lin J, et al. Rapid room-temperature fabrication of ultrathin Ni(OH)2 nanoflakes with abundant edge sites for efficient urea oxidation. Applied Catalysis B: Environmental. 2019;259:118020.

[36] Yang W, Yang X, Li B, Lin J, Gao H, Hou C, et al. Ultrathin nickel hydroxide nanosheets with a porous structure for efficient electrocatalytic urea oxidation. J Mater Chem A. 2019;7(46):26364-70.

[37] Yuan M, Wang R, Sun Z, Lin L, Yang H, Li H, et al. Morphology-Controlled Synthesis of Ni-MOFs with Highly Enhanced Electrocatalytic Performance for Urea Oxidation. Inorg Chem. 2019;58(17):11449-57.

[38] Vedharathinam V, Botte GG. Understanding the electro-catalytic oxidation mechanism of urea on nickel electrodes in alkaline medium. Electrochim Acta. 2012;81:292-300.

[39] Wang D, Yan W, Botte GG. Exfoliated nickel hydroxide nanosheets for urea electrolysis. Electrochemistry Communications. 2011;13(10):1135-8.

[40] Yan W, Wang D, Botte GG. Nickel and cobalt bimetallic hydroxide catalysts for urea electro-oxidation. Electrochim Acta. 2012;61:25-30.

[41] Yan W, Wang D, Diaz LA, Botte GG. Nickel nanowires as effective catalysts for urea electro-oxidation. Electrochim Acta. 2014;134:266-71.

[42] Ye K, Zhang D, Guo F, Cheng K, Wang G, Cao D. Highly porous nickel@ carbon sponge as a novel type of three-dimensional anode with low cost for high catalytic performance of urea electro-oxidation in alkaline medium. Journal of Power Sources. 2015;283:408-15.

[43] Shi W, Sun XJ, Ding R, Ying DF, Huang YF, Huang YX, et al. Trimetallic NiCoMo/graphene multifunctional electrocatalysts with moderate structural/electronic effects for highly efficient alkaline urea oxidation reaction. Chem Commun. 2020;56(48):6503-6.

[44] Li B, Song C, Rong J, Zhao J, Wang H-E, Yang P, et al. A new catalyst for urea oxidation: NiCo2S4 nanowires modified 3D carbon sponge. Journal of Energy Chemistry. 2020;50:195-205.

[45] Cook B. Introduction to fuel cells and hydrogen technology. Engineering Science & Education Journal. 2002;11(6):205-16.

[46] Mekhilef S, Saidur R, Safari A. Comparative study of different fuel cell technologies. Renewable and Sustainable Energy Reviews. 2012;16(1):981-9.

[47] Zhu B, Liang Z, Zou R. Designing Advanced Catalysts for Energy Conversion Based on Urea Oxidation Reaction. Small. 2020;16(7):1906133.

[48] Ganiyu SO, Martínez-Huitle CA, Rodrigo MA. Renewable energies driven electrochemical wastewater/soil decontamination technologies: A critical review of fundamental concepts and applications. Applied Catalysis B: Environmental. 2020;270:118857.

[49] Cao Y, Wang K, Wang X, Gu Z, Fan Q, Gibbons W, et al. Hierarchical porous activated carbon for supercapacitor derived from corn stalk core by potassium hydroxide activation. Electrochim Acta. 2016;212:839-47.

[50] Yang Y, Chiang K, Burke N. Porous carbon-supported catalysts for energy and environmental applications: A short review. Catalysis Today. 2011;178(1):197-205.

[51] Tsai W, Yang J, Lai C, Cheng Y, Lin C, Yeh C. Characterization and adsorption properties of eggshells and eggshell membrane. Bioresource technology. 2006;97(3):488-93.

[52] Li Z, Zhang L, Amirkhiz BS, Tan X, Xu Z, Wang H, et al. Carbonized chicken eggshell membranes with 3D architectures as high‐performance electrode materials for supercapacitors. Advanced Energy Materials. 2012;2(4):431-7.

[53] Nasrollahzadeh M, Sajadi SM, Hatamifard A. Waste chicken eggshell as a natural valuable resource and environmentally benign support for biosynthesis of catalytically active Cu/eggshell, Fe3O4/eggshell and Cu/Fe3O4/eggshell nanocomposites. Applied Catalysis B: Environmental. 2016;191:209-27.

[54] Lu S, Hummel M, Gu Z, Gu Y, Cen Z, Wei L, et al. Trash to treasure: A novel chemical route to synthesis of NiO/C for hydrogen production. International Journal of Hydrogen Energy. 2019;44(31):16144-53.

[55] Lu S, Gu Z, Hummel M, Zhou Y, Wang K, Xu BB, et al. Nickel Oxide Immobilized on the Carbonized Eggshell Membrane for Electrochemical Detection of Urea. Journal of The Electrochemical Society. 2020;167(10):106509.

[56] Maruthapandian V, Kumaraguru S, Mohan S, Saraswathy V, Muralidharan S. An Insight on the Electrocatalytic Mechanistic Study of Pristine Ni MOF (BTC) in Alkaline Medium for Enhanced OER and UOR. ChemElectroChem. 2018;5(19):2795-807.

[57] Ye K, Wang G, Cao D, Wang G. Recent advances in the electro-oxidation of urea for direct urea fuel cell and urea electrolysis. Topics Curr Chem. 2018;376(6):42.

[58] Perdew JP, Burke K, Ernzerhof M. Generalized gradient approximation made simple. Physical Review Letters. 1996;77(18):3865.

[59] Kresse G, Hafner J. Norm-conserving and ultrasoft pseudopotentials for first-row and transition elements. Journal of Physics: Condensed Matter. 1994;6(40):8245.

[60] Panchal M, Raghavendra G, Ojha S, Omprakash M, Acharya S. A single step process to synthesize ordered porous carbon from coconut shells-eggshells biowaste. Materials Research Express. 2019;6(11):115613.

[61] Liu H, Wang G, Liu J, Qiao S, Ahn H. Highly ordered mesoporous NiO anode material for lithium ion batteries with an excellent electrochemical performance. Journal of Materials Chemistry. 2011;21(9):3046-52.

[62] Zhai Z, Liu Q, Zhu Y, Cao J, Shi S. Synthesis of Ni(OH)2/graphene composite with enhanced electrochemical property by stirring solvothermal method. Journal of Alloys and Compounds. 2019;775:1316-23.

[63] Aghazadeh M, Golikand AN, Ghaemi M. Synthesis, characterization, and electrochemical properties of ultrafine β-Ni(OH)2 nanoparticles. Int J Hydrogen Energ. 2011;36(14):8674-9.

[64] Su Y-Z, Xiao K, Li N, Liu Z-Q, Qiao S-Z. Amorphous Ni (OH) 2@ three-dimensional Ni core–shell nanostructures for high capacitance pseudocapacitors and asymmetric supercapacitors. J Mater Chem A. 2014;2(34):13845-53.

[65] He Q, Wan Y, Jiang H, Pan Z, Wu C, Wang M, et al. Nickel Vacancies Boost Reconstruction in Nickel Hydroxide Electrocatalyst. ACS Energy Letters. 2018;3(6):1373-80.

[66] Ding Y, Li Y, Xue Y, Miao B, Li S, Jiang Y, et al. Atomically thick Ni(OH)2 nanomeshes for urea electrooxidation. Nanoscale. 2019;11(3):1058-64.

[67] Abdel Hameed RM, Medany SS. NiO nanoparticles on graphene nanosheets at different calcination temperatures as effective electrocatalysts for urea electro-oxidation in alkaline medium. J Colloid Interf Sci. 2017;508:291-302.

[68] Abdel Hameed RM, Medany SS. Enhanced electrocatalytic activity of NiO nanoparticles supported on graphite planes towards urea electro-oxidation in NaOH solution. International Journal of Hydrogen Energy. 2017;42(38):24117-30.

[69] Abutaleb A. Electrochemical oxidation of urea on NiCu alloy nanoparticles decorated carbon nanofibers. Catalysts. 2019;9(5):397.

[70] Yan X, Hu Q-T, Wang G, Zhang W-D, Liu J, Li T, et al. NiCo layered double hydroxide/hydroxide nanosheet heterostructures for highly efficient electro-oxidation of urea. Int J Hydrogen Energ. 2020;45(38):19206-13.

[71] Gu X, Yang D, Liu Z, Wang S, Feng L. Iron oxide promoted nickel/nickel oxide rough nanorods for efficient urea assisted water splitting. Electrochim Acta. 2020;353:136516.

[72] Tong Y, Chen P, Zhang M, Zhou T, Zhang L, Chu W, et al. Oxygen vacancies confined in nickel molybdenum oxide porous nanosheets for promoted electrocatalytic urea oxidation. Acs Catal. 2018;8(1):1-7.

[73] Daramola DA, Singh D, Botte GG. Dissociation rates of urea in the presence of NiOOH catalyst: a DFT analysis. The Journal of Physical Chemistry A. 2010;114(43):11513-21.

[74] Zhu X, Dou X, Dai J, An X, Guo Y, Zhang L, et al. Metallic nickel hydroxide nanosheets give superior electrocatalytic oxidation of urea for fuel cells. Angewandte Chemie International Edition. 2016;55(40):12465-9.

[75] Tahir M, Pan L, Idrees F, Zhang X, Wang L, Zou J-J, et al. Electrocatalytic oxygen evolution reaction for energy conversion and storage: a comprehensive review. Nano Energy. 2017;37:136-57.

[76] Li Y, Sun Y, Qin Y, Zhang W, Wang L, Luo M, et al. Recent advances on water‐splitting electrocatalysis mediated by noble‐metal‐based nanostructured materials. Advanced Energy Materials. 2020;10(11):1903120.

[77] Sigurdarson JJ, Svane S, Karring H. The molecular processes of urea hydrolysis in relation to ammonia emissions from agriculture. Reviews in Environmental Science and Bio/Technology. 2018;17(2):241-58.

[78] Ke K, Wang G, Cao D, Wang G. Recent Advances in the Electro-Oxidation of Urea for Direct Urea Fuel Cell and Urea Electrolysis. Electrocatalysis. 2020:41-78.

[79] Singh RK, Schechter A. Electrochemical investigation of urea oxidation reaction on β Ni (OH) 2 and Ni/Ni (OH) 2. Electrochimica Acta. 2018;278:405-11.

[80] Xiong P, Ao X, Chen J, Li J-G, Lv L, Li Z, et al. Nickel diselenide nanoflakes give superior urea electrocatalytic conversion. Electrochimica Acta. 2019;297:833-41.

[81] Bao C, Niu Q, Chen Z-A, Cao X, Wang H, Lu W. Ultrathin nickel-metal–organic framework nanobelt based electrochemical sensor for the determination of urea in human body fluids. RSC advances. 2019;9(50):29474-81.

[82] Hayler JD, Leahy DK, Simmons EM. A pharmaceutical industry perspective on sustainable metal catalysis. Organometallics. 2018;38(1):36-46.

[83] Kaushik M, Moores A. New trends in sustainable nanocatalysis: Emerging use of earth abundant metals. Current Opinion in Green and Sustainable Chemistry. 2017;7:39-45.

[84] Tammam RH, Saleh MM. On the electrocatalytic urea oxidation on nickel oxide nanoparticles modified glassy carbon electrode. J Electroanal Chem. 2017;794:189-96.

[85] Lu S, Hummel M, Gu Z, Wang Y, Wang K, Pathak R, et al. Highly Efficient Urea Oxidation via Nesting Nano-Nickel Oxide in Eggshell Membrane-Derived Carbon. Acs Sustain Chem Eng. 2021;9(4):1703-13.

[86] Xie J, Liu W, Lei F, Zhang X, Qu H, Gao L, et al. Iron‐Incorporated α‐Ni (OH) 2 Hierarchical Nanosheet Arrays for Electrocatalytic Urea Oxidation. Chemistry–A European Journal. 2018;24(69):18408-12.

[87] Zhang L, Wang L, Lin H, Liu Y, Ye J, Wen Y, et al. A Lattice‐Oxygen‐Involved Reaction Pathway to Boost Urea Oxidation. Angewandte Chemie International Edition. 2019;58(47):16820-5.

[88] Chen Y, Gao R, Ji S, Li H, Tang K, Jiang P, et al. Atomic‐Level Modulation of Electronic Density at Cobalt Single‐Atom Sites Derived from Metal–Organic Frameworks: Enhanced Oxygen Reduction Performance. Angewandte Chemie International Edition. 2021;60(6):3212-21.

[89] Ban J, Wen X, Xu H, Wang Z, Liu X, Cao G, et al. Dual Evolution in Defect and Morphology of Single‐Atom Dispersed Carbon Based Oxygen Electrocatalyst. Advanced Functional Materials. 2021:2010472.

[90] Lu Y, Su L, Qi J, Lei S, Liu B, Zang Q, et al. A combined DFT and experimental study on the nucleation mechanism of NiO nanodots on graphene. J Mater Chem A. 2018;6(28):13717-24.

[91] Liu YL, Liu R, Qin Y, Qiu QF, Chen Z, Cheng SB, et al. Flexible Electrochemical Urea Sensor Based on Surface Molecularly Imprinted Nanotubes for Detection of Human Sweat. Anal Chem. 2018;90(21):13081-7.

[92] Waisbren SE, Gropman AL, Members of the Urea Cycle Disorders C, Batshaw ML. Improving long term outcomes in urea cycle disorders-report from the Urea Cycle Disorders Consortium. J Inherit Metab Dis. 2016;39(4):573-84.

[93] Shen SG, Li BB, Li MN, Fan JM, Zhao ZJ. Removal of urea from wastewater by heterogeneous catalysis. Desalin Water Treat. 2015;55(1):70-6.

[94] Dutta D, Chandra S, Swain AK, Bahadur D. SnO2 quantum dots-reduced graphene oxide composite for enzyme-free ultrasensitive electrochemical detection of urea. Anal Chem. 2014;86(12):5914-21.

[95] Gupta VK, Goyal RN, Sharma RA. Comparative studies of neodymium (III)-selective PVC membrane sensors. Analytica Chimica Acta. 2009;647(1):66-71.

[96] Velichkova Y, Ivanov Y, Marinov I, Ramesh R, Kamini NR, Dimcheva N, et al. Amperometric electrode for determination of urea using electrodeposited rhodium and immobilized urease. Journal of Molecular Catalysis B: Enzymatic. 2011;69(3):168-75.

[97] Nie M, Du S, Li Q, Hummel M, Gu Z, Lu S. Tungsten carbide as supports for trimetallic AuPdPt electrocatalysts for methanol oxidation. Journal of The Electrochemical Society. 2020;167(4):044510.

[98] Nie M, Lu S, Li Q, Liu X, Du S. Facile solvothermal synthesis of HKUST-1 as electrocatalyst for hydrogen evolution reaction. SCIENTIA SINICA Chimica.46(4):357-64.

[99] Gupta VK, Karimi-Maleh H, Sadegh R. Simultaneous determination of hydroxylamine, phenol and sulfite in water and waste water samples using a voltammetric nanosensor. Int J Electrochem Sci. 2015;10:303-16.

[100] Gupta VK, Singh AK, Kumawat LK. Thiazole Schiff base turn-on fluorescent chemosensor for Al3+ ion. Sensors and Actuators B: Chemical. 2014;195:98-108.

[101] Gupta VK, Kumar S, Singh R, Singh L, Shoora S, Sethi B. Cadmium (II) ion sensing through p-tert-butyl calix [6] arene based potentiometric sensor. Journal of Molecular Liquids. 2014;195:65-8.

[102] Dehghani MH, Sanaei D, Ali I, Bhatnagar A. Removal of chromium (VI) from aqueous solution using treated waste newspaper as a low-cost adsorbent: kinetic modeling and isotherm studies. Journal of molecular liquids. 2016;215:671-9.

[103] Goyal RN, Gupta VK, Sangal A, Bachheti N. Voltammetric determination of uric acid at a fullerene‐C60‐modified glassy carbon electrode. Electroanalysis: An International Journal Devoted to Fundamental and Practical Aspects of Electroanalysis. 2005;17(24):2217-23.

[104] Goyal RN, Gupta VK, Chatterjee S. Fullerene-C60-modified edge plane pyrolytic graphite electrode for the determination of dexamethasone in pharmaceutical formulations and human biological fluids. Biosensors and Bioelectronics. 2009;24(6):1649-54.

[105] Goyal RN, Gupta VK, Chatterjee S. A sensitive voltammetric sensor for determination of synthetic corticosteroid triamcinolone, abused for doping. Biosensors and Bioelectronics. 2009;24(12):3562-8.

[106] Lin Z, Xue W, Chen H, Lin J-M. Peroxynitrous-acid-induced chemiluminescence of fluorescent carbon dots for nitrite sensing. Analytical Chemistry. 2011;83(21):8245-51.

[107] Gimbert LJ, Worsfold PJ. Environmental applications of liquid-waveguide-capillary cells coupled with spectroscopic detection. TrAC Trends in Analytical Chemistry. 2007;26(9):914-30.

[108] Breadmore MC, Shallan AI, Rabanes HR, Gstoettenmayr D, Abdul Keyon AS, Gaspar A, et al. Recent advances in enhancing the sensitivity of electrophoresis and electrochromatography in capillaries and microchips (2010–2012). Electrophoresis. 2013;34(1):29-54.

[109] Zhang J, Chen Z, Wu H, Wu F, He C, Wang B, et al. An electrochemical bifunctional sensor for the detection of nitrite and hydrogen peroxide based on layer-by-layer multilayer films of cationic phthalocyanine cobalt (ii) and carbon nanotubes. Journal of Materials Chemistry B. 2016;4(7):1310-7.

[110] Bedioui F, Griveau S. Electrochemical detection of nitric oxide: assessement of twenty years of strategies. Electroanalysis. 2013;25(3):587-600.

[111] Chokkareddy R, Redhi GG, Karthick T. A lignin polymer nanocomposite based electrochemical sensor for the sensitive detection of chlorogenic acid in coffee samples. Heliyon. 2019;5(3):e01457.

[112] Lu S, Hummel M, Kang S, Gu Z. Selective Voltammetric Determination of Nitrite Using Cobalt Phthalocyanine Modified on Multiwalled Carbon Nanotubes. Journal of The Electrochemical Society. 2020;167(4):046515.

[113] Lu S, Hummel M, Chen K, Zhou Y, Kang S, Gu Z. Synthesis of Au@ZIF-8 nanocomposites for enhanced electrochemical detection of dopamine. Electrochemistry Communications. 2020;114:106715.

[114] Nie M, Lu S, Lei D, Yang C, Zhao Z. Rapid synthesis of ZIF-8 nanocrystals for electrochemical detection of dopamine. Journal of The Electrochemical Society. 2017;164(13):H952.

[115] Ahmed TA, Kulshreshtha G, Hincke MT. Value-added Uses of Eggshell and Eggshell Membranes. Eggs as Functional Foods and Nutraceuticals for Human Health2019. p. 359-97.

[116] Chung SH, Manthiram A. Carbonized eggshell membrane as a natural polysulfide reservoir for highly reversible li‐S batteries. Advanced Materials. 2014;26(9):1360-5.

[117] Park S, Choi KS, Lee D, Kim D, Lim KT, Lee K-H, et al. Eggshell membrane: review and impact on engineering. Biosystems Engineering. 2016;151:446-63.

[118] Huang L, Li J, Wang Z, Li Y, He X, Yuan Y. Microwave absorption enhancement of porous C@$CoFe_2O_4$ nanocomposites derived from eggshell membrane. Carbon. 2019;143:507-16.

[119] Meng X, Deng D. Bio-inspired synthesis of 3-D network of NiO-Ni nanowires on carbonized eggshell membrane for lithium-ion batteries. Chemical Engineering Science. 2019;194:134-41.

[120] Zhao J, Syed JA, Wen X, Lu H, Meng X. Green synthesis of FeS anchored carbon fibers using eggshell membrane as a bio-template for energy storage application. Journal of Alloys and Compounds. 2019;777:974-81.

[121] Zhong S-L, Zhuang J, Yang D-P, Tang D. Eggshell membrane-templated synthesis of 3D hierarchical porous Au networks for electrochemical nonenzymatic glucose sensor. Biosensors and Bioelectronics. 2017;96:26-32.

[122] Lu L. Highly sensitive detection of nitrite at a novel electrochemical sensor based on mutually stabilized Pt nanoclusters doped CoO nanohybrid. Sensors and Actuators B: Chemical. 2019;281:182-90.

[123] Trasatti S, Petrii O. Real surface area measurements in electrochemistry. Journal of Electroanalytical Chemistry. 1992;327(1-2):353-76.

[124] Penner RM, Martin CR. Preparation and electrochemical characterization of ultramicroelectrode ensembles. Analytical Chemistry. 1987;59(21):2625-30.

[125] Yeo BS, Bell AT. In situ Raman study of nickel oxide and gold-supported nickel oxide catalysts for the electrochemical evolution of oxygen. The Journal of Physical Chemistry C. 2012;116(15):8394-400.

[126] Zhang LY, Ouyang Y, Wang S, Gong Y, Jiang M, Yuan W, et al. Ultrafast synthesis of uniform 4–5 atoms-thin layered tremella-like Pd nanostructure with extremely large electrochemically active surface area for formic acid oxidation. Journal of Power Sources. 2020;447:227248.

[127] Mai HD, Sung GY, Yoo H. Fabrication of nickel oxide nanostructures with high surface area and application for urease-based biosensor for urea detection. Rsc Adv. 2015;5(96):78807-14.

[128] Ahuja T, Kumar D, Singh N, Biradar AM, Rajesh. Potentiometric urea biosensor based on multi-walled carbon nanotubes (MWCNTs)/silica composite material. Materials Science and Engineering: C. 2011;31(2):90-4.

[129] Tyagi M, Tomar M, Gupta V. NiO nanoparticle-based urea biosensor. Biosensors and Bioelectronics. 2013;41:110-5.

[130] Huang C-P, Li Y-K, Chen T-M. A highly sensitive system for urea detection by using CdSe/ZnS core-shell quantum dots. Biosensors and Bioelectronics. 2007;22(8):1835-8.

[131] Zhao GQ, Rui K, Dou SX, Sun WP. Heterostructures for electrochemical hydrogen evolution reaction: a review. Adv Funct Mater. 2018;28(43):1803291.

[132] Cox R. Hydrogen: its technology and implication: production technology: CRC press, 2018.

[133] Staffell I, Dodds P, Scamman D, Abad AV, Dowell N, Ward K, et al. The role of hydrogen and fuel cells in future energy systems. H2FC SUPERGEN, London, UK. 2017.

[134] Zhang T, Wu MY, Yan DY, Mao J, Liu H, Hu WB, et al. Engineering oxygen vacancy on NiO nanorod arrays for alkaline hydrogen evolution. Nano Energy. 2018;43:103-9.

[135] Liu C, Wang Z, Song H, Qi Y, Li Y, Li F, et al. Experimental and numerical investigation on H_2/CO formation and their effects on combustion characteristics in a natural gas SI engine. Energy. 2018;143:597-605.

[136] Zou X, Zhang Y. Noble metal-free hydrogen evolution catalysts for water splitting. Chem Soc Rev. 2015;44(15):5148-80.

[137] Yin H, Zhao S, Zhao K, Muqsit A, Tang H, Chang L, et al. Ultrathin platinum nanowires grown on single-layered nickel hydroxide with high hydrogen evolution activity. Nat Commun. 2015;6:6430.

[138] Cheng N, Stambula S, Wang D, Banis MN, Liu J, Riese A, et al. Platinum single-atom and cluster catalysis of the hydrogen evolution reaction. Nat Commun. 2016;7:13638.

[139] Chen ZH, Ma ZP, Song JJ, Wang LX, Shao GJ. Novel one-step synthesis of wool-ball-like Ni-carbon nanotubes composite cathodes with favorable electrocatalytic activity for hydrogen evolution reaction in alkaline solution. J Power Sources. 2016;324:86-96.

[140] Zheng Y, Jiao Y, Vasileff A, Qiao SZ. The hydrogen evolution reaction in alkaline solution: from theory, single crystal models, to practical electrocatalysts. Angew Chem Int Ed. 2018;57(26):7568-79.

[141] Gong M, Zhou W, Tsai MC, Zhou J, Guan M, Lin MC, et al. Nanoscale nickel oxide/nickel heterostructures for active hydrogen evolution electrocatalysis. Nat Commun. 2014;5:4695.

[142] Liu T, Jiang CJ, Cheng B, You W, Yu JG. Hierarchical flower-like C/NiO composite hollow microspheres and its excellent supercapacitor performance. J Power Sources. 2017;359:371-8.

[143] Li T, Li XH, Wang ZX, Guo HJ, Li Y, Wang JX. A new design concept for preparing nickel-foam supported metal oxide microspheres with superior electrochemical properties. J Mater Chem A. 2017;5(26):13469-74.

[144] Czelej K, Cwieka K, Colmenares JC, Kurzydlowski KJ. Catalytic activity of NiO cathode in molten carbonate fuel cells. Appl Catal B-Environ. 2018;222:73-5.

[145] Li YH, Liu PF, Pan LF, Wang HF, Yang ZZ, Zheng LR, et al. Local atomic structure modulations activate metal oxide as electrocatalyst for hydrogen evolution in acidic water. Nat Commun. 2015;6:8064.

[146] Chinnappan A, Ji DX, Jayathilaka WADM, Baskar C, Qin XH, Ramakrishna S. Facile synthesis of electrospun C@NiO/Ni nanofibers as an electrocatalyst for hydrogen evolution reaction. Int J Hydrogen Energ. 2018;43(32):15217-24.

[147] Yang Y, Yang F, Hu HR, Lee SS, Wang Y, Zhao HR, et al. Dilute NiO/carbon nanofiber composites derived from metal organic framework fibers as electrode materials for supercapacitors. Chem Eng J. 2017;307:583-92.

[148] Xu YF, Gao MR, Zheng YR, Jiang J, Yu SH. Nickel/nickel(II) oxide nanoparticles anchored onto cobalt(IV) diselenide nanobelts for the electrochemical production of hydrogen. Angew Chem Int Ed. 2013;52(33):8546-50.

[149] Tembe S, Kubal BS, Karve M, D'Souza SF. Glutaraldehyde activated eggshell membrane for immobilization of tyrosinase from amorphophallus companulatus: application in construction of electrochemical biosensor for dopamine. Anal Chim Acta. 2008;612(2):212-7.

[150] Deng WT, Liu Y, Zhang Y, Lu F, Chen QY, Ji XB. Enhanced electrochemical capacitance of nanoporous NiO based on an eggshell membrane. Rsc Adv. 2012;2(5):1743-5.

[151] Nguyen VH, Lee DH, Baek SY, Kim YH. Recycling different eggshell membranes for lithium-ion battery. Mater Lett. 2018;228:504-8.

[152] Meng X, Deng D. Trash to treasure: waste eggshells used as reactor and template for synthesis of Co_9S_8 nanorod arrays on carbon fibers for energy storage. Chem Mater. 2016;28(11):3897-904.

[153] Ma LB, Chen RP, Hu Y, Zhang WJ, Zhu GY, Zhao PY, et al. Nanoporous and lyophilic battery separator from regenerated eggshell membrane with effective suppression of dendritic lithium growth. Energy Storage Mater. 2018;14:258-66.

[154] Park S, Choi KS, Lee D, Kim D, Lim KT, Lee KH, et al. Eggshell membrane: review and impact on engineering. Biosyst Eng. 2016;151:446-63.

[155] Meng XH, Deng D. Bio-inspired synthesis of 3-D network of NiO-Ni nanowires on carbonized eggshell membrane for lithium-ion batteries. Chem Eng Sci. 2019;194:134-41.

[156] Selvakumari JC, Nishanthi ST, Dhanalakshmi J, Ahila M, Padiyan DP. Bio-active synthesis of tin oxide nanoparticles using eggshell membrane for energy storage application. Appl Surf Sci. 2018;441:530-7.

[157] Chung SH, Manthiram A. Carbonized eggshell membrane as a natural polysulfide reservoir for highly reversible Li‐S batteries. Adv Mater. 2014;26(9):1360-5.

[158] Yu H, Tang Q, Wu J, Lin Y, Fan L, Huang M, et al. Using eggshell membrane as a separator in supercapacitor. J Power Sources. 2012;206:463-8.

[159] Zhang ZC, Xu B, Wang X. Engineering nanointerfaces for nanocatalysis. Chem Soc Rev. 2014;43(22):7870-86.

[160] Lu S, Yang C, Nie M. Hydrothermal synthesized urchin-like nickel-cobalt carbonate hollow spheres for sensitive amperometric detection of nitrite. J Alloy Compd. 2017;708:780-6.

[161] Hou HS, Jing MJ, Yang YC, Zhang Y, Song WX, Yang XM, et al. Antimony nanoparticles anchored on interconnected carbon nanofibers networks as advanced anode material for sodium-ion batteries. J Power Sources. 2015;284:227-35.

[162] Li Y, Xie X, Liu J, Cai M, Rogers J, Shen W. Synthesis of α-$Ni(OH)_2$ with hydrotalcite-like structure: precursor for the formation of NiO and Ni nanomaterials with fibrous shapes. Chem Eng J. 2008;136(2-3):398-408.

[163] Tian JY, Shao Q, Dong XJ, Zheng JL, Pan D, Zhang XY, et al. Bio-template synthesized NiO/C hollow microspheres with enhanced Li-ion battery electrochemical performance. Electrochim Acta. 2018;261:236-45.

[164] Hall DS, Bock C, MacDougall BR. The electrochemistry of metallic nickel: oxides, hydroxides, hydrides and alkaline hydrogen evolution. J Electrochem Soc. 2013;160(3):F235-F43.

[165] Zhang LL, Zhu SQ, Dong SY, Woo NJ, Xu ZL, Huang JQ, et al. Co nanoparticles encapsulated in porous N-doped carbon nanofibers as an efficient electrocatalyst for hydrogen evolution reaction. J Electrochem Soc. 2018;165(15):J3271-J5.

[166] Wang DY, Gong M, Chou HL, Pan CJ, Chen HA, Wu Y, et al. Highly active and stable hybrid catalyst of cobalt-doped FeS^2 nanosheets-carbon nanotubes for hydrogen evolution reaction. J Am Chem Soc. 2015;137(4):1587-92.

[167] Ji DX, Peng SJ, Lu J, Li LL, Yang SY, Yang GR, et al. Design and synthesis of porous channel-rich carbon nanofibers for self-standing oxygen reduction reaction and hydrogen evolution reaction bifunctional catalysts in alkaline medium. J Mater Chem A. 2017;5(16):7507-15.

[168] Liu YY, Zhang HP, Zhu B, Zhang HW, Fan LD, Chai XY, et al. C/N-co-doped Pd coated Ag nanowires as a high-performance electrocatalyst for hydrogen evolution reaction. Electrochim Acta. 2018;283:221-7.

[169] Wang DZ, Zhang XY, Du ZJ, Mo ZY, Wu YF, Yang Q, et al. $CoNi_2S_4$ nanoparticles as highly efficient electrocatalysts for the hydrogen evolution reaction in alkaline media. Int J Hydrogen Energ. 2017;42(5):3043-50.

[170] An L, Huang L, Zhou PP, Yin J, Liu HY, Xi PX. A self-standing high-performance hydrogen evolution electrode with nanostructured $NiCo_2O_4$/CuS heterostructures. Adv Funct Mater. 2015;25(43):6814-22.

[171] Chu M, Wang L, Li X, Hou MJ, Li N, Dong YZ, et al. Carbon coated nickel-nickel oxide composites as a highly efficient catalyst for hydrogen evolution reaction in acid medium. Electrochim Acta. 2018;264:284-91.

[172] Jin J, Zhu Y, Liu Y, Li Y, Peng W, Zhang G, et al. CoP nanoparticles combined with WS_2 nanosheets as efficient electrocatalytic hydrogen evolution reaction catalyst. Int J Hydrogen Energ. 2017;42(7):3947-54.

[173] Tukimin N, Abdullah J, Sulaiman Y. Review-Electrochemical detection of uric acid, dopamine and ascorbic acid. Journal of the Electrochemical Society. 2018;165(7):B258-B67.

[174] Lammel S, Steinberg EE, Foldy C, Wall NR, Beier K, Luo L, et al. Diversity of transgenic mouse models for selective targeting of midbrain dopamine neurons. Neuron. 2015;85(2):429-38.

[175] Robinson DL, Venton BJ, Heien ML, Wightman RM. Detecting subsecond dopamine release with fast-scan cyclic voltammetry in vivo. Clinical chemistry. 2003;49(10):1763-73.

[176] Seeman P. Parkinson's disease treatment may cause impulse-control disorder via dopamine D3 receptors. Synapse. 2015;69(4):183-9.

[177] Patrice FT, Zhao LJ, Fodjo EK, Li DW, Qiu KP, Long YT. Highly sensitive and selective electrochemical detection of dopamine using hybrid bilayer membranes. Chemelectrochem. 2019;6(3):634-7.

[178] Bacil RP, Chen L, Serrano SHP, Compton RG. Dopamine oxidation at gold electrodes: mechanism and kinetics near neutral pH. Physical Chemistry Chemical Physics. 2020;22(2):607-14.

[179] Yu J, Ge L, Huang J, Wang S, Ge S. Microfluidic paper-based chemiluminescence biosensor for simultaneous determination of glucose and uric acid. Lab Chip. 2011;11(7):1286-91.

[180] Wang HY, Hui QS, Xu LX, Jiang JG, Sun Y. Fluorimetric determination of dopamine in pharmaceutical products and urine using ethylene diamine as the fluorigenic reagent. Analytica Chimica Acta. 2003;497(1-2):93-9.

[181] Satyanarayana M, Reddy KK, Gobi KV. Nanobiocomposite based electrochemical sensor for sensitive determination of serotonin in presence of dopamine, ascorbic acid and uric acid in vitro. Electroanalysis. 2014;26(11):2365-72.

[182] Yue HY, Wu PF, Huang S, Wang ZZ, Gao X, Song SS, et al. Golf ball-like MoS_2 nanosheet arrays anchored onto carbon nanofibers for electrochemical detection of dopamine. Microchimica Acta. 2019;186(6):378.

[183] Sajid M, Baig N, Alhooshani K. Chemically modified electrodes for electrochemical detection of dopamine: Challenges and opportunities. Trac-Trend Anal Chem. 2019;118:368-85.

[184] Compton RG, Banks CE. Understanding voltammetry. London, U.K: World Scientific, 2011.

[185] Hočevar SB, Wang J, Deo RP, Musameh M, Ogorevc B. Carbon nanotube modified microelectrode for enhanced voltammetric detection of dopamine in the presence of ascorbate. Electroanalysis. 2005;17(5‐6):417-22.

[186] Chen L, Peng Y, Wang H, Gu Z, Duan C. Synthesis of Au@ZIF-8 single- or multi-core-shell structures for photocatalysis. Chemical Communications. 2014;50(63):8651-4.

[187] Pan Y, Liu Y, Zeng G, Zhao L, Lai Z. Rapid synthesis of zeolitic imidazolate framework-8 (ZIF-8) nanocrystals in an aqueous system. Chemical Communications. 2011;47(7):2071-3.

[188] Song QL, Nataraj SK, Roussenova MV, Tan JC, Hughes DJ, Li W, et al. Zeolitic imidazolate framework (ZIF-8) based polymer nanocomposite membranes for gas separation. Energy & Environmental Science. 2012;5(8):8359-69.

[189] Assfour B, Leoni S, Seifert G. Hydrogen adsorption sites in zeolite imidazolate frameworks ZIF-8 and ZIF-11. Journal of Physical Chemistry C. 2010;114(31):13381-4.

[190] Nie M, Lu S, Li Q, Liu X, Du S. Facile solvothermal synthesis of HKUST-1 as electrocatalyst for hydrogen evolution reaction. SCIENTIA SINICA Chimica. 2016;46(4):357-64.

[191] Duan C, Zheng J. Bimetallic MOF-based enzyme-free sensor for highly sensitive and delective detection of dopamine. Journal of The Electrochemical Society. 2019;166(12):B942-B7.

[192] Saraf M, Rajak R, Mobin SM. A fascinating multitasking Cu-MOF/rGO hybrid for high performance supercapacitors and highly sensitive and selective electrochemical nitrite sensors. Journal of Materials Chemistry A. 2016;4(42):16432-45.

[193] Zhang CY, Wang MY, Liu L, Yang XJ, Xu XY. Electrochemical investigation of a new Cu-MOF and its electrocatalytic activity towards H_2O_2 oxidation in alkaline solution. Electrochemistry Communications. 2013;33:131-4.

[194] Nie M, Lu S, Lei D, Yang C, Zhao ZZ. Rapid Synthesis of ZIF-8 Nanocrystals for Electrochemical Detection of Dopamine. J Electrochem Soc. 2017;164(13):H952-H7.

[195] Yu AM, Liang ZJ, Cho J, Caruso F. Nanostructured electrochemical sensor based on dense gold nanoparticle films. Nano Letters. 2003;3(9):1203-7.

[196] Wang H, Zhang S, Li S, Qu J. Electrochemical sensor based on palladium-reduced graphene oxide modified with gold nanoparticles for simultaneous determination of acetaminophen and 4-aminophenol. Talanta. 2018;178:188-94.

[197] Devi NR, Sasidharan M, Sundramoorthy AK. Gold nanoparticles-thiol-functionalized reduced graphene oxide coated electrochemical sensor system for selective detection of mercury Ion. Journal of the Electrochemical Society. 2018;165(8):B3046-B53.

[198] Yadav DK, Ganesan V, Sonkar PK, Gupta R, Rastogi PK. Electrochemical investigation of gold nanoparticles incorporated zinc based metal-organic framework for selective recognition of nitrite and nitrobenzene. Electrochimica Acta. 2016;200:276-82.

[199] Jin JC, Wu J, Yang GP, Wu YL, Wang YY. A microporous anionic metal-organic framework for a highly selective and sensitive electrochemical sensor of Cu^{2+} ions. Chemical Communications. 2016;52(54):8475-8.

[200] Sun C-L, Lee H-H, Yang J-M, Wu C-C. The simultaneous electrochemical detection of ascorbic acid, dopamine, and uric acid using graphene/size-selected Pt nanocomposites. Biosensors and Bioelectronics. 2011;26(8):3450-5.

[201] Wang L, Meng T, Fan Y, Chen C, Guo Z, Wang H, et al. Electrochemical study of acetaminophen oxidation by gold nanoparticles supported on a leaf-like zeolitic imidazolate framework. J Colloid Interface Sci. 2018;524:1-7.

[202] Cheng L, Fan YJ, Shen XC, Liang H. Highly sensitive detection of dopamine at ionic liquid functionalized RGO/ZIF-8 nanocomposite-modified electrode. Journal of Nanomaterials. 2019:8936095.

[203] Li D, Lin C, Batchelor-McAuley C, Chen L, Compton RG. Tafel analysis in practice. Journal of Electroanalytical Chemistry. 2018;826:117-24.

[204] Zhu G, He Z, Chen J, Zhao J, Feng X, Ma Y, et al. Highly conductive three-dimensional MnO_2-carbon nanotube-graphene-Ni hybrid foam as a binder-free supercapacitor electrode. Nanoscale. 2014;6(2):1079-85.

[205] Yue HY, Wu PF, Huang S, Wang ZZ, Gao X, Song SS, et al. Golf ball-like MoS_2 nanosheet arrays anchored onto carbon nanofibers for electrochemical detection of dopamine. Mikrochim Acta. 2019;186(6):378.

[206] Khan MZH, Liu X, Tang Y, Zhu J, Hu W, Liu X. A glassy carbon electrode modified with a composite consisting of gold nanoparticle, reduced graphene oxide and poly(L-arginine) for simultaneous voltammetric determination of dopamine, serotonin and L-tryptophan. Mikrochim Acta. 2018;185(9):439.

[207] Cheng L, Fan YJ, Shen XC, Liang H. Highly Sensitive Detection of Dopamine at Ionic Liquid Functionalized RGO/ZIF-8 Nanocomposite-Modified Electrode. J Nanomater. 2019;2019.

[208] Sáenz HSC, Hernández-Saravia LP, Selva JS, Sukeri A, Espinoza-Montero PJ, Bertotti M. Electrochemical dopamine sensor using a nanoporous gold microelectrode: a proof-of-concept study for the detection of dopamine release by scanning electrochemical microscopy. Microchimica Acta. 2018;185(8):367.

[209] Duan C, Zheng J. Bimetallic MOF-Based Enzyme-Free Sensor for Highly Sensitive and Selective Detection of Dopamine. Journal of The Electrochemical Society. 2019;166(12):B942-B7.

[210] Tavakolian E, Tashkhourian J. Sonication-assisted preparation of a nanocomposite consisting of reduced graphene oxide and CdSe quantum dots, and its

application to simultaneous voltammetric determination of ascorbic acid, dopamine and uric acid. Microchimica Acta. 2018;185(10):456.

[211] Hou C-Y, Fu L-M, Ju W-J, Wu P-Y. Microfluidic colorimetric system for nitrite detection in foods. Chemical Engineering Journal. 2020:125573.

[212] Annalakshmi M, Kumaravel S, Chen S-M, Balasubramanian P, Balamurugan T. A straightforward ultrasonic-assisted synthesis of zinc sulfide for supersensitive detection of carcinogenic nitrite ions in water samples. Sensors and Actuators B: Chemical. 2020;305:127387.

[213] Sall ML, Fall B, Diédhiou I, Lo M, Diaw AKD, Gningue-Sall D, et al. Toxicity and electrochemical detection of lead, cadmium and nitrite ions by organic conducting polymers: a review. Chemistry Africa. 2020:1-14.

[214] Zhu D, Zhen Q, Xin J, Ma H, Tan L, Pang H, et al. A free-standing and flexible phosphorus/nitrogen dual-doped three-dimensional reticular porous carbon frameworks encapsulated cobalt phosphide with superior performance for nitrite detection in drinking water and sausage samples. Sensors and Actuators B: Chemical. 2020;321:128541.

[215] Lin S-L, Hsu J-W, Fuh M-R. Simultaneous determination of nitrate and nitrite in vegetables by poly (vinylimidazole-co-ethylene dimethacrylate) monolithic capillary liquid chromatography with UV detection. Talanta. 2019;205:120082.

[216] Sun XJ, Zhang L, Zhang XH, Liu XX, Jian J, Kong DC, et al. Electrochemical dopamine sensor based on superionic conducting potassium ferrite. Biosens Bioelectron. 2020;153:112045.

[217] Murray E, Roche P, Harrington K, McCaul M, Moore B, Morrin A, et al. Low cost 235 nm ultra-violet light-emitting diode-based absorbance detector for application in a portable ion chromatography system for nitrite and nitrate monitoring. Journal of Chromatography A. 2019;1603:8-14.

[218] Li D, Wang T, Li Z, Xu X, Wang C, Duan Y. Application of graphene-based materials for detection of nitrate and nitrite in water-a review. Sensors. 2020;20(1):54.

[219] Lu S, Hummel M, Wang X, He W, Pathak R, Dong X, et al. Communication—In Situ Electrodeposition of Nickel Phosphide on Ni Foam for Non-Enzymatic Detection of Nitrite. Journal of The Electrochemical Society. 2020;167(14):146517.

[220] Chen J, Pang S, He L, Nugen SR. Highly sensitive and selective detection of nitrite ions using Fe3O4@SiO2/Au magnetic nanoparticles by surface-enhanced Raman spectroscopy. Biosensors and Bioelectronics. 2016;85:726-33.

[221] Han Y, Zhang R, Dong C, Cheng F, Guo Y. Sensitive electrochemical sensor for nitrite ions based on rose-like AuNPs/MoS2/graphene composite. Biosensors and Bioelectronics. 2019;142:111529.

[222] Lu S, Yang C, Nie M. Hydrothermal synthesized urchin-like nickel-cobalt carbonate hollow spheres for sensitive amperometric detection of nitrite. Journal of Alloys and Compounds. 2017;708:780-6.

[223] Sahoo MK, Samantara AK, Behera JN. In Situ Transformed Cobalt Metal–Organic Framework Electrocatalysts for the Electrochemical Oxygen Evolution Reaction. Inorganic Chemistry. 2020;59(17):12252-62.

[224] Liu C-S, Li J, Pang H. Metal-organic framework-based materials as an emerging platform for advanced electrochemical sensing. Coordination Chemistry Reviews. 2020;410:213222.

[225] Ding J, Zhong L, Wang X, Chai L, Wang Y, Jiang M, et al. General approach to MOF-derived core-shell bimetallic oxide nanowires for fast response to glucose oxidation. Sensors and Actuators B: Chemical. 2020;306:127551.

[226] Ma X, Pang C, Li S, Xiong Y, Li J, Luo J, et al. Synthesis of Zr-coordinated amide porphyrin-based two-dimensional covalent organic framework at liquid-liquid interface for electrochemical sensing of tetracycline. Biosensors and Bioelectronics. 2019;146:111734.

[227] Zhou N, Su F, Guo C, He L, Jia Z, Wang M, et al. Two-dimensional oriented growth of Zn-MOF-on-Zr-MOF architecture: A highly sensitive and selective platform for detecting cancer markers. Biosensors and Bioelectronics. 2019;123:51-8.

[228] Cai F, Wang Q, Chen X, Qiu W, Zhan F, Gao F, et al. Selective binding of Pb2+ with manganese-terephthalic acid MOF/SWCNTs: Theoretical modeling, experimental study and electroanalytical application. Biosensors and Bioelectronics. 2017;98:310-6.

[229] Chai L, Hu Z, Wang X, Xu Y, Zhang L, Li TT, et al. Stringing Bimetallic Metal–Organic Framework‐Derived Cobalt Phosphide Composite for High‐Efficiency Overall Water Splitting. Advanced Science. 2020;7(5):1903195.

[230] Niu X, Shi Q, Zhu W, Liu D, Tian H, Fu S, et al. Unprecedented peroxidase-mimicking activity of single-atom nanozyme with atomically dispersed Fe–Nx moieties hosted by MOF derived porous carbon. Biosensors and Bioelectronics. 2019;142:111495.

[231] Wang X, Dong A, Hu Y, Qian J, Huang S. A review of recent work on using metal–organic frameworks to grow carbon nanotubes. Chemical Communications. 2020;56(74):10809-23.

[232] Fu K, Zhang R, He J, Bai H, Zhang G. Sensitive detection of ketamine with an electrochemical sensor based on UV-induced polymerized molecularly imprinted membranes at graphene and MOFs modified electrode. Biosensors and Bioelectronics. 2019;143:111636.

[233] Guo J, Lin C-Y, Xia Z, Xiang Z. A Pyrolysis-Free Covalent Organic Polymer for Oxygen Reduction. Angewandte Chemie International Edition. 2018;57(38):12567-72.

[234] Park J, Lee M, Feng D, Huang Z, Hinckley AC, Yakovenko A, et al. Stabilization of hexaaminobenzene in a 2D conductive metal–organic framework for high power sodium storage. Journal of the American Chemical Society. 2018;140(32):10315-23.

[235] Meng Z, Stolz RM, Mirica KA. Two-dimensional chemiresistive covalent organic framework with high intrinsic conductivity. Journal of the American Chemical Society. 2019;141(30):11929-37.

[236] Ko M, Mendecki L, Eagleton AM, Durbin CG, Stolz RM, Meng Z, et al. Employing Conductive Metal–Organic Frameworks for Voltammetric Detection of Neurochemicals. Journal of the American Chemical Society. 2020;142(27):11717-33.

[237] Qiu Z, Yang T, Gao R, Jie G, Hou W. An electrochemical ratiometric sensor based on 2D MOF nanosheet/Au/polyxanthurenic acid composite for detection of dopamine. Journal of Electroanalytical Chemistry. 2019;835:123-9.

[238] Meng Z, Stolz RM, Mendecki L, Mirica KA. Electrically-transduced chemical sensors based on two-dimensional nanomaterials. Chemical reviews. 2019;119(1):478-598.

[239] Zhao Z, Zhang J, Wang W, Sun Y, Li P, Hu J, et al. Synthesis and electrochemical properties of Co3O4-rGO/CNTs composites towards highly sensitive nitrite detection. Applied Surface Science. 2019;485:274-82.

[240] Mounesh, Venugopala Reddy KR. Sensitive and reliable electrochemical detection of nitrite and H2O2 embellish-CoPc coupled with appliance of composite MWCNTs. Analytica Chimica Acta. 2020;1108:98-107.

[241] Zhe T, Li R, Wang Q, Shi D, Li F, Liu Y, et al. In situ preparation of FeSe nanorods-functionalized carbon cloth for efficient and stable electrochemical detection of nitrite. Sensors and Actuators B: Chemical. 2020;321:128452.

[242] Wang X, Li M, Yang S, Shan J. A novel electrochemical sensor based on TiO2–Ti3C2TX/CTAB/chitosan composite for the detection of nitrite. Electrochimica Acta. 2020;359:136938.

[243] Lei P, Zhou Y, Zhu R, Wu S, Jiang C, Dong C, et al. Gold nanoparticles decorated bimetallic CuNi-based hollow nanoarchitecture for the enhancement of electrochemical sensing performance of nitrite. Microchimica Acta. 2020;187(10):572.

[244] Zhao X, Li N, Jing M, Zhang Y, Wang W, Liu L, et al. Monodispersed and spherical silver nanoparticles/graphene nanocomposites from gamma-ray assisted in-situ synthesis for nitrite electrochemical sensing. Electrochimica Acta. 2019;295:434-43.

[245] Annalakshmi M, Balaji R, Chen S-M, Chen T-W, Huang YC. A sensitive and high-performance electrochemical detection of nitrite in water samples based on Sonochemical synthesized Strontium Ferrite Nanochain architectures. Electrochimica Acta. 2020;360:136797.

[246] Balasubramanian P, Settu R, Chen S-M, Chen T-W, Sharmila G. A new electrochemical sensor for highly sensitive and selective detection of nitrite in food samples based on sonochemical synthesized Calcium Ferrite (CaFe2O4) clusters modified screen printed carbon electrode. Journal of colloid and interface science. 2018;524:417-26.

[247] Aralekallu S, Mohammed I, Manjunatha N, Palanna M, Dhanjai, Sannegowda LK. Synthesis of novel azo group substituted polymeric phthalocyanine for amperometric sensing of nitrite. Sensors and Actuators B: Chemical. 2019;282:417-25.

[248] Jilani BS, Mounesh, Malathesh P, Mruthyunjayachari CD, Reddy KRV. Cobalt (II) tetra methyl-quinoline oxy bridged phthalocyanine carbon nano particles modified glassy carbon electrode for sensing nitrite: A voltammetric study. Materials Chemistry and Physics. 2020;239:121920.

[249] Wang N, Lin M, Dai H, Ma H. Functionalized gold nanoparticles/reduced graphene oxide nanocomposites for ultrasensitive electrochemical sensing of mercury ions based on thymine–mercury–thymine structure. Biosensors and Bioelectronics. 2016;79:320-6.

[250] Palanisamy S, Thirumalraj B, Chen S-M. A novel amperometric nitrite sensor based on screen printed carbon electrode modified with graphite/β-cyclodextrin composite. Journal of Electroanalytical Chemistry. 2016;760:97-104.